

A COMPTON CAMERA FOR IN-VIVO DOSIMETRY IN ION-BEAM RADIOTHERAPY

DISSERTATION

zur Erlangung des akademischen Grades

Doctor rerum naturalium
(Dr. rer. nat.)

vorgelegt

der Fakultät Mathematik und Naturwissenschaften
der Technischen Universität Dresden

von

Dipl.-Phys. Thomas Kormoll

geboren am 7.12.1983 in Flensburg

Eingereicht am 3.12.2012

Verteidigt am 22.2.2013

Die Dissertation wurde in der Zeit von April 2009 bis November 2012 am
Nationalen Zentrum für Strahlenforschung in der Onkologie, OncoRay,
Dresden, angefertigt.

1. Gutachter: Prof. Dr. Kai Zuber
2. Gutachter: Prof. Dr. Wolfgang Enhardt

Abstract/Zusammenfassung

This work presents the first efforts at the Dresden University of Technology to study the feasibility of Compton imaging as a modality to monitor ion beam radiation therapy. The inherent limitations of the method have been studied by means of calculation and Monte Carlo simulation. As a result, the room-temperature semiconductor cadmium zinc telluride appeared as a promising detector material for a clinical device. For more detailed investigation, a simple Compton camera has been constructed comprising a cadmium zinc telluride detector and a position sensitive scintillation detector. This system has proven that accurate imaging of radioactive point sources in the laboratory is feasible. More practical restrictions of Compton imaging in beam conditions have been derived through experiments at a proton facility. Through the experimental work with the Compton camera developed in this work, valuable information was gathered which allowed to test the image reconstruction and to direct the further research towards a clinical Compton camera system.

In dieser Arbeit wird die Bildgebung durch eine Compton-Kamera zur Überwachung der Partikelstrahlentherapie erstmals an der Technischen Universität Dresden untersucht. Die inhärenten Beschränkungen der Methode wurden durch Berechnungen und Monte Carlo Simulationen studiert. Im Zuge dieser Untersuchungen erschien der Raumtemperatur-Halbleiter Cadmium Zink Tellurid als ein vielversprechendes Detektor-Material. Zur weiteren Untersuchung wurde eine einfache Compton-Kamera konstruiert bestehend aus einem Cadmium Zink Tellurid Detektor und einem ortsempfindlichen Szintillationsdetektor. Das System hat gezeigt, dass eine akkurate Bildgebung mit radioaktiven Punktquellen unter Laborbedingungen möglich ist. Weitere praktische Beschränkungen der Compton-Bildgebung unter Strahlbedingungen konnten durch Experimente an einem Protonen-Strahl hergeleitet werden. Durch die experimentellen Erfahrungen mit der in dieser Arbeit entwickelten Compton-Kamera konnten wertvolle Informationen gesammelt werden, die erlauben, die Bildrekonstruktion zu evaluieren und dazu beitragen, die weitere Forschung hin zu einer klinisch anwendbaren Compton-Kamera zu leiten.

Table of Contents

| | |
|--|-------------|
| Abstract/Zusammenfassung..... | i |
| Illustration Index..... | iv |
| Index of Tables..... | vii |
| List of Abbreviations..... | viii |
| 0 Introduction..... | 1 |
| 0.1 Motivation..... | 4 |
| 0.2 Task..... | 5 |
| 1 Physical Background..... | 6 |
| 1.1 Interaction of Ionizing Radiation with Matter..... | 6 |
| 1.1.1 Coherent Photon Scattering..... | 6 |
| 1.1.2 Incoherent Photon Scattering..... | 7 |
| 1.1.3 Complete Absorption in the Nuclear Electric Field..... | 8 |
| 1.1.4 Pair Production..... | 9 |
| 1.1.5 Total Photon Cross Section..... | 10 |
| 1.1.6 Directly Ionizing Radiation..... | 10 |
| 1.2 Prompt γ -rays from Nuclear Reactions..... | 11 |
| 1.3 Detector Technology..... | 13 |
| 1.3.1 Semiconductor Detectors..... | 15 |
| 1.3.2 Scintillation Detectors..... | 22 |
| 1.4 Compton Imaging..... | 25 |
| 1.4.1 Image Formation..... | 27 |
| 1.4.2 History and Application of Compton Cameras..... | 28 |
| 1.5 Prompt γ -ray Imaging for In-vivo Dosimetry – Work of Other Groups..... | 29 |

| | |
|---|------------|
| 2 Design Study | 31 |
| 2.1 Introduction..... | 31 |
| 2.1.1 Emission Spectra – Available Data..... | 32 |
| 2.2 Materials and Methods..... | 32 |
| 2.2.1 Angular Resolution..... | 32 |
| 2.2.2 Efficiency..... | 44 |
| 2.3 Results..... | 48 |
| 2.4 Conclusions..... | 52 |
| 3 Prototype System | 54 |
| 3.1 Overview..... | 54 |
| 3.2 System Components..... | 56 |
| 3.2.1 CdZnTe Detector and its Front-End-Electronics..... | 56 |
| 3.2.2 LSO Block-Detector..... | 60 |
| 3.2.3 Mounting Frame..... | 61 |
| 3.2.4 DAQ Hardware and Software..... | 62 |
| 3.3 Results..... | 69 |
| 3.3.1 Detector Performance..... | 69 |
| 3.3.2 System Performance..... | 75 |
| 3.4 Conclusions..... | 80 |
| 4 Beam Experiments | 82 |
| 4.1 Introduction..... | 82 |
| 4.2 Materials and Methods..... | 83 |
| 4.3 Results..... | 84 |
| 4.3.1 Source Test..... | 84 |
| 4.3.2 Beam Profile..... | 85 |
| 4.3.3 Trigger Rate..... | 85 |
| 4.3.4 Pixel selection in the LSO..... | 86 |
| 4.3.5 Phantom Measurement..... | 87 |
| 4.4 Conclusions..... | 89 |
| 5 Discussion | 90 |
| Appendix A | 95 |
| A.1 Technical Drawing of the CdZnTe Electrode Layout..... | 95 |
| Bibliography | 99 |
| Danksagung | 107 |
| Erklärung | 109 |

Illustration Index

| | |
|---|----|
| Figure 0.1: Dose deposition in polymethyl metacrylate (PMMA) of photons compared to protons..... | 1 |
| Figure 0.2: Double head in-beam PET camera system BASTEI at GSI, Darmstadt..... | 3 |
| Figure 1.1: The two Feynman graphs of Compton scattering (first order, s- and u-channel)..... | 7 |
| Figure 1.2: Three Feynman graphs of the incoherent scattering of a photon off an electron bound to a nucleus..... | 8 |
| Figure 1.3: Two possible crossing channels of the pair production in the nuclear electric field..... | 9 |
| Figure 1.4: Mass attenuation coefficient μ/ρ of CdZnTe [XCOM]..... | 10 |
| Figure 1.5: Photon emission spectrum from a water phantom irradiated with 200 MeV protons, simulated with Geant4 [Fie10a]..... | 12 |
| Figure 1.6: Circuit diagram of the simplest case of a preamplifier..... | 14 |
| Figure 1.7: The induced charge on the anode in the absence of charge loss as a function of time for interactions that take place near the cathode, near the anode and halfway in between..... | 18 |
| Figure 1.8: Weighting potential in a coplanar grid detector along a line perpendicular to the electrodes and ending on one of the collecting strips..... | 20 |
| Figure 1.9: Schematic display of the weighting potential of the collecting anode in steering grid configuration..... | 21 |
| Figure 1.10: Principle of Compton imaging..... | 26 |
| Figure 1.11: Event chain in multiple Compton scattering..... | 26 |
| Figure 2.1: The influence of primary γ -ray energy E_0 and the scatter angle φ on the Compton camera angular resolution measure due to the first scatter detector denoted by the term T_1 | 34 |
| Figure 2.2: The variation of T_2 in scatter-scatter mode with φ_2 where E_0 is 1 MeV and φ is 20 degree..... | 35 |
| Figure 2.3: The influence of primary γ -ray energy E_0 and the scatter angle φ on the Compton camera angular resolution measure due to the second scatter detector denoted by the term T_2 | 35 |
| Figure 2.4: Atomic Compton profiles for the elements hydrogen, silicon and germanium..... | 37 |
| Figure 2.5: Ribberfors cross section and Klein-Nishina cross section for CdZnTe..... | 37 |
| Figure 2.6: The distribution of the reconstructed scattering angle in 2-Compton mode due to Doppler broadening for three different scattering materials..... | 38 |

| | |
|---|----|
| Figure 2.7: Profiles of the reconstructed scattering angle due to Doppler broadening in 2-Compton mode for different energies and scattering angles..... | 39 |
| Figure 2.8: Distribution of the reconstructed first scattering angle in 3-Compton mode calculated for 2000 events in each distribution..... | 40 |
| Figure 2.9: Profiles of the reconstructed scattering angle due to Doppler broadening in 3-Compton mode for different energies and scattering angles..... | 41 |
| Figure 2.10: Geometrical contribution to the ARM in 3-Compton mode from the measurement of φ_2 at three different incident energies..... | 43 |
| Figure 2.11: Deposited energy in Compton scattering over the incident energy for three different scattering angles..... | 43 |
| Figure 2.12: Flowchart of the simulation of a single photon history in the efficiency simulation..... | 47 |
| Figure 2.13: The contributions to the ARM in 2-Compton mode for three different energies. | 49 |
| Figure 2.14: The contributions to the ARM in 3-Compton mode for three different energies. | 50 |
| Figure 2.15: Simulated efficiency for homogeneous stacks of detectors of different material. The data was simulated with 400 000 events for each point..... | 51 |
| Figure 3.1: The initial detector design was supposed to be constituted of two layers of CdZnTe detectors followed by a larger scintillation plane..... | 55 |
| Figure 3.2: Schematic overview of the camera system..... | 55 |
| Figure 3.3: Left: anode electrode of the CdZnTe detector. Right: cathode side (images by Baltic Scientific Instruments)..... | 57 |
| Figure 3.4: Left: detector assembly from the anode side. Right: cathode side view (images by Baltic Scientific Instruments)..... | 57 |
| Figure 3.5: Front side of the front-end-board which supports the CdZnTe detector and its preamplifiers (drawing by Klaus Heide, HZDR)..... | 58 |
| Figure 3.6: Block diagram of the Nanosecondpreamplifier (by Klaus Heide, HZDR)..... | 59 |
| Figure 3.7: The FE-board fully populated with the detector and all powered up NSP modules. | 60 |
| Figure 3.8: Coordinate system and channel arrangement in the LSO detector..... | 61 |
| Figure 3.9: The detectors in the mounting frame..... | 62 |
| Figure 3.10: Signal paths in the DAQ system..... | 63 |
| Figure 3.11: The logic which is programmed on the V1495 FPGA module..... | 64 |
| Figure 3.12: The populated VME crate with the measurement PC and delay lines..... | 65 |
| Figure 3.13: Implementation of the interface to VME bus operations in <i>libCVME</i> | 67 |
| Figure 3.14: Data flow and thread organization in <i>libCVME</i> | 67 |
| Figure 3.15: Elements for measurement control and data inspection during a measurement. | 69 |
| Figure 3.16: Pedestal measurement for QDC channel alignment..... | 70 |
| Figure 3.17: Typical pulse shapes from the CdZnTe detector. Left: anode, right: cathode..... | 71 |
| Figure 3.18: Single anode pulse height spectrum from the CdZnTe detector..... | 71 |
| Figure 3.19: Distribution of the FWHM at 511 keV among the anode channels..... | 71 |
| Figure 3.20: Single cathode pulse height spectrum..... | 71 |
| Figure 3.21: Spectrum of the sum of all cathode signals per trigger..... | 71 |
| Figure 3.22: Scatter plot of the energy-weighted anode and cathode channel. The anodes 0, 1 and 6 were turned off during this measurement..... | 72 |
| Figure 3.23: Cathode-to-anode ratio over the energy measured on the anode. The color scale indicates the number of entries per bin and is logarithmic..... | 73 |
| Figure 3.24: Typical pulse shape of one of the four PMT from the LSO block-detector..... | 74 |
| Figure 3.25: LSO sum spectrum..... | 74 |

Figure 3.26: LSO interaction map without gain adjustment.....75

Figure 3.27: LSO interaction with gain adjustment.....75

Figure 3.28: Total event energy in a ^{22}Na measurement.....76

Figure 3.29: Cosine of the measured scattering angle corresponding to the events in figure 3.28.....76

Figure 3.30: Cosine of the scattering angle for events with a total energy around 1275 keV..76

Figure 3.31: The same data as in figure 3.30 without energy depositions in the CdZnTe detector around 511 keV. In red: incoherent scattering cross section of 1275 keV.....76

Figure 3.32: Image reconstruction of a ^{22}Na point source.....77

Figure 3.33: Slices through the tenth iteration reconstruction of a point source measurement at the source distance.....78

Figure 3.34: Reconstructed images of a point source at different positions, first iteration ML-EM.....79

Figure 3.35: The same data as in figure 3.34 after five iterations.....80

Figure 4.1: The setup at the AGORFIRM beam line. The beam direction is indicated with a red arrow.....83

Figure 4.2: Reconstructed images of a ^{60}Co source taped on the phantom.....84

Figure 4.3: Beam profile at the entrance (left) and in 10 cm depth (right).....85

Figure 4.4: Trigger rate in dependence on the beam current.....86

Figure 4.5: LSO interaction map recorded during a beam experiment at 50 pA.....86

Figure 4.6: Energy spectra in the CdZnTe and LSO detector and the sum spectrum from coincident data taken during a PE irradiation.....87

Figure 4.7: Reconstruction results from a PE phantom measurement.....88

Index of Tables

| | |
|---|----|
| Table 1.1: Semiconductor Material Properties..... | 19 |
| Table 1.2: Some commonly used scintillators..... | 23 |

List of Abbreviations

| | |
|----------|---|
| ADC | Analogue to digital converter |
| AGOR | Accélérateur Groningen-Orsay |
| AGORFIRM | AGOR Facility for Irradiation of Materials |
| APD | Avalanche photodiode |
| ARM | Angular resolution measure |
| ASIC | Application specific integrated circuit |
| BASTEI | Beta activity measurements at the therapy with energetic ions |
| BGO | Bismuth germanate, $\text{Bi}_4\text{Ge}_3\text{O}_{12}$ |
| CCIDB | Compton Camera Imaging Database |
| CFD | Constant fraction discriminator |
| COBRA | CdTe 0 -neutrino research apparatus |
| COMPTEL | Imaging Compton Telescope |
| DAQ | Data acquisition |
| DPP | Digital pulse processing |
| FE | Front-end |
| FLUKA | Fluktuierende Kaskade |
| FPGA | Field programmable gate array |
| FWHM | Full width at half maximum |
| Geant4 | Geometry and tracking, version 4 |
| GSI | Gesellschaft für Schwerionenforschung, Darmstadt, Germany |
| HEP | High-energy physics |
| HPGe | High-purity germanium |

| | |
|----------|--|
| HZDR | Helmholtz-Zentrum Dresden-Rossendorf, Dresden, Germany |
| IBIS | Imager on-board the INTEGRAL satellite |
| IMRT | Intensity modulated radiotherapy |
| INTEGRAL | International Gamma-Ray Astrophysics Laboratory |
| KVI | Kernfysisch Versneller Instituut, Groningen, the Netherlands |
| LE | Leading edge |
| LET | Linear energy transfer |
| LSO | Lutetium oxyorthosilicate, Lu_2SiO_5 |
| ML-EM | Maximum likelihood expectation maximization |
| MWD | Moving window deconvolution |
| NSP | Nanosecond preamplifier |
| PC | Personal computer |
| PCB | Printed circuit board |
| PE | Polyethylene, $(\text{C}_2\text{H}_4)_n$ |
| PET | Positron emission tomography |
| PMMA | Polymethyl metacrylate, Plexiglass, $(\text{C}_5\text{H}_8\text{O}_2)_n$ |
| PMT | Photomultiplier tube |
| QDC | Charge (Q) to digital converter |
| SiPM | Silicon photomultiplier |
| SPAD | Single photon avalanche diode |
| SPECT | Single photon computed tomography |
| TDC | Time to digital converter |
| TPC | Time projection chamber |
| VHDL | Very high speed integrated circuit hardware description language |
| VME | Versa module eurocard-bus |

0 Introduction

Conventional percutaneous radiotherapy is performed by means of irradiation with bremsstrahlung photons and, to a minor degree by means of electrons. Such treatment devices comprise a compact electron accelerator that is mounted on a gantry which rotates around the patient. The electrons are accelerated to up to about 20 MeV and converted into bremsstrahlungs spectra. Most treatment machines offer photon spectra of 6 MV or 15 MV. These are 1/E spectra with a maximum energy at the electron energy of 6 MeV or 15 MeV, respectively. The machine can rotate freely around the patient and can be equipped with various collimators and wedges to make the radiation field as tumor conformal as possible. Intensity modulated radiotherapy (IMRT) allows even for inhomogeneous dose prescription within the irradiated volume.

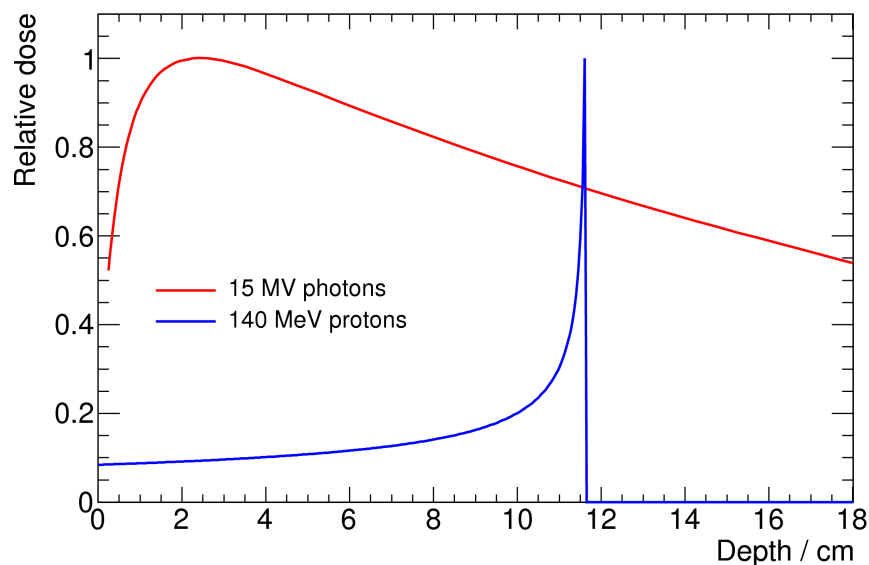


Figure 0.1: Dose deposition in polymethyl metacrylate (PMMA) of photons compared to protons.

However, the dose deposition in depth of bremsstrahlung photons is not ideal since healthy tissue before and after the target volume always receives a considerable amount of dose as illustrated in figure 0.1. Shown is the depth dose curve in polymethyl metacrylate

(PMMA) of 15 MV photons, taken from [Kor09a], and of protons with 140 MeV initial energy which was calculated according to the expression given in [Bor96]. The photon curve increases to a dose maximum in a depth of 2.5 cm. Hereafter, the curve decreases exponentially. In the case of tumors deeper than 2.5 cm, the dose maximum is delivered to healthy tissue.

Ions deposit the most of their kinetic energy at the end of their path through tissue in the Bragg peak. In the case of protons, it is situated in a depth R of

$$R = \alpha E_0^p \tag{0.1}$$

with $\alpha = 1.9 \times 10^{-3}$ cm, $p = 1.8$ for protons in water and E_0 the initial proton energy in units of MeV [Bor96]. Because of this feature, ion beam irradiation can be very tumor conformal in depth by modulating the energy so that the Bragg peak is scanned through the tumor volume (*spread out Bragg peak*). The energy deposition per length (linear energy transfer, LET) increases at the end of the ion path which leads to a high ionization density. This results in a higher density of double strand breaks of DNA which leaves less chance for the cell to repair the damage.

To make maximal use of ion therapy, it is crucial to assure the accuracy of the treatment. That is even more important than in the case of photons because the Bragg peak location is very sensitive for the tissue density. Weight loss of the patient during the therapy or tumor shrinking can lead to beam over- or undershoot.

An established monitoring method for protons and heavier ions is positron emission tomography (PET). One exploits that the projectiles undergo nuclear reactions with the target nuclei to β^+ -emitting nuclei whose decay can be seen on PET images. In the case of proton irradiation, the relevant reactions are $^{12}\text{C}(p,p+n)^{11}\text{C}$ and $^{16}\text{O}(p,p+n)^{15}\text{O}$. ^{11}C has a half live of 20 minutes. The half life of ^{15}O is 2 minutes. In the case of ^{12}C beams, even the projectiles may fragment into ^{11}C . Nevertheless, the so produced activity is still orders of magnitude less than what is common in nuclear medicine. PET monitoring therefore operates in terms of event numbers and count rates always on the low boundary.

A conventional PET ring is not compatible with the beam nozzle because the patient couch needs to be rotated relative to the beam. Therefore, dedicated PET hardware is required to implement PET imaging during the irradiation (in-beam PET). A double head camera can be applied that leaves enough space for the patient to be positioned accordingly. Such a device has been realized in the form of the BASTEI PET camera at the Gesellschaft für Schwerionenforschung (GSI), Darmstadt, Germany (see figure 0.2). This camera has been successfully applied in over 440 cases of carbon irradiation [Sha11]. The accelerator at GSI is a synchrotron. At this machine, there is an interval of 2.4 s between two extractions at a repetition cycle of 4.6 s [Paw97]. The PET camera has been operated between two extraction in order to avoid random coincidences due to promptly emitted γ -rays [Par05].

Another possibility of applying PET verification is to move the patient to a conventional PET ring shortly after the treatment (off-beam PET). This technique has also been successfully applied [Par07]. However, most of the ^{15}O signal is lost due to its short half life. The further amount of signal loss depends on whether the PET scanner is located in the treatment room or outside. A detailed discussion of the expected image quality and the costs of dedicated PET systems for beam monitoring is done in [Sha11]. The best image quality is expected from in-beam PET while a scanner in the treatment room is a good compromise of image quality and cost.

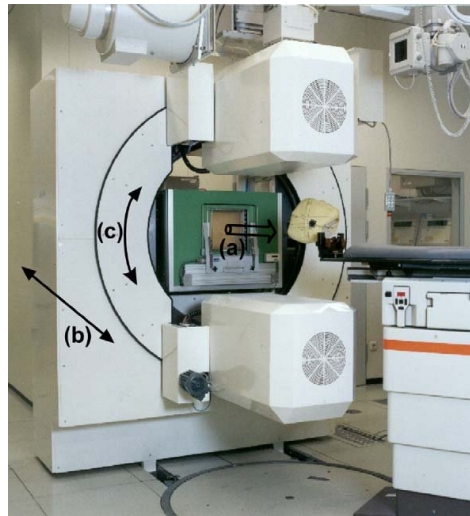


Figure 0.2: Double head in-beam PET camera system BASTEI at GSI, Darmstadt [Eng04]. The beam enters at position (a). The camera is mounted on rails and can be retracted for easier patient positioning (b). The heads can also rotate around the patient to allow for treatments in sitting position (c).

PET verification has been proven to be a feasible method. However, several limitations remain:

- (1) *Limited angle artifacts:* As already mentioned, the treatment nozzle is not compatible with a full ring scanner since the patient has to be rotated relative to the beam axis. Only a camera in double head geometry is possible. This is in most cases sufficient to determine the beam range. But the activity appears to be elongated along the connection of the two heads because of the missing information perpendicular to this direction. Moreover, the per se low event number is further reduced through the incomplete solid angle coverage.
- (2) *Dedicated hardware:* PET scanners for nuclear medicine are integrated systems with dedicated computing hardware and reconstruction methods. Reducing the full ring scanner to a double head camera operated synchronously to the accelerator requires a considerable amount of engineering which can only amortize if these devices can sell at a certain number. The number of treatment facilities suitable for the installation of in-beam PET cameras is however limited.
- (3) *Hard to install at cyclotrons:* The aforementioned limitation would not be so restricting if in-beam PET devices could easily operate at cyclotrons. The cyclotron pulse structure however leaves only short pauses typically a few ns for the acquisition of PET data. The beam is extracted more or less continuously (*continuous wave mode* – *cw mode*) while a synchrotron facility has longer periods between extractions during the filling and acceleration phases. Most newly installed ion beam facilities offer proton beams which are most efficiently accelerated in a cyclotron.
- (4) *Metabolic washout:* The generated PET nuclides are subject to the blood flow and other metabolic processes. Especially in the brain many transport processes take place. This leads to a rather fast reduction of the activity. This is not so much an issue for the data taken directly during the irradiation. As mentioned in (3), cyclotron

facilities do not allow for the data to be taken in beam pauses. So off-beam PET is the only option in these cases. Moving the patient to the scanner takes time in which the image degrades by the mentioned mechanism.

- (5) *Low statistics*: In nuclear medicine, an activity of more than 100 MBq is usually applied. In PET verification, the induced activity is two or more orders of magnitudes less. Additionally, the solid angle covered by the double head camera in the BASTEI device is only 8 %. In the case of off-beam PET activity is lost due to the time delay. The images quality is for the purpose of range verification sufficient. But especially for parts with low dose gradient in beam direction, better statistics would be advantageous.
- (6) *Prolonged treatment time*: Acquiring data after the treatment in in-beam PET occupies the treatment room. Off-beam PET may be logistically preferential but still leaves an additional step in hospital routine which requires time on equipment and staff and thereby increasing the cost of ion irradiation [Sha11].
- (7) *No quantitative method*: The PET camera does not record “dose images”. An inverse calculation of the dose from recorded activity is not feasible due to the metabolic washout as outlined in (4). PET verification therefore remains a qualitative method.

0.1 Motivation

The analysis above makes it desirable to explore alternative methods to PET verification despite its successful record. The annihilation radiation following the decay of β^+ -radioactive nuclei produced by nuclear reactions between the beam and the target is only one kind of radiation that is suitable to be detected spatially resolved and allow conclusions on the interaction site. The annihilation radiation has however the advantage that there is a mature medical imaging technology available. Other emitted particles are*:

- Photons
- Neutrons
- Protons
- α -particles
- Other light nuclei, leptons and mesons.

All of these can potentially be used for treatment verification since they all originate in the interaction of projectile and target nuclei. The technology to track and determine the origin of any of these particles has already been developed in astrophysics and high energy physics (HEP). However, the demands on count rate capability and accuracy differ from the clinical case. Existing techniques have to be translated and adapted to show the clinical feasibility of the method.

*) Roughly in order of abundance; this depends on the beam parameters and the target material

There is much experience within HEP with tracking detectors for charged particles. Consequently, there are efforts to apply this technology to track the protons emitted from the patient [Tes12]. Tracking detectors can even be used as vertex detectors which even more resembles the HEP application. In the case of antiproton irradiation, the annihilation process at the end of the antiproton path emits pions which could theoretically be used like the annihilation radiation from the β^+ decay in PET monitoring [Kan10].

As high energy physics provides mostly detector technology for charged particles, there is much knowledge in the detection of photons in nuclear physics and astrophysics. Astronomy is interested in nuclear processes. These are often associated with the emission of photons in the MeV energy range because this is the order of magnitude which separates nuclear energy levels. Similar reactions take place during hadron irradiation. These photons are of similar origin like the ones astrophysics is interested in. The application of astrophysical imaging techniques to radiation therapy is therefore a coherent step towards new modalities of dose monitoring.

0.2 Task

Astrophysical imaging techniques for photons include coded aperture imaging and Compton telescopes. The former relies on an absorbing mask in front of a location sensitive detector. This is probably hard to implement in the clinical case since there are practical restrictions on the mass of the absorber[†]. The latter technique does not need passive materials and consequently can potentially have a higher efficiency. Compton telescopes have a long successful record in astrophysics for recording MeV γ -rays. The technology is described in depth in chapter 1.4. The aim of this work is to explore the potential of Compton imaging for in-vivo dose monitoring in hadron therapy. Major steps for this purpose are:

- (1) Evaluate the expected performance of a Compton camera system by means of calculation and simulation with respect to clinical conditions. This has to lead to a promising setup in terms of geometry and possible detector materials.
- (2) Based on these considerations construct a system capable of actual image recording with available components to validate the considerations and to provide real data for the development of image reconstruction methods.
- (3) Test the developed system at a beam experiment to gain further knowledge on the limitations and problems arising from the actual application case.

The considerations of point (1) are presented in chapter 2. The evaluation system which has been developed is shown in chapter 3 while chapter 4 describes the performed beam experiment. In chapter 5 conclusions are drawn on the gained experience with Compton imaging for dose monitoring. But first of all, more details on the physical processes and technologies which are relevant for this work are described in chapter 1.

[†]) However, there are very promising approaches which rely on absorbers [Pel11].

1 Physical Background

This work is about the interaction of radiation with matter and the quantification of these interaction events with the help of radiation detector technology. In this introduction chapter, the most important interaction modes are discussed and the relevant measurement technologies are presented. This includes not only detector materials but also readout and analysis techniques. Signal formation in semiconductor detectors is especially emphasized since the CdZnTe detector in the developed Compton camera is a central component. This material is far from a perfect detector material and a close look at the charge collection process is required to achieve the best possible results.

1.1 Interaction of Ionizing Radiation with Matter

The Compton camera has its name from the Compton effect, the incoherent scattering of a photon off a free electron. This modality and the other interaction modes of photons with matter shall be discussed here. The effects are roughly ordered for the photon energy at which they dominate the total cross section. Additionally, the charged particle transport will be touched as most photon interactions result in fast electrons that travel through matter.

1.1.1 Coherent Photon Scattering

This interaction modality implies no change in wavelength and thereby no energy modification, nor is the phase of the photon shifted, i.e. the incoming and the outgoing photons are coherent. Nevertheless, the direction can be altered. This scattering process can be described entirely classically. In this perspective, an electron is stimulated to oscillate due to the alternating electric field which makes the photon. The oscillating motion results in the emission of dipole radiation which is coherent to the stimulating field. In the mentioned case of the scattering entity being an electron, this process is referred to Thomson scattering whose differential cross section is

$$\frac{d\sigma}{d\Omega} = \frac{r_e^2}{2} (1 + \cos^2\varphi). \quad (1.1)$$

(φ : scattering angle, r_e : classical electron radius)

If the whole atom or molecule is the scatter center, this kind of interaction is named Rayleigh scattering. Although (1.1) has no energy dependence, this is not strictly true since the description of the problem leading to the Thompson cross section is only valid if the wavelength of the exciting field is much larger than the scale of the scatter center size. This limits the relevance of Rayleigh and Thompson scattering to optical processes. Despite this, coherent scattering leads to very interesting phenomena like the fact that the sky in the absence of clouds is blue and polarized, coherent photon scattering has little to no relevance for this work and a detailed discussion goes well beyond its scope.

1.1.2 Incoherent Photon Scattering

The scattering of a photon off a free electron is referred to as Compton scattering named in honor of Sir Arthur Holly Compton who first described this process in kinematic terms in 1923 [Com23]. In the description it is necessary to treat the photon like a massive particle. The Compton effect was therefore after the photoelectric effect described by Einstein another indication for the corpuscular nature of light.

The respective Feynman diagram of the u - and s -channel are shown in figure 1.1*. If the electron is at rest in the laboratory frame before the event, the following relation holds for the angle φ between the direction of the incoming photon and the scattered photon and their respective energies E_0 and E_1 :

$$\cos\varphi \equiv \mu = 1 - mc^2 \left(\frac{1}{E_1} - \frac{1}{E_0} \right). \quad (1.2)$$

This relation can be deduced with the help of energy and momentum conservation only. The maximal energy is transferred to the electron in the case of backscattering where $\cos\varphi = -1$.



Figure 1.1: The two Feynman graphs of Compton scattering (first order, s - and u -channel).

The differential cross section for the scattering off a free electron has first been derived by Oskar Klein and Yoshio Nishina in 1929 [Kle29]. The application of relativistic quantum mechanics yields the following cross section:

*) In all Feynman diagrams in this work time runs from left to right. The t -channel in Compton scattering does not exist because it would involve an unphysical vertex where a photon emits a lepton and continues as photon.

$$\frac{d\sigma}{d\Omega} = \frac{r_e^2}{2} \frac{1}{[1+\varepsilon(1-\mu)]^2} \left[1+\mu^2 + \frac{\varepsilon^2(1-\mu)^2}{1+\varepsilon(1-\mu)} \right], \quad \varepsilon = E_0/mc^2. \quad (1.3)$$

An electron may be considered as “free” if the energy which is transferred to it, is much larger than its binding energy, hence

$$E_b \ll E_0 - E_1. \quad (1.4)$$

In heaviest elements, the binding energy of the *K*-shell is in the order of 100 keV and condition (1.4) might not be sufficiently fulfilled to neglect the electronic binding completely. In the view of the Feynman diagram, the binding is introduced by the exchange of a virtual photon between the electron and the core, which at this energy scale may be seen as a single unit (figure 1.2).

Instead of calculating the matrix element of figure 1.2, an intermediate approximation can be applied which includes the electronic motion within the atomic orbitals. This is referred to as *impulse approximation* (sic) [Rib75]. Because this approximation has been used to estimate the deviation from the ideal relation (1.2) in simulation code on the expected performance of the Compton camera, it will be discussed in more detail in section 2.

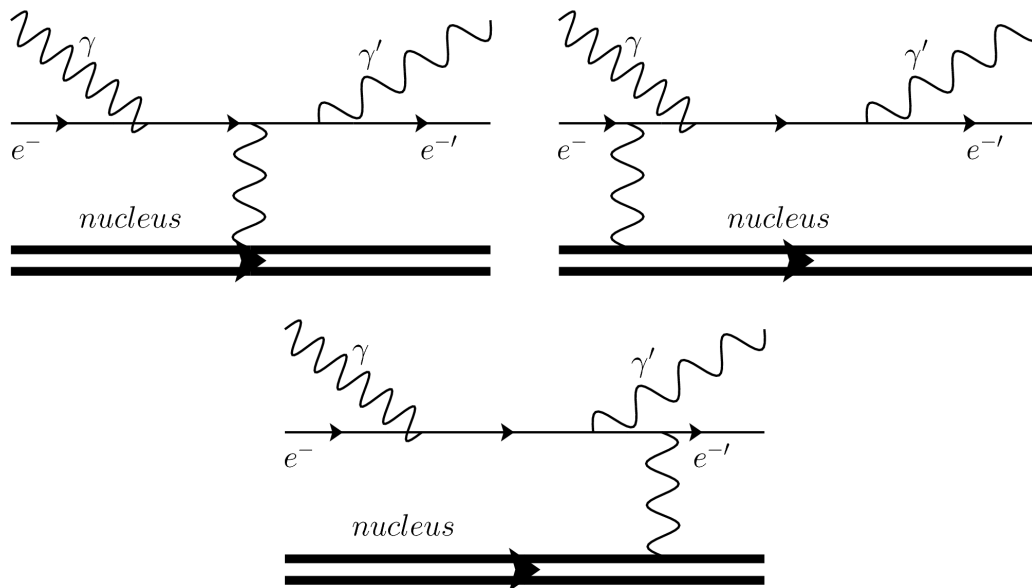


Figure 1.2: Three Feynman graphs of the incoherent scattering of a photon off an electron bound to a nucleus.

1.1.3 Complete Absorption in the Nuclear Electric Field

In this process, which is also referred to as photoelectric effect, a single electron of the atomic shell absorbs the total energy of an incident photon. Since the allowed energy band for the electron becomes only continuous outside the atom, the effect is energetically only allowed for photon energies greater than the binding energy of the electron under consideration.

Albert Einstein was the first to recognize that a single electron takes all energy of the photon in 1905 [Ein05] why the Nobel Prize was awarded to him. This was one point which

lead to the complementary description of the photon as wave (c.f. coherent scattering) and as a particle at the same time. However, the complete quantum electrodynamical description of the process was delivered by Fritz Sauter in 1931 [Sau31]. The most important feature of the cross section is

$$\sigma \propto Z^5 E^{-7/2} \tag{1.5}$$

on a wide energy range. It is highly dependent of the atomic number of the medium Z and drops steeply with increasing energy.

The electron leaves a vacancy in the shell. This vacancy is filled with electrons of higher states. In this process, additional radiation is emitted. This can be X-ray photons with the energy which become free when the electron “drops” in place, or the energy is transferred to other electrons which leave the atom as Auger electrons.

1.1.4 Pair Production

If sufficient energy is present, a photon can convert into a particle-antiparticle pair in the presence of matter. This can occur if the photon energy is larger than the rest energy of the particle-antiparticle pair. The lightest pair is the electron-positron pair with a combined rest mass of 1.022 MeV which is why the conversion of a photon in such a pair is the most commonly observed pair production process.

For a non-virtual particle pair the presence of another particle is required. Otherwise, the process is forbidden due to energy and momentum conservation. The Feynman diagram of a photon converting into an electron and a positron is shown in figure 1.3.

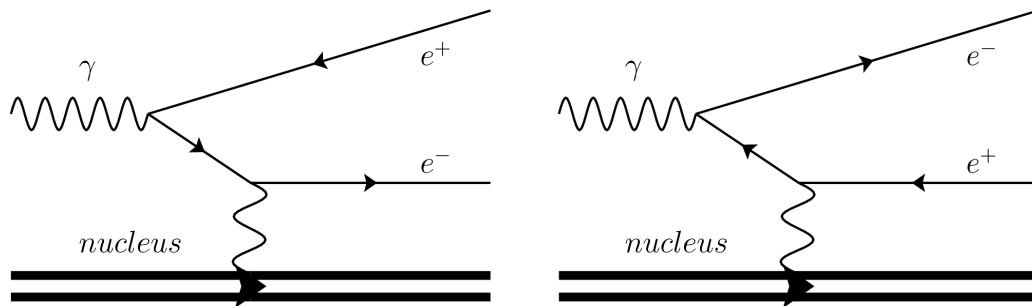


Figure 1.3: Two possible crossing channels of the pair production in the nuclear electric field. The exchange of the virtual photon between one of the resulting leptons and the nucleus is mandatory for momentum conservation.

The cross section is [Lan91]

$$\sigma = \frac{1}{2\pi} \frac{28}{9} Z^2 \alpha r_e^2 \left(\ln \frac{2E_0}{m_e c^2} - \frac{109}{42} \right), E_0 \gg m_e c^2. \tag{1.6}$$

Materials with a high atomic number are good conversion targets. The cross section increases smoothly with energy.

The antiparticle annihilates mostly at the end of its path so that the pair production is accompanied by annihilation radiation.

Momentum conservation allows for determining the incident direction of the photon if the momentum of the emerging electron and positron can be measured. This is the basis for

pair production telescopes which can be used to determine the origin of γ -rays with an energy of several MeV. A pair production camera is an approach which has also been pursued for imaging the high energetic photons emitted during radiotherapy. Even a pair production upgrade to the device developed in this work was discussed [Gol11]. However, this approach will not be addressed further here.

1.1.5 Total Photon Cross Section

The different processes of 1.1.1 to 1.1.4 add up to the total cross section. It is commonly expressed in terms of the macroscopic cross section divided by the mass density μ/ρ . This quantity is referred to as mass attenuation coefficient. μ is the inverse of the mean free path and is connected to the microscopic cross section σ via

$$\mu/\rho = \sigma N_A / M \tag{1.7}$$

where M is the molar mass of target entities σ refers to – usually atoms or molecules. The mass attenuation coefficient μ/ρ for CdZnTe is plotted over the incoming photon energy in figure 1.4.

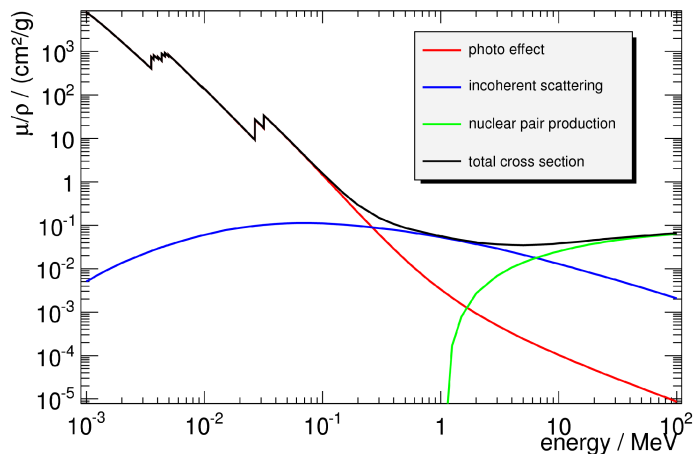


Figure 1.4: Mass attenuation coefficient μ/ρ of CdZnTe [XCOM].

1.1.6 Directly Ionizing Radiation

So far only the interaction of photons with matter has been discussed. Photons, together with neutrons are considered as indirectly ionizing radiation because they transfer their energy to charged particles. These secondary particles transfer their energy in a large number of interactions to matter. Charged particles are therefore considered as directly ionizing particles. On their path through matter they excite or ionize numerous atoms due to the Coulomb interaction with the shell electrons. It is also possible for charged particles to radiate photons which are referred to as bremsstrahlung.

The total energy loss per unit length or stopping power, dE/dx , is the sum of the collision stopping power and the radiative stopping power. The energy loss has first been derived comprehensively in [Bet32]. The most important dependencies are:

$$\begin{aligned}
\left(-\frac{dE}{dx}\right) &= \left(-\frac{dE}{dx}\right)^{(\text{collision})} + \left(-\frac{dE}{dx}\right)^{(\text{radiation})} \\
\left(-\frac{dE}{dx}\right)^{(\text{collision})} &\propto Z m, \\
\left(-\frac{dE}{dx}\right)^{(\text{radiation})} &\propto Z^2 E_0/m^2.
\end{aligned} \tag{1.8}$$

The mass m of the particle plays a crucial role for its energy loss characteristics. For energies of up to a couple of MeV, only the lightest particles electrons and positrons lose a considerable amount of energy due to bremsstrahlung. Target materials with a high atomic number Z increase the radiative fraction.

Beside the inelastic scattering which transfers energy from the incident particle to the scattering medium, elastic scattering is also possible which changes the direction only. This is especially important for lighter charged particles like electrons, where the mass of the beam particles is negligible compared to that of the target particles.

1.2 Prompt γ -rays from Nuclear Reactions

Projectile and target particles undergo various reactions that can yield γ -ray emission. According to the classification in [Fou10], the following reaction mechanisms are of relevance:

- *Nucleon-nucleon bremsstrahlung*: The projectile particles radiate photons as they slow down. This mainly results in photons with an energy of more than 30 MeV.
- *Collective de-excitation*: The projectile and the target nucleus can form a compound nucleus which can be in an excited collective state, referred to as Giant Resonances. The transition between such a state and the collective ground state is usually accompanied by the emission of γ -rays with an energy between 10 MeV and 30 MeV [Fou10].
- *Statistical de-excitation*: The fragments of the compound nucleus are left in a highly excited state close to the evaporation level where nucleons can leave the nucleus. Assuming a Fermi gas model for the nucleus, it can de-excite under the emission of γ -rays with an average energy of 2 MeV to 3 MeV [Mol62]. Because the density of allowed states is high, the emission spectrum appears to be continuous. Because the photons do not only carry away energy but also angular momentum, states with lower angular momentum emit fewer photons. Bombardment with light nuclei like protons induces a smaller angular momentum than heavier projectiles [Mol62]. One therefore expects fewer statistical photons from proton irradiation than from irradiation with heavier nuclei.
- *Discrete γ -ray emission*: Deeper lying energy levels are separated by several MeV. The transition between these levels can therefore be clearly identified by the emission of characteristic γ -rays. Tissue mostly comprises the elements hydrogen, oxygen and carbon. Expected γ -ray energies are therefore:

- 2.2 MeV: ${}^1\text{H}(n,\gamma){}^2\text{H}$,
- 4.4 MeV: ${}^{16}\text{O}$ de-excitation and
- 6.1 MeV: ${}^{12}\text{C}$ de-excitation.

For this work, it would be advantageous to have emission data from tissue-equivalent material available. However, at the time of writing, there are only few experimental data available to build upon [Pol09]. The mentioned γ -ray emission mechanisms can be handled by Monte Carlo simulation code. Work has been going on and there is data available, e.g. [Ric11][Fie10a]. The spectra however are not entirely congruent. The reason might be that different simulation codes – be it FLUKA or Geant4 – have been used. The codes are usually tuned to give the correct energy deposition because this is what usually is of interest in the analysis, either for the expected detector response or for dose curves. The particle number might therefore not be correct in any simulation step as long as the energy, the particle carries, is in the end deposited correctly[†]. But simulation codes for gathering the emission spectrum in ion beam therapy are just querying the particle type and sorting its energy in a spectrum. Even worse, the framework Geant4 allows to chose the type of nuclear model to use for nuclear reactions. It has been shown that the total photon yield and the spectral composition is very sensitive to the chosen model [Fie10]. This is obvious since the production mechanisms, especially for the statistical γ -rays, builds upon the nuclear density of states and their transition probability.

An example of a simulated γ -ray spectrum is shown in figure 1.5. This is a pure emission spectrum with no account for detector resolution. On a continuous background stemming from nuclear bremsstrahlung, collective de-excitation and most notably statistical γ -rays, discrete γ -lines are situated which come from the de-excitation of deeper nuclear states. Especially the continuous component shows some peculiar features like the shoulders visible at some lines. Such features might be model dependent and are therefore not discussed here any further.

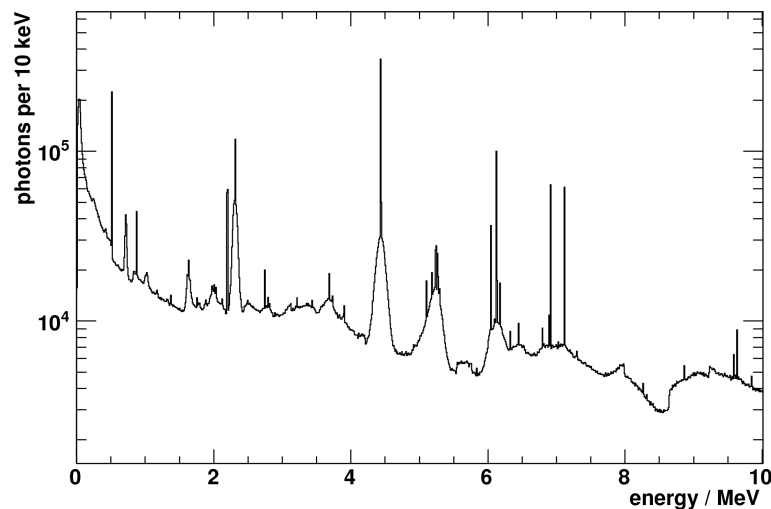


Figure 1.5: Photon emission spectrum from a water phantom irradiated with 200 MeV protons, simulated with Geant4 [Fie10a].

[†]) Private communication Jürgen Henniger, University of Technology Dresden, 2011.

1.3 Detector Technology

The detection of ionizing radiation in real-time relies on the creation of free charge carriers within an electric field. The field leads to a motion of the charge that induces a current on sensing electrodes. The induced current is amplified and measured by subsequent electronics.

If indirectly ionizing radiation is the subject of interest, the measurement current is induced by secondary particles that emerge from an interaction such as the photo electron or the Compton electron which in turn ionizes the detector material. In a semiconductor detector the interaction and the charge collection take place in the very same volume. A scintillation detector however converts the generated charge into light. This light is converted back into charge in a secondary photo detector.

In general, it is required that the charge collection time is small compared to the time interval between two events. Moreover, the total amount of generated charge should be proportional to the deposited energy E_{dep} . In semiconductor detectors the constant of proportionality is the mean excitation energy or pair energy E_{pair} , i.e. the mean energy that is required to excite an electron from the valence band where a hole is left into the conduction band. Voltage across the semiconductor lets the electrons and holes drift towards the electrodes. This movement induces the signal. Signal formation in semiconductors is discussed in more detail further down. The number of electron-hole pairs is

$$N_{\text{eh}} = E_{\text{dep}}/E_{\text{pair}}. \quad (1.9)$$

In scintillators, the proportionality is commonly expressed in terms of the number of generated photons per amount of deposited energy. These photons are converted in a photo detector into charge. This is discussed in more detail in 1.3.2.

The theoretically achievable resolution of the energy measurement is closely connected to the number of free charge carriers N_{pair} . Applying Poisson statistics gives the fluctuation of the mean number of charge carriers as

$$\sigma_{\text{pair}} = \sqrt{N_{\text{pair}}}. \quad (1.10)$$

However, this only holds if the formation of each electron hole pair is completely independent. Observations indicate that this is not the case and (1.10) has to be corrected by introducing the Fano factor F :

$$\sigma_{\text{pair}} = \sqrt{F \cdot N_{\text{pair}}}. \quad (1.11)$$

The resolution R is commonly expressed as the full width at half maximum (FWHM) in percent of the mean position of a peak. Assuming the transition from Poisson to Gaussian statistics and changing to FWHM instead of the standard deviation this gives

$$R = 2.35 \cdot \sqrt{F/N_{\text{pair}}} = 2.35 \cdot \sqrt{F \cdot E_{\text{pair}}/E_{\text{dep}}}. \quad (1.12)$$

A low E_{pair} gives a good energy resolution.

The Fano factor in semiconductors is considerably less than 1 which makes them perform better than predicted from Poisson statistics. Scintillators however mostly have a Fano factor close to unity.

This only describes the contribution to the resolution from the initial fluctuation of the number of generated charge carriers. Other effects especially concerning the charge collection and influences from the electronics are not included in this step. All sources of uncertainty add up quadratically to the total resolution:

$$R^2_{\text{tot}} = R^2_{\text{statistical}} + R^2_{\text{electronics}} + \dots \quad (1.13)$$

Pulse Shaping

Once the current is induced on the electrodes it has to be converted to voltage in order to be eligible for further processing. This is the task of the preamplifier and the following pulse processing chain. The preamplifier provides a voltage signal that is proportional to the induced charge. The simplest circuit diagram of a preamplifier contains an operational amplifier, a capacitor which provides the conversion from charge to voltage, and a resistor that is the simplest form of reset circuitry to keep the signal from rising indefinitely. The circuit is shown in figure 1.6. Real preamplifiers contain much more features like filters for a clean power supply and more to provide a clean signal. This is especially important in this first stage of signal processing since all noise introduced at this level will be amplified.

One is typically interested in the height of the signal which is proportional to the induced charge and the time the signal starts to rise. There are several methods to extract this information. With the wide availability of fast digitization electronics and field programmable gate arrays (FPGA) capable to perform real time processing in the time regime of radiation detector pulses, it became feasible to apply these mathematics digitally. The algorithm used most widely for determining the pulse height is the Moving-Window-Deconvolution (MWD) algorithm first described in [Geo93]. It retains the shape of the leading edge and corrects for the discharge of the preamplifier during the pulse rise time (ballistic deficit). The baseline of the output is close to zero. In the event of a pulse, the signal returns to the baseline as fast as possible. The height of the output can be used as a direct measure for the deposited energy. This is the basic idea behind pulse shaping for spectroscopic analysis. More details on the MWD algorithm can be found in the original publication [Geo93] and in [Kor09a].

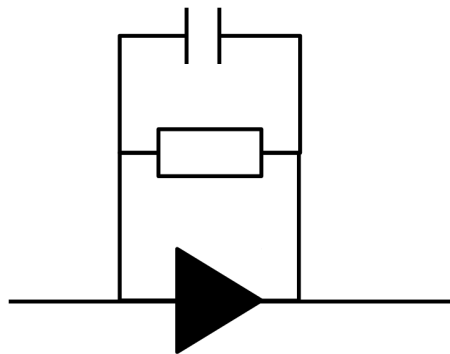


Figure 1.6: Circuit diagram of the simplest case of a preamplifier.

There are several possibilities to extract the energy information in analogue pulse processing. Here the pulse is first shaped and then an energy-proportional figure is extracted from the shaped pulse. Most commonly used are:

- *Peak height*: A differential circuit followed by a chain of integrating circuits (CR - $(RC)^n$) is applied to the preamplifier output. With increasing number of integrators, the output approximates a Gaussian pulse whose amplitude can be analyzed by dedicated devices.
- *Integral*: A reset is applied to the pulse in a defined manner so that the integral of the shaped pulse remains finite. This can be done with a single RC shaping circuit for example. The shaped pulse is fed into “charge-to-digital-converter” (QDC) that integrate the pulse.
- *Time over threshold*: If it is made sure that the pulse returns to the baseline, the time it is above a defined threshold can also be used as a measure for the energy. “Time-to-digital-converter” (TDC) provided with the output of a dedicated discriminator can measure the time between the threshold crossing.

For many applications a precise point in time is required which defines the arrival of an event. The aim is to convert the analogue voltage signal into a digital signal which is zero in the absence of an event and rises to one when an event occurs. This is especially important for the clinical application of the Compton camera in order to find the two interactions that make a valid Compton event.

The simplest method is to apply a threshold. When the signal crosses the threshold, the digital output is set to one. This is referred to as leading edge trigger (LE). A drawback of this timing method is that it depends on the pulse height. This leads to a variation (jitter) which makes these timestamps less reliable than those of a method which is independent of the pulse height.

An established method is the constant fraction discrimination (CFD). This can also easily implemented in digital pulse processing (DPP). Here, the trigger is generated when the pulse reaches a fraction, often 0.2 to 0.3, of its final amplitude. This gives an accurate timestamp for larger and for smaller pulses. It requires however the knowledge of the height that is finally reached. In DPP this can be extracted by first applying the MWD. Since MWD conserves the rising edge, the very same dataset can be used. In analogue signal processing, a delay line is required with a delay in the order of the rise time. Then, a damped and inverted pulse is added to the delayed pulse. It can be shown that the resulting function crosses the baseline when the original pulse has reached the fraction of the damping factor.

Especially system with a large number of signal channels pose a challenge to the analogue implementation of a CFD because the delay lines, which are most commonly made from coaxial cables for shielding, require much space. Therefore, CFD timing is often not suitable for highly granular systems although it would be desirable.

1.3.1 Semiconductor Detectors

Semiconductor detectors offer the advantage that the interaction and the charge sensing takes place in the very same volume. Because of this, spatial resolution can be achieved by segmenting the electrodes. Photolithographic methods practically put no constraints on the electrode design. Highly granular semiconductor detectors are therefore easy to produce compared to scintillation detectors where additional effort has to be put into segmented light guides and photodetectors.

While a granular readout is easily achieved, the detector material itself needs to be uniform across the entire sensitive volume. For the detection of X-rays or charged particle tracking only very thin slices – often less than 100 μm – are needed. Moreover, in many applications it is sufficient to apply a trigger and have no energy information. But for the energy sensitive detection of high energetic γ -rays, a large volume with good charge transport properties is required. Depending on the crystal growth technique, single crystals with few defects of several cm^3 are very rare. In consequence, demanding large crystals with good charge transport properties (few defects) leads to a large amount of degraded material which naturally drives the price. However, the superior properties are often worth the price. Most common semiconductors applied in nuclear instrumentation are silicon, high purity germanium (HPGe) and cadmium zinc telluride (CdZnTe). After a general discussion of the most important features of semiconductor photon detectors, CdZnTe will be discussed in some more detail because of the relevance for this work.

The atoms in a semiconductor are arranged in a lattice structure. While the innermost electronic orbitals are not affected by this arrangement, the outer orbitals form valence bonds that unify in a periodic structure to de-localized states in which electrons can move freely across the entire lattice volume. They can thereby contribute to an electrical current across the device. The configuration of the allowed states is referred to as bandstructure. The most important characteristic of a semiconductor is the energetic distance between these two bands, the bandgap. It is typically in the order of one electron volt. In case the valence band and the conduction band are separated by 5 eV or more, the material is considered as an insulator.

In a semiconductor, the localized orbitals (valence band) are fully occupied while the de-localized states (conduction band) are unoccupied[‡]. If the energy is supplied to an electron to cross the band gap, it can be elevated to an excited state. Each excited electron leaves a vacancy (hole) behind in the valence band. Both states are considered as charge carriers and can contribute to electrical current as they can move across the lattice.

The charge carrier concentration can be altered by replacing some of the lattice atoms. If, for example, in a silicon bulk, some Si atoms (group IV) are replaced with atoms of group V (e.g. P), there are additional electrons which take not part in the valence bonding. These electrons are free to move without their hole counterparts. A material like this is referred to as *n*-type semiconductor. Similarly, atoms of group III result in a deficit of electrons (hole excess) which make the material a *p*-type semiconductor.

Thermal energy that is shared among the electrons gives rise to a certain number of excited states. The number of these excited states obeys Fermi statistics. The probability P that such a state is generated in the time interval τ_{readout} is

$$P \propto \tau_{\text{readout}} T^{3/2} e^{-\frac{E_g}{2k_B T}}. \quad (1.14)$$

Thermally excited states lead to a thermal current whose fluctuation causes thermal noise. Keeping (1.14) low is therefore desired. This can be achieved with a short readout time τ_{readout} , a low temperature T or a large bandgap E_g . The latter however is required to be small according to (1.12), since the pair creation energy is closely connected to the band gap. In practice one attempts to keep T low. Cooling is often costly and requires a consider-

[‡]) That is in the absence of excited states, which implies a temperature of 0 K.

able amount of engineering effort. Semiconductors like high purity germanium (HPGe) are not operable at room temperature. CdZnTe however has a larger band gap and can be operated without cooling, but at a worse resolution than HPGe.

Excited electrons can recombine with holes and get thereby lost in the charge collection process. Most common is the recombination through “traps”. These are states close to the middle of the bandgap (deep defects) which are accessible for holes as well as for electrons. Once an electron enters such state, it might be localized in this state for some time. If during this time a hole enters this state, too, the recombination takes place and leaves the defect state unoccupied and ready for the next recombination. Such states are introduced by impurities and crystal imperfections like cracks. The mean lifetime between creation and recombination of a charge carrier τ_e for electrons and τ_h for holes are other important numbers of a semiconductor. τ_e and τ_h may be very different.

As excited states are present – either through thermal or external excitation – they start to move as an electric field is applied. Electron states in the conduction band and holes in the valence band propagate differently. Their respective velocity v is however proportional to the electric field across the bulk \vec{E} :

$$\begin{aligned} v_e &= \mu_e |\vec{E}| \\ v_h &= \mu_h |\vec{E}| \end{aligned} \quad (1.15)$$

The proportionality constants μ is referred to as mobility.

This motion induces charge on the sensing electrodes which makes the detector signal. Following (1.9) the generated charge is proportional to the deposited energy. The induced charge can be calculated with the Shockley-Ramo theorem^s [Sho38][Ram39]. Accordingly, a charge Q_0 moving from \vec{r}_1 to \vec{r}_2 induces a charge

$$Q_i = Q_0 [\Phi_i(\vec{r}_2) - \Phi_i(\vec{r}_1)] \quad (1.16)$$

on electrode i . $\Phi_i(\vec{r})$ is called weighting potential of the electrode i . It is a dimensionless quantity which presents the potential which would be present if the sensing electrode is held at unit potential and all other electrodes at zero potential. For simple cases, it can be calculated analytically. Most real cases require to solve the Laplace equation numerically to obtain the weighting potential. In a planar detector with thickness L the weighting potential of the anode in distance d of the cathode is

$$\Phi(d) = d/L. \quad (1.17)$$

If N_{eh} electron-hole pairs are created in depth d , and all created electrons and holes drift the whole way to the anode and cathode, respectively, the induced charge is

§) The concept of the weighting potential was discovered independently by William Shockley and Simon Ramo. Both were driven by the tediousness of the calculation of the induced charge using the Green's function method to solve the Laplace equation and then computing the surface integral of the electric field around the electrode in focus. Their theorem was first described for vacuum and only later extended for semiconductors [Jen41]. Discussions on the validity in presence of space charge went on for some time but were eventually settled [Cav71].

An excellent review of the Shockley-Ramo theorem in the context of CdZnTe detectors is [He01].

$$Q_{\text{anode}} = Q_e + Q_h = -eN_{\text{eh}}(L-d)/L + eN_{\text{eh}}(0-d)/L = -eN_{\text{eh}}. \quad (1.18)$$

It is noteworthy that the induced charge does not depend on the applied voltage nor on the depth. This holds as long as there is no internal amplification which is not the case for ordinary semiconductors. It can however be achieved with specially doped layers. This is exploited for some kinds of low light sensors and is discussed briefly when scintillation detectors are presented.

Equation (1.18) implies that the output pulse on each electrode is affected by the motion of both types of charge carriers. A pulse in a planar detector has therefore two components that contribution is a function of the depth as illustrated in figure 1.7. Here a model has been assumed where the electrons move five times as quick as the holes.

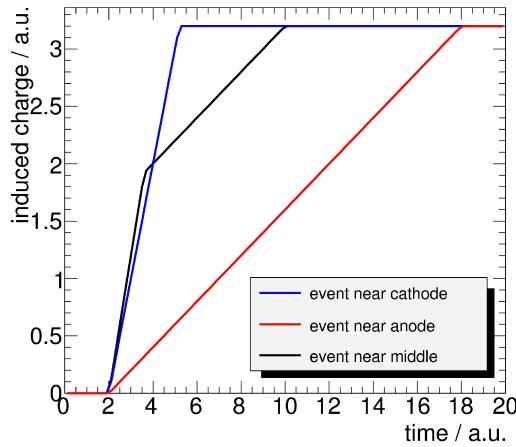


Figure 1.7: The induced charge on the anode in the absence of charge loss as a function of time for interactions that take place near the cathode, near the anode and halfway in between. There is a steep rise in the induced charge due to the fast movement of the electrons when the event takes place close to the cathode, i.e. when the holes do not induce any signal. Events close to the anode produce only the slower hole signal. Hits in the middle result in a superposition.

The different pulse shapes at different depths can be the starting point to gain depth of interaction information by estimating the relative contribution of the steep electron part and the flat hole part. However, it requires that holes and electrons can actually cross the entire detector volume and are not trapped completely before reaching the respective electrode. This implies that the mean lifetime of electrons and holes must be large compared to the drift time. Using (1.15) this gives

$$\frac{L}{\mu\tau|\vec{E}|} \ll 1. \quad (1.19)$$

Aside from the material properties μ and τ one can try to achieve condition (1.19) by making the detector thinner or increasing the voltage. This is however restricted by the dark current fluctuations. Even if (1.19) is reached for electrons, it cannot always be assured for holes. The detector has then a charge collection efficiency ϵ less than 1 which is described by the Hecht equation [Hec32] for the case of a planar detector and when neglecting de-trapping:

$$\varepsilon_{\text{anode}} = \frac{Q_{\text{anode}}}{Q_0} = |\vec{E}| \left[\frac{\mu_e \tau_e}{L} \left(1 - e^{-\frac{L-d}{\mu_e \tau_e |\vec{E}|}} \right) + \frac{\mu_h \tau_h}{L} \left(1 - e^{-\frac{d}{\mu_h \tau_h |\vec{E}|}} \right) \right] \quad (1.20)$$

The charge loss not only has negative effects but can also be used to calculate d if ε can be estimated. This is discussed for the case of CdZnTe further down.

Three semiconductor materials commonly used in nuclear instrumentation are listed in table 1.1. All three have been considered for application in this work. The choice of material is discussed in chapter 2. Some features of CdZnTe shall be discussed here because this material has been chosen later. It has many advantages but the very different transport properties of electrons and holes require special measurement techniques which will be described here.

TABLE 1.1: SEMICONDUCTOR MATERIAL PROPERTIES
[EV11][Kno00][Sze04][Hay51][Kem80][Bil67][Owe02]

| | CdZnTe | Si | Ge |
|----------------------|--------------------------------|--------------------------|--------------------------|
| Atomic Number | 49.1 | 14 | 32 |
| Bandgap | 1.572 eV | 1.12 eV | 0.67 eV |
| Pair Energy | 4.64 eV | 3.62 eV | 2.95 eV |
| Density | 5.78 g/cm ³ | 2.33 g/cm ³ | 5.33 g/cm ³ |
| Mobility (electrons) | 1000 – 800 cm ² /Vs | 1200 cm ² /Vs | 3600 cm ² /Vs |
| Mobility (holes) | 80 – 30 cm ² /Vs | 250 cm ² /Vs | 1700 cm ² /Vs |
| Lifetime (electrons) | 1 – 5 μ s | 100 – 1000 μ s | ~ 100 μ s |
| Lifetime (holes) | 1 – 0.1 μ s | 100 – 1000 μ s | ~ 100 μ s |
| Fano factor | 0.1 | 0.12 | 0.13 |

Cadmium Zinc Telluride Detectors

Cadmium zinc telluride is a semiconductor with a zinblende structure with many almost ideal properties for applications like γ -astronomy, homeland security, nuclear safety and medical imaging. It has a high density, a high atomic number and a reasonable bandgap which on the one hand is small enough to give a pair energy substantially lower than scintillators or gas detectors and on the other hand is large enough to allow operation at room temperature. Fabrication is challenging because of the tendency of the melt for tellurium inclusions, the low thermal conductivity and other intrinsic problems. Nonetheless, the demand on the market for room temperature semiconductor detectors has incited the industry to refine the production techniques so that spectroscopy grade crystals at

reasonable sizes and prizes are available. They are normally grown by high pressure Bridgman, low pressure Bridgman, vertical Bridgman and traveling heater methods. Especially the demand in the homeland security and nuclear safeguard sectors for robust field spectrometers for isotope identification has driven the development so that crystals of several cubic centimeters are readily available. However, larger crystals are still rare and thereby expensive and each crystal may have different properties so that the numbers in table 1.1 are only for orientation.

In addition to the restricted availability of big crystals, a challenge when measuring with CdZnTe is the very poor $\mu\tau$ product of holes. As can be seen from table 1.1, there is a difference of three orders of magnitude in comparison to silicon or germanium. For electrons, equation (1.19) can be fulfilled in most cases, but for holes, it cannot. Moreover, holes that cannot move at all and do not contribute to the induced charge is often a valid assumption. Reevaluating (1.18) under this condition gives

$$Q_i = -eN_{\text{ch}}(1-d/L). \quad (1.21)$$

The pulse amplitude will be between 0 and a maximum value proportional to the deposited energy and the depth.

To circumvent the depth dependence and to restore a sole proportionality to N_{ch} , one has to tune the weighting potential by altering the electrode layout. The degrees of freedom in this respect are however limited since one has to retain a homogeneous sensitivity and for many applications a planar device. This can be achieved if Φ is flat in nearly the whole detector depth and rises steeply very shortly before the sensing anode. In this case, the electrons do not induce any signal as they travel the bulk. The signal just rises when they are very close to the anode.

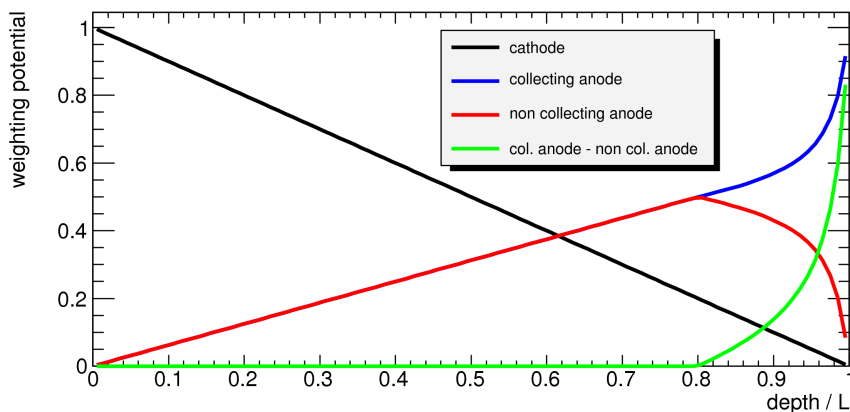


Figure 1.8: Weighting potential in a coplanar grid detector along a line perpendicular to the electrodes and ending on one of the collecting strips. The cathode potential is just the same as in a simple planar detector. The collecting and non-collecting potential are similar until shortly before the anode surface. The difference of the two has just the desired form to generate a depth-independent signal.

The most elegant way to achieve this has been proposed by Paul Luke [Luk94]. It is similar to the concept of the Frisch grid for gas detectors and is most commonly referred to as coplanar grid electrode design. In this design, the anode is laid out as two interfingering grids of thin strips. One is referred to as the collecting anode, the other as the non-collecting

anode. The weighting potential along a line through the detector that ends on a collecting anode strip for all electrodes is shown in figure 1.8. The anode grids have practically the same potential across the majority of the detector depth. Thus, the difference between the two is flat and only rises steeply in a region whose depth is in the order of magnitude of the strip pitch. This is just the desired form of the weighting potential described above. Since the charge induction and the pulse formation are all linear processes, a depth independent signal can be obtained by subtracting the non-collecting anode signal from the collecting anode signal.

The coplanar grid technology is elegant and efficient, but it introduces an extra readout channel including electronic noise. For some applications, it is advantageous to pursue a simpler way of unipolar charge sensing. In a helical detector, Φ drops proportional to $1/r$. The potential is not entirely flat in most of the detector volume, but sufficient to get a signal with a weak dependence on depth. It has been found that anodes made of small pixels achieve the same effect. The field can be shaped similarly for a planar electrode, when the collecting anode is closely surrounded by the non-collecting anode. In the concept of the weighting potential, the effect of the non-collecting anode can be understood as follows: the potential of the anode is calculated by setting the boundary conditions on the anode to 1 and to 0 on the non-collecting anode. Since the two electrodes are very close to each other, the field lines are pushed sharply to the collecting anode which makes the potential rise quickly close to the anode which is just the wanted behavior. This technique has been first applied for semiconductor detectors by [Pat96] and [But97] to compensate for bad hole mobility.

Although Φ does not depend on the applied voltage, the non-collecting anode – or the steering electrode – is biased on a voltage higher than the collecting strips, but substantially lower than the cathode. The non-collecting anode is therefore also named focusing electrode.

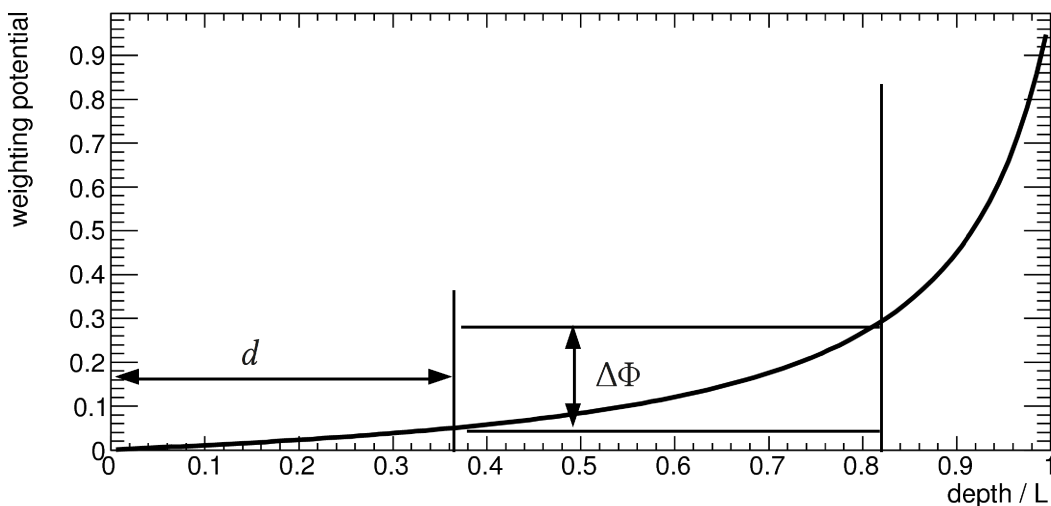


Figure 1.9: Schematic display of the weighting potential of the collecting anode in steering grid configuration. Electrons set free in a depth d experience a slight rise in the potential before reaching the near-grid region on the right. If $\Phi(d)$ is adjusted carefully, it can compensate for charge trapping.

When not using the coplanar grid, the potential is not entirely flat throughout the detector. This is illustrated in figure 1.9. As mentioned before, this introduces a weak depth

dependence of the anode signal. Electrons generated at a depth d experience a larger potential difference $\Delta\Phi$ before reaching the region close to the anode with rapid potential rise on the right of the graph. The signal from electrons generated closer to the cathode is therefore larger. This in principal unwanted behavior can be used to compensate for electron trapping [Amm97]. In a coplanar grid, only the electrons contribute to the pulse which arrive in the near-grid region. Their number decays exponentially. If Φ can be adjusted so that

$$\frac{\Delta\Phi(d)}{e \frac{L-d}{\mu_c \tau_c |\vec{E}|}} \approx \text{const.} \quad (1.22)$$

in the far grid region, electron trapping is intrinsically compensated. Φ can only be shaped yet via the electrode geometry. This approach is hence not very flexible because μ and τ are seldom known before fabrication.

If one has the ability to handle numerous readout channels, it has been shown that a pixelated anode with negligible space between the pixels is also insensitive to hole movement [Bar95]. The pixel pitch has to be small compared to the detector thickness, but still larger than the charge cloud dimensions. If a suitable readout chain in form of an application specific integrated circuit (ASIC) or by other means is available, this is the method of choice if spatially resolved measurement is required. A detector with a segmented anode and a continuous cathode can give an accurate energy signal and the point of interaction in all three dimensions as explained in the following paragraph.

The weighting potential of the cathode is not touched by the grid structure on the anode side. Its induced charge is the same as in a simple planar detector. If the approximation of completely immobile holes (1.21) holds and the induced charge on the anode is $-eN_{\text{eh}}$, the ratio of the cathode and anode signal can be used for depth of interaction information [He97]:

$$\frac{Q_{\text{cathode}}}{Q_{\text{anode}}} = 1-d. \quad (1.23)$$

With the progress in fabrication technology and the mentioned methods to circumvent and even exploit the very different transport properties of electrons and holes, CdZnTe is a very convenient material for many applications. It has been deployed in homeland security projects [Wah10], the search for the rare neutrinoless double beta decay of ^{116}Cd in the experiment COBRA [Schw11], in medical imaging [Cui11] and many other applications.

1.3.2 Scintillation Detectors

One of the oldest modalities to perform calorimetric measurements of photon radiation is to use scintillators. These are crystals that transform the energy deposited by ionizing particles into light in the visible or ultraviolet range. The amount of light is proportional to the deposited energy. These materials are not common in nature since it is required that they emit light at a certain wavelength while being transparent for just this light.

There are several ways for scintillation to emerge involving the electronic band structure of the crystal. One very common mechanism is the cerium induced scintillation where an

appropriate host crystal is doped with Ce^{3+} . The cerium ions provide shallow defects close to the conduction band and the valence band. As electron-hole pairs are generated, holes get eventually trapped in the $4f$ state and electrons in the $5d$ state of the same cerium ion. The orbital overlap between these two leads to annihilation and the emission of light with a wavelength of approximately 420 nm. The mean lifetime of this state is around 30 ns and largely independent** of the host crystal since it is inversely proportional to the probability of the transition between the $4f$ and $5d$ orbitals. The decay time of the excited states is a characteristic number of the scintillator. For good timing, one wants the decay time to be short to have a sharply rising pulse.

The scintillation mechanism of Ce^{3+} is very efficient. Ce doped scintillators are therefore considered as being “bright”. This quantity is expressed in the proportionality constant between the deposited energy and the average amount of scintillation photons – the light yield Y . The properties of scintillators with different scintillation mechanism are shown in table 1.2. Besides the listed attributes, the price and availability are important. Furthermore, crystals may be hygroscopic like NaI and LaBr_3 , or may have an intrinsic radioactivity like Lu_2SiO_5 due to the natural abundance of ^{176}Lu .

TABLE 1.2: SOME COMMONLY USED SCINTILLATORS [HAA08][LAV83]. WHILE THE ATOMIC NUMBER AND DENSITY ARE DETERMINED BY THE HOST CRYSTAL, THE SCINTILLATION PROPERTIES ARE MOSTLY GIVEN BY THE SCINTILLATION CENTERS Tl AND Ce. BaF_2 IS AN INTRINSIC SCINTILLATOR WHICH DOES NOT REQUIRE DOPING.

| | Eff. atomic number | Density [g/cm ³] | Light yield [ph./MeV] | Decay time [ns] |
|--------------------------------------|--------------------|------------------------------|-----------------------|-----------------|
| NaI(Tl) | 50 | 3.7 | 44 000 | 230 |
| BaF_2 | 52 | 4.9 | 2000 | 0.6 |
| $\text{Lu}_2\text{SiO}_5(\text{Ce})$ | 64 | 7.4 | 27 000 | 40 |
| $\text{LaBr}_3(\text{Ce})$ | 45 | 5.3 | 61 000 | 20 |

Once the light is emitted it has to be transported to a light sensor and being read out. Scintillation crystals are usually wrapped with reflective material on all sides but one which is attached to the light sensor. Only a fraction of the emitted light ϵ_{col} reaches the detector. This depends on the crystal geometry, its surface properties and the wrapping. The light sensor can be a photomultiplier tube (PMT), a photodiode, an avalanche photodiode (APD) or a silicon photomultiplier (SiPM).

PMT are the oldest devices for low level light sensing that are still commonly used. The entrance surface of the light is made of a material with a low work function. The photons undergo the photoelectric effect and emit electrons. The number of electrons is

$$N_e = N_{\text{ph}} \epsilon_{\text{qe}}. \quad (1.24)$$

(N_{ph} : number of photons, ϵ_{qe} : quantum efficiency of the photo cathode)

***) The total decay time of the scintillator includes the transport of the charge carriers to the scintillation centers. In this sense, the host crystal contributes to the decay time, but there is a lower threshold given by the orbital overlap.

When the electrons are emitted is the point in the signal chain with the fewest number of charge carriers. Hence, this is when the resolution is determined. Applying (1.12) with $F = 1$ gives

$$R \geq 2.35 / \sqrt{\varepsilon_{qe} \varepsilon_{col} Y E_{dep}}, \quad (1.25)$$

where Y is the light yield. ε_{qe} is around 0.3 depending on the cathode material. ε_{col} is usually around 0.5. This loss of signal additional to the higher pair energy compared to semiconductors give scintillators in most cases a worse energy resolution than semiconductors.

The primary electrons are accelerated through an electric field within the PMT towards a metal surface (dynode) where they set free other electrons. This step is repeated in several acceleration stages until the electron shower reaches the final anode where the output signal is measured. At the final stage, the number of electrons is 10^6 to 10^7 times that of the initially generated electrons. The total bias of the PMT is in the range of 1 keV.

Depending on the shape of the dynodes, the electrons in the shower can take slightly different paths which leads to transit time spread. The pulse of a PMT rises very quickly and makes it the first choice for timing applications. The intrinsic rise time is the order of 1 ns.

The high gain and the speed of a PMT are its main advantages. However, they cannot be built arbitrarily small since the dynode array requires space. In applications where segmented readout is required, a one-to-one coupling of crystal to PMT is often not feasible. An intermediate solution is to couple a large crystal or a crystal matrix to four PMT. The point of light emission can then be recovered by calculating the center of gravity of the four PMT signals. This is referred to as Anger principle [Ang58].

Recently, PMT are more and more replaced by silicon detector devices. Conventional *pin*-diodes (*positive intrinsic negative* diodes) are not suitable for scintillation light sensing since the number of photons is too low to produce a convenient signal on such devices. Diodes with internal gain have therefore been developed. In APD, an electron shower analogue to the mechanism in a proportional gas counter is generated. The overall gain is here proportional to the applied voltage. It is usually in the range of 100 V. These devices can be manufactured much smaller and are insensitive to magnetic fields unlike PMT. Because of that, entirely new fields of application are open to scintillation detectors in combination with APD like combined PET/magnetic resonance tomography imaging. These devices also provide a much higher quantum efficiency ε_{qe} of up to 0.8.

APD have a substantially lower gain than PMT. It is usually around 100 to 1000. Because it depends on the voltage, the bias has to be carefully stabilized. Furthermore, they are sensitive to temperature variation.

A gain comparable to that of PMT can be obtained when operating the diodes in Geiger mode analogous to the working principle of the Geiger counter. These diodes are called Geiger diodes or silicon photomultipliers (SiPM). The avalanche is so strong that the resulting charge is independent of the amount of primary charge. The proportionality to the primary charge is restored by segmenting the detector in many micropixels or SPAD (single-photon avalanche diode). In an analogue device, the output of the SPAD are connected in series to a common output which is then proportional to the number of fired cells. The advantage is the high gain of these devices, but due to the pixel structure, only a part of the total area is sensitive. Additionally, these devices have a certain dark count rate because the avalanche is easily triggered by very few electrons. Radiation damage might further increase the dark count rate. When designing a system with SiPM, one also has to have in

mind the limited dynamic range which ranges from one fired pixel to the total number of available pixels.

Nevertheless, SiPM offer signals that rise nearly as quick as that of PMT and will most probably replace the latter on the long run.

A very interesting development on this path is the availability of fully digital SiPM [Deg10]. In these devices, the pixels are not connected in series to a common output, but are read out digitally one by one. This allows masking noisy pixels or areas and removes the need of a subsequent signal shaping chain.

1.4 Compton Imaging

In imaging applications the origin of photons is of interest. When the dominating interaction modality of the photons is the photoeffect, the photon field can be collimated by passive materials. Through the shape of these collimators, an image of the source density can be reconstructed. This is exploited in pinhole cameras and in coded aperture imaging. A collimator, often made of lead or other material with a high atomic number shapes the field for later detection. As photons of higher energy are of interest, the absorption of the high Z material gets inefficient (c.f. figure 1.4) and incoherent scattering becomes the dominant interaction mode.

One can restrict the possible origin of a photon if it undergoes incoherent scattering in \vec{r}_1 with energy deposit L_1 and is absorbed in \vec{r}_2 with energy deposit L_2 . Applying the Compton kinematics of (1.2), the scattering angle φ and the incident energy E_0 can be calculated:

$$\cos\varphi = 1 - mc^2 \left(\frac{1}{E_0 - L_1} - \frac{1}{E_0} \right). \quad (1.26)$$

$$E_0 = L_1 + L_2$$

Together with the two interaction sites, the origin of the photon can be restricted to a cone whose axis goes through \vec{r}_1 and \vec{r}_2 with the opening angle φ and the apex in \vec{r}_1 . Figure 1.10 illustrates the situation for a single cone. Several photons from the same source will generate several cones that intersect at the source position. Furthermore, the cone data allows to apply image reconstruction methods. This will be discussed briefly further down.

A detector system is required which is able to measure spatially resolved two subsequent energy depositions. They can take place in the very same detector volume, but it is often advantageous to have two separated stages in order to optimize one for scattering and the other for absorption of scattered photons.

Photons of several MeV energy might however even after a scattering event carry so much energy that an absorption is still unlikely. An impractically thick absorber layer may be needed for an efficient device. A more advanced Compton imaging technique has been proposed for astrophysical purpose. It has the advantage that the camera needs less material but is still efficient for several MeV photons [Kur00]. Here, two subsequent scattering events are required and a third interaction of any kind as long as enough energy is deposited to trigger the detection. The desired event chain is illustrated in figure 1.11.

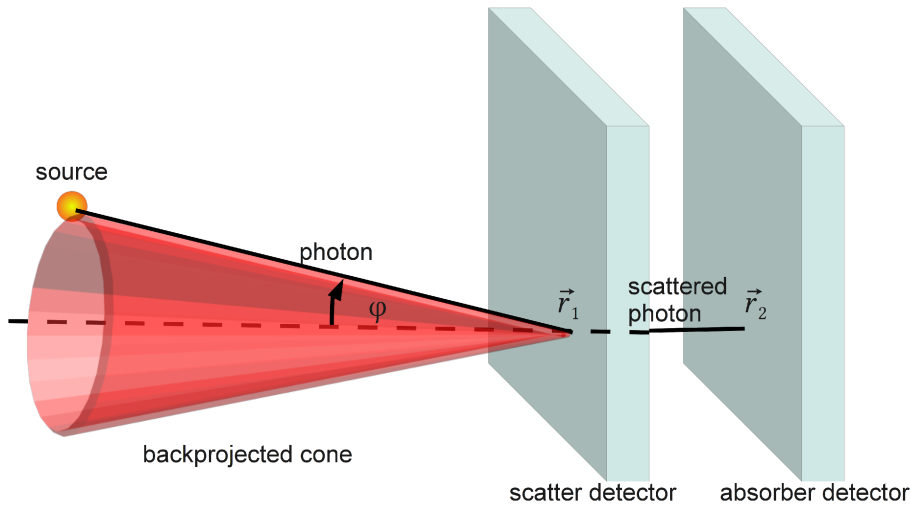


Figure 1.10: Principle of Compton imaging. A photon is scattered in a first detector layer in \vec{r}_1 and absorbed in a second one in \vec{r}_2 . The kinematics restrict the possible origin to the surface of a cone whose geometry is given through the interaction sites and the deposited energies. The cone therefore intersects with the actual source position.

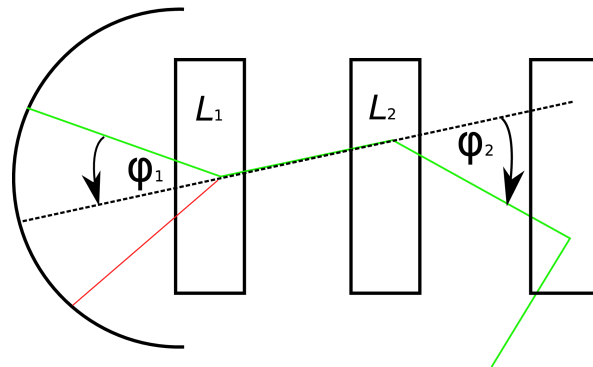


Figure 1.11: Event chain in multiple Compton scattering. Two Compton scatter events are followed by a third interaction which does not have to be an absorption event.

The first scattering angle (the opening angle of the cone) and the initial photon energy can still be calculated. The second equation in (1.26) is replaced with the kinematics equation of the second scatter event. The equations become

$$\begin{aligned} \cos \phi_1 &= 1 - m c^2 \left(\frac{1}{E_0 - L_1} - \frac{1}{E_0} \right) \\ \cos \phi_2 &= 1 - m c^2 \left(\frac{1}{E_0 - L_1 - L_2} - \frac{1}{E_0 - L_1} \right). \end{aligned} \quad (1.27)$$

This is a system of two equations with the two unknowns E_0 and ϕ . L_1 , L_2 and ϕ_2 are measured quantities. Solving for E_0 gives

$$E_0(L_1, L_2, \varphi_2) = L_1 + \frac{L_2}{2} + \frac{1}{2} \sqrt{L_2^2 + \frac{4mc^2 L_2}{1 - \cos \varphi_2}}. \quad (1.28)$$

With this, the opening angle of the cone becomes

$$\cos \varphi = 1 - mc^2 \left(\frac{1}{E_0 - L_1} - \frac{1}{E_0} \right) \quad (1.29)$$

which is just the same as in the single scatter case.

It should be mentioned, that if the photon is scattered multiple times in the detector and it is assured that it loses all its energy, the energy depositions can just be summed up and attributed to the second interaction site. Thereby, the simple case of single scattering with a subsequent absorption is restored and the respective equations are valid for this case, too.

In the course of this work, the event chain where the kinematics of a second scattering event are exploited might be referred to as *scatter-scatter* technique or *3-Compton* technique. The simpler case where the total energy is accessible will be referred to as *scatter-absorber* or *2-Compton* technique.

Since the measurement of a single Compton event comprises several measurements in space, time and energy (\vec{r} , t , E), numerous uncertainties play a role. It will be discussed in detail in chapter 2 how these errors influence the quality of the acquired data. Here, the errors should only be mentioned:

- **Geometry errors:** The segmentation of the detector makes the geometry uncertainty in the two lateral dimensions. The pixel depth or depth-of-interaction capability give information on the error in the third direction.
- **Energy:** The energy resolution of the scatter layer and absorber layer contribute differently to the total error.
- **Electronic motion:** As mentioned in 1.1.2, the electronic motion puts an intrinsic limitation on the accuracy of Compton imaging.

1.4.1 Image Formation

The image formation algorithm that has been used with the data of this project has been developed and implemented by Sebastian Schöne. It is mentioned here for the sake of completeness and to emphasize the various interconnection points of detector physics to image reconstruction.

A central point in image reconstruction is the mapping between the actual emission scene λ and the measured data \mathbf{d} . The mapping is supplied by the function A which is characteristic for the measurement device:

$$\mathbf{d} = A(\lambda). \quad (1.30)$$

The task in image reconstruction is to find an image λ' such that

$$\begin{aligned} \lambda' &= A^{-1}(\mathbf{d}). \\ \lambda' &\rightarrow \lambda \end{aligned} \quad (1.31)$$

It is common to express the function A in matrix form $A = (a_{ij})$. The measured data in the event space element i , d_i , is generated by the values in the image space in each voxel j , λ_j , via:

$$d_i = \sum_j a_{ij} \lambda_j. \quad (1.32)$$

The event space in Compton imaging is a 7 dimensional space with the coordinates $(E_0, \cos\phi, \vec{r}_{\text{apex}}, \vec{d}_{\text{axis}})$ (initial energy, scattering angle, apex position, direction of the cone axis). Each measured event can be represented as a point in this space.

The system matrix (a_{ij}) supplies the transition of an emission in a certain point in space into the event space. It therefore includes all physics, geometry and data processing. Details about the modeling of (a_{ij}) can be found in [Scho10].

The image reconstruction algorithm for solving (1.31) is either the simple backprojection algorithm which is just the backprojection of all measured cones into image space, or the gold standard *maximum likelihood expectation maximization* (ML-EM) algorithm based on [She82]. The latter is an iterative algorithm which updates an image λ' in each step. ML-EM allows to account for statistical fluctuation in the data.

The measured cones are affected by measurement uncertainties and the a priori unknown electron momentum. The density function of the cone in image space is not a δ -function but a distribution according to the probability of the measured event originating from a certain point in space.

The distribution is not necessarily Gaussian. Especially the electron motion adds a shape that deviates considerably from a standard Gaussian form. This will be discussed in detail in section 2. The weighting factors by which different sources of error contribute to the final cone profile depend on energy and scattering angle. Consequently, each cone has an individual density profile.

At the stage of selecting the cones to be used, it is possible to apply event filters that only select events with certain criteria such as a window on the total deposited energy or a certain interval on the scattering angle. These filters are crucial for the selection of good events out of measured data and to reduce random coincidences.

1.4.2 History and Application of Compton Cameras

The Compton camera technique which is a central part of this work is not a new technology but has a long track record in astronomy. It was first proposed in 1973 [Scho73] for a telescope for intermediate gamma energies which penetrate too well to be efficiently stopped in reasonable absorbers and which do not yet produce particle showers via alternating pair production and radiative energy loss. Compton telescopes need to be satellite mounted because photons with relevant energies do not reach deep into the atmosphere of the earth. The first successful instrument of this kind was the Imaging Compton Telescope (COMPTEL) aboard the Compton Gamma Ray Observatory satellite from 1991 to 2000. COMPTEL comprised a scatter layer of liquid scintillator and NaI absorber detectors [Scho84].

In 2002, the INTEGRAL (International Gamma-Ray Astrophysics Laboratory) satellite was launched with a coded aperture imaging instrument aboard. The instrument IBIS (Imager on-board the INTEGRAL satellite) consists of one layer of 128×128 CdTe detectors optimized for imaging in the energy range from 15 keV to 1 MeV. A second layer is made of 64×64 CsI scintillation crystals which are designed for imaging in the energy range from

190 keV to 10 MeV. Through the double layer layout, it is possible to use the IBIS instrument for Compton imaging as well [For07]. Due to the possibility to combine coded aperture imaging with the Compton mode, the IBIS instrument reaches an improved spatial resolution compared to COMPTEL.

An advanced instrument especially designed for Compton imaging will be the Nuclear Compton Telescope (NCT) which currently undertakes balloon born flights. NCT is a stacked detector system of 12 double sided germanium strip detectors [Bel09] and can therefore make use of multiple scattered photons. The MEGA collaboration (Medium Energy Gamma-ray Astronomy) has built prototype detectors based on a stack of double sided silicon strip detectors as scatter and tracking detector and pixelated CsI detectors to absorb scattered photons [Kan04].

The clear trend in the development of these astrophysical instruments is towards finer segmentation and stacked detectors to reach a good resolution and a reasonable efficiency at the same time. Semiconductor detectors are very well suited and replace the scintillation materials, which are only used in the absorption stage. This development puts high demands on the read out electronics and craves for integrated solutions.

The Compton camera was proposed for medical purpose about the same time as it was in astrophysics [Tod74]. It was suggested to replace the Anger camera used in single photon emission tomography (SPECT). The Anger camera features a pin-hole or multi-hole collimator in front of a position sensitive detector. Photons not hitting the holes are absorbed which results in a very low efficiency. However, with the Anger camera, there is a viable technical solution for SPECT imaging which is challenged by a novel concept. The simplicity and robustness of the Anger camera might be a reason why the Compton camera never made it into clinical practice, despite early promising results shown in the extensive work of Singh and Doria [Sin85]. Moving towards stacked, finely segmented detectors may give the best results in Compton imaging as shown by astrophysics, but due to the increase in electronic readout channels does not make this technology economically competitive to the battle proven Anger camera. However, recently a group from Japan has shown impressive SPECT results recorded with an instrument that was initially designed for astrophysical purpose [Kab10]. Their Compton camera features a gaseous time projection chamber (TPC) as scatter detector and LaBr_3 as absorber. The TPC allows to track the recoil electron and thereby restrict the Compton cones to an arc according to the momentum resolution of the system. While this instrument sacrifices some efficiency owed to the low density of the scattering stage, it certainly has its appeal through the relatively simple readout scheme compared to a stack of semiconductor detectors with millimeter segmentation in coincidence and the possibility of electron tracking.

1.5 Prompt γ -ray Imaging for In-vivo Dosimetry – Work of Other Groups

Driven by the growing ability of ion therapy units, there is recently enhanced scientific interest in Compton imaging for radiotherapy. Like explained in the motivation, a Compton camera is a possible modality of imaging the promptly emitted photons from irradiated tissue. The above mentioned electron tracking camera has demonstrated the successful application of a Compton camera for this purpose [Kab09]. However, the beam current had

1.5 PROMPT γ -RAY IMAGING FOR IN-VIVO DOSIMETRY – WORK OF OTHER GROUPS

to be reduced while the irradiation time was prolonged. Further refinement of the camera design seems to be mandatory to achieve practical usefulness. This is where this work lines in with other efforts. There are simulation calculations that aim to optimize a semiconductor camera for in-vivo dosimetry [Pet00][Rob11][Roe11]. However, at the time of writing, the present work is the only one known to the author that scrutinizes CdZnTe as possible scatter material.

Another appealing approach for imaging prompt gamma rays is the use of a slit collimator [Pel11]. This technique is simpler in construction than a Compton camera, but yields only one-dimensional data on the beam location. However, for range verification this might be sufficient. Moreover, it provides the possibility for background subtraction since it does not rely on an event-wise data reconstruction. This is a major advantage in the struggle for actual feasibility and will be discussed in the conclusive part of this work.

2 Design Study

Prior to the construction of a Compton camera, calculations have been conducted concerning the expected performance of the device. The aim is not so much to gather entirely realistic numbers which are meant to be verified in experiments. This prevents already the lack of reliable emission data as discussed in section 2.1.1. It is rather the objective to explore if the Compton camera technology with available materials – and especially with CdZnTe – is a dead end for in-vivo dosimetry or worth pursuing.

The most significant results from this chapter have been published in a scientific paper [Kor11].

2.1 Introduction

Efficiency and resolution are the two crucial properties of a Compton camera that decide over the relevance of such a device for clinical practice. While the efficiency limits the number of events that can be used for image reconstruction, the angular resolution determines the quality of these events. Both numbers highly depend on the detection properties and the geometry. To answer the question if recent detector materials are at all able to allow Compton imaging with a reasonable quality – putting aside practical limitations that arise from the clinical application case for the moment – simulations have been carried out to estimate the efficiency as it is limited by the geometry and the material itself. Furthermore, an angular resolution measure (ARM) has been calculated to assess the data quality. The contributions from different factors that limit the ARM have also been calculated.

The Compton camera has its origin in the astrophysical field. There is therefore extensive activity similar to the calculations done in this chapter. Especially the comprehensive work of Andreas Zoglauer [Zog03][Zog06] has to be mentioned. The most significant differences however to the application pursued in this study are:

- (1) Astrophysical objects are at an infinite range compared to the scale of the detector.
- (2) The photon flux is very low.

- (3) The room temperature semiconductor CdZnTe has often not been considered as scattering detector.

Especially the last point justifies repeated calculations since CdZnTe is an appealing material for a clinical system since cooling is not required. A major motivation of the simulation work is to throw light on whether the large Doppler broadening in CdZnTe prevents it from being a feasible scatter material.

2.1.1 Emission Spectra – Available Data

The resulting ARM and efficiency depend explicitly on the γ -ray-spectrum which is needed as input data in subsequent simulations and calculations. In order to produce sustainable results, the input spectral data should not be questionable and be valid for any relevant conditions. Unfortunately, the spectral composition of the prompt photon spectrum depends on the type and geometry of the irradiation target. Furthermore, in section 1.2, the lack of experimental data for biologically relevant materials was mentioned and the problematic of simulated emission spectra. The strategy for the following calculations is therefore to keep the results energy depended, i.e. calculate ARM and efficiency for several energies in the range of a couple of MeV and to evaluate in a later step if the so found figures might suffice for imaging of the the most significant discrete γ -emissions and the statistical γ -rays which are most abundant.

2.2 Materials and Methods

The detector materials HPGe, CdZnTe and silicon have been studied. The resolution affecting factors and the expected efficiency have been treated separately. The calculation methods are presented here. Both the simpler, but presumably less efficient *scatter-absorber* technique and the more advanced *scatter-scatter* technique have been covered.

The computations were done using the software library *libCompton* which builds upon the object-oriented framework Root [Bru97]. The code *libCompton* has been developed within this study and provides classes for Monte Carlo calculations, data analysis and display. In the text, references to class names relevant for the current computation may occur.

2.2.1 Angular Resolution

Factors affecting the angular resolution include the energy resolution of any measurement, the spatial resolution and the Doppler broadening, i.e. the electronic motion which shifts the energy of the incoherently scattered photon. This causes a deviation from the ideal Compton kinematics.

Energy Resolution

The energy resolution of the detectors influence the value of the calculated cone opening angle only; the orientation of the axis remains untouched as it is entirely determined by the

localization of the first two events in the detector stack. To estimate the deviation from the true scattering angle due to blurred energy readings, a model for the resolution R (1.13) for different energy depositions L for the three detector materials is required. This can however vary greatly depending on the detector material and on the readout scheme so that a generalization may not be allowed. Either may a single, simple equation describe the data well over all relevant energies. Nevertheless, absolute accuracy is not required for these calculation. Resolution models should however reflect the differences between the detector materials and should mirror the behavior of a typical device in the range of 100 keV up to a couple of MeV. The following numbers have been used:

$$\begin{aligned} R_{\text{HPGe}} &= 2 \text{ keV}/L \\ R_{\text{CdZnTe}} &= (6 \text{ keV} + 0.15 \text{ keV} \sqrt{L/\text{keV}})/L \\ R_{\text{Si}} &= 2.5 \text{ keV}/L \end{aligned} \quad (2.1)$$

The HPGe and silicon model are motivated from results in [Vet07]. The model for CdZnTe is based on the numbers presented in [Zha05].

The relevant equations in terms of the energy depositions in the scatter and absorption site L_1 and L_2 are

$$\cos \varphi = 1 - mc^2 \left(\frac{1}{L_2} - \frac{1}{L_1 + L_2} \right) \quad (2.2)$$

in the *scatter-absorber* configuration and

$$\begin{aligned} \cos \varphi &= 1 - mc^2 \left(\frac{1}{E_0(L_1, L_2, \varphi_2) - L_1} - \frac{1}{E_0(L_1, L_2, \varphi_2)} \right) \\ E_0(L_1, L_2, \varphi_2) &= L_1 + \frac{L_2}{2} + \frac{1}{2} \sqrt{L_2^2 + \frac{4mc^2 L_2}{1 - \cos \varphi_2}} \end{aligned} \quad (2.3)$$

in *scatter-scatter* mode. To (2.2) and (2.3) standard error propagation in L_1 and L_2 has been applied. Neglecting covariance terms, (2.2) gives

$$\begin{aligned} (d\varphi)^2 &= T_1^2 \left(\frac{dL_1}{L_1} \right)^2 + T_2^2 \left(\frac{dL_2}{L_2} \right)^2 \quad \text{with} \\ T_1 &= \frac{mc^2 L_1}{(L_1 + L_2)^2 \sin \varphi} \quad \text{and} \\ T_2 &= \frac{mc^2 L_2}{\sin \varphi} \left(\frac{1}{L_2} - \frac{1}{(L_1 + L_2)^2} \right). \end{aligned} \quad (2.4)$$

The same procedure for (2.3) results in the expressions

$$\begin{aligned}
 (d\varphi)^2 &= T_1^2 \left(\frac{dL_1}{L_1} \right)^2 + T_2^2 \left(\frac{dL_2}{L_2} \right)^2 + T_3^2 (d\varphi_2)^2 \quad \text{with} \\
 T_1 &= \frac{mc^2 L_1}{E_0^2 \sin \varphi} , \\
 T_2 &= \frac{mc^2 L_2}{\sin \varphi} \left(\frac{1}{(E_0 - L_1)^2} - \frac{1}{E_0^2} \right) \left(\frac{1}{2} + \frac{1}{4} (L_2^2 + X L_2)^{-1/2} (2L_2 + X) \right) , \\
 T_3 &= \frac{\sin \varphi_2 mc^2}{4 \sin \varphi} \left(\frac{1}{(E_0 - L_1)^2} - \frac{1}{E_0^2} \right) (L_2^2 + X L_2)^{-1/2} \left(\frac{X L_2}{1 - \cos \varphi_2} \right) , \\
 X &= 4 m c^2 / (1 - \cos \varphi_2) .
 \end{aligned} \tag{2.5}$$

For later reference, the derivative with respect to φ_2 has also been calculated here.

The influence of the first scatter detector (i.e. T_1) is similar in both modes since $E_0 = L_1 + L_2$ in 2-Compton mode. T_1 can be further simplified. Solving (2.2) for L_1 and inserting it into (2.4) gives T_1 in dependence of φ and E_0 only:

$$T_1 = \frac{1}{\sin \varphi} \frac{1}{\frac{E_0}{mc^2} + \frac{1}{1 - \cos \varphi}} . \tag{2.6}$$

In 3-Compton mode, the same method yields

$$T_1 = \frac{mc^2}{E_0 \sin \varphi} (2\eta^2 - 2\eta - 1 + 1/\eta) , \quad \eta = 1 + E_0 / mc^2 (1 - \cos \varphi) . \tag{2.7}$$

It is obvious in this representation that the influence of the energy resolution of the first detector decreases with increasing incident energy when φ is kept fixed. However, φ will tend to be smaller as energy increases because forward scattering is preferred.

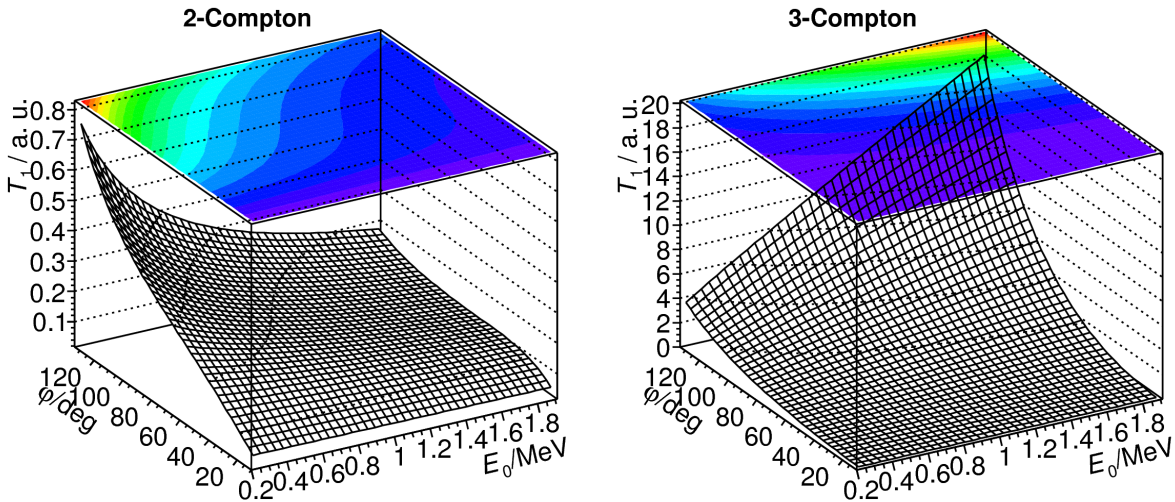


Figure 2.1: The influence of primary γ -ray energy E_0 and the scatter angle φ on the Compton camera angular resolution measure due to the first scatter detector denoted by the term T_1 .

T_1 is plotted over E_0 and φ in figure 2.1. In *scatter-absorber* mode, T_1 remains flat in the chosen parameter space. There is only an increase for low energies and large scattering angles. In *scatter-scatter* mode, there is a divergence in the unlikely regime of large angles and high energies.

The same analysis for the terms T_2 is not as straight forward since there is a dependence on the second scattering angle φ_2 in the scatter-scatter mode. This cannot easily be eliminated. However, evaluating T_2 for different φ_2 while E_0 and φ are kept fixed, it is revealed that there is only a slight variation with φ_2 . T_2 is plotted for $E_0 = 1$ MeV and $\varphi = 20$ degree in figure 2.2. To reduce the dimension of the parameter space for T_2 , φ_2 has been kept fixed at 110 degree as a worst case scenario.

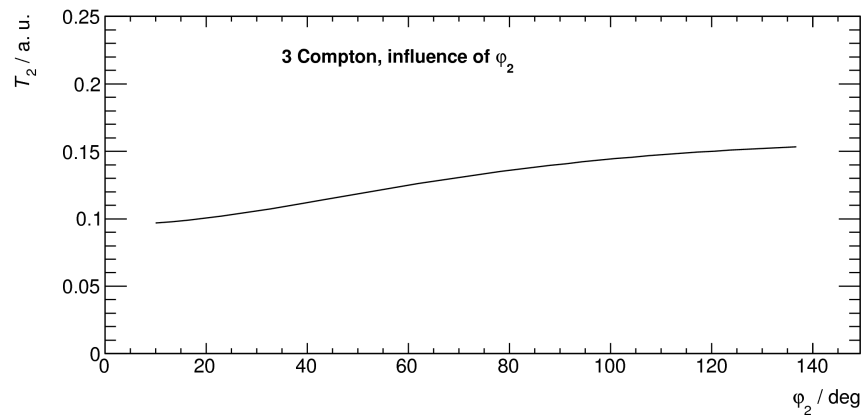


Figure 2.2: The variation of T_2 in scatter-scatter mode with φ_2 where E_0 is 1 MeV and φ is 20 degree.

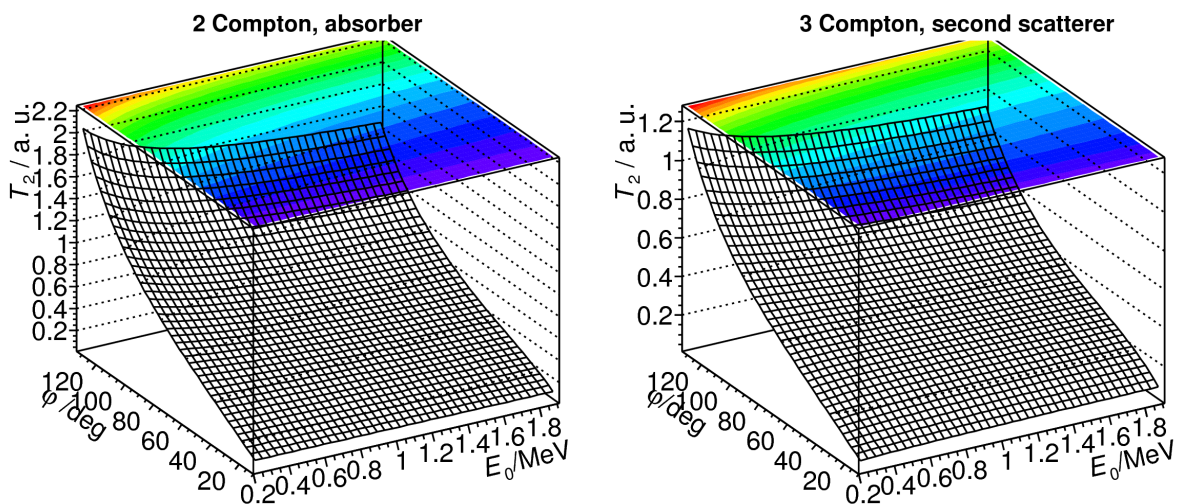


Figure 2.3: The influence of primary γ -ray energy E_0 and the scatter angle φ on the Compton camera angular resolution measure due to the second scatter detector denoted by the term T_2 .

Fixing the second scattering angle allows T_2 to be evaluated like T_1 . Figure 2.3 shows the influence of the second detector in dependence of the first scattering angle and the incident energy. There is a very similar behavior in 2- and 3-Compton mode, although the role of the

second detector is different in the two modes. In the simple case, it has to absorb the scattered photon while it may be scattered in the advanced mode. T_2 increases with increasing scatter angle, which are less likely with increasing energy.

The influence of the energy resolution can be calculated in dependence of E_0 and φ using the expressions for T_1 and T_2 and substituting dL/L with the resolution $R(L)$. What remains to be treated is the influence of the Doppler broadening and the spatial resolution.

Doppler Broadening

The term ‘‘Doppler broadening’’ in this context means that a photon is scattered off a moving electron with a certain quantum mechanical momentum distribution into an energy state that deviates from the clearly defined energy given by the Compton kinematics. Binding effects are neglected in this view since the transferred energy is considered to be large against the atomic binding energy. This is referred to as *impulse approximation* (sic). To be applied to real cases, a relativistic treatment is needed. This was first delivered by Ribberfors [Rib75][Rib82].

Scattering off an electron at rest is described by the well known Compton kinematics. Re-stating equation (1.2) for the energy of the scattered photon gives

$$E_C = \frac{E_0}{1 + E_0/mc^2(1 - \cos\varphi)}. \quad (2.8)$$

If the projection of the electron momentum on the direction of the incident photon is non-zero, the kinematics equation complicates to

$$p_z = -mc \frac{E_0 - E_1 - E_0 E_1 (1 - \cos\varphi)/mc^2}{\sqrt{E_0^2 + E_1^2 - 2E_0 E_1 \cos\varphi}}. \quad (2.9)$$

(p_z : electron momentum projection on the direction z of the incident photon, E_1 : energy of the scattered photon)

(2.9) reduces to (2.8) if $p_z = 0$.

The differential, relativistic cross section for scattering a photon with energy E_0 about the angle φ off an electron in the atomic shell n into a state with the final energy E_1 is (in the representation of [Ces92]):

$$\left(\frac{d^2\sigma}{d\Omega dE_1} \right)_n = \frac{m r_0^2 E_1}{2E_0} \left(\frac{E_C}{E_0} + \frac{E_0}{E_C} - \sin^2\varphi \right) (E_0^2 + E_1^2 - 2E_0 E_1 \cos\varphi)^{1/2} \mathcal{J}_n(p_z). \quad (2.10)$$

In this work, this cross section is also referred as Ribberfors cross section. It is proportional to the so called Compton profile $\mathcal{J}_n(p_z)$ of shell n . It is calculated as

$$\begin{aligned} \mathcal{J}_n(p_z) &= \int \int d p_x d p_y \Psi_n(\mathbf{p}) \cdot \Psi_n^*(\mathbf{p}) \\ \mathcal{J}(p_z) &= \sum_n Z_n \mathcal{J}_n(p_z) \Theta(E_0 - E_1 - I_n) \end{aligned} \quad (2.11)$$

where Ψ is the atomic wavefunction. $\mathcal{J}(p_z)$ is the total atomic Compton profile. Z_n is the number of electrons in shell n and Θ is the step function. I_n is the ionization potential of shell n .

The Compton profiles for most elements are available as tables in the publication [Big75]. These tables have also been used in the calculations for this work. Figure 2.4 shows the

atomic Compton profiles for the elements hydrogen, silicon and germanium. The curve for the simplest atom hydrogen has a simple structure while the curves for the elements with higher atomic numbers have a more pronounced structure. There is a contribution at low momenta like in hydrogen from the loosely bound (and thereby slow) valence electrons while the core electrons contribute at higher momenta. Through the kink in the curve the contribution to \bar{j} from these two types of electrons can clearly be identified.

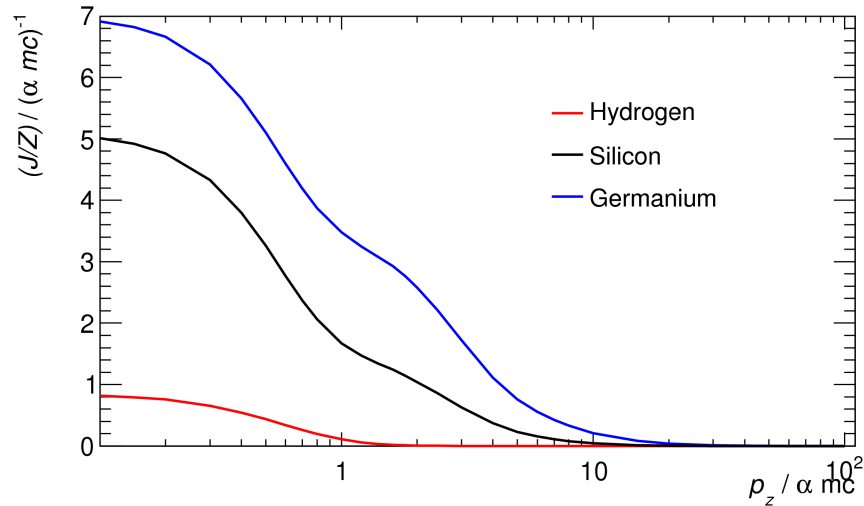


Figure 2.4: Atomic Compton profiles for the elements hydrogen, silicon and germanium.

It is interesting to plot the Ribberfors cross section together with the Klein-Nishina expression (1.3) (scaled with the atomic number) over the cosine of the scattering angle. This is done for CdZnTe at 200 keV incident energy in figure 2.5. The curves run close together for large scattering angles until the transferred energy becomes small at small scattering angles. Here, the electronic kinetic energy is not negligible and the Ribberfors expression deviates from the the Klein-Nishina curve. It is therefore expected to observe Doppler influence primarily at small scattering angles and low incident energy.

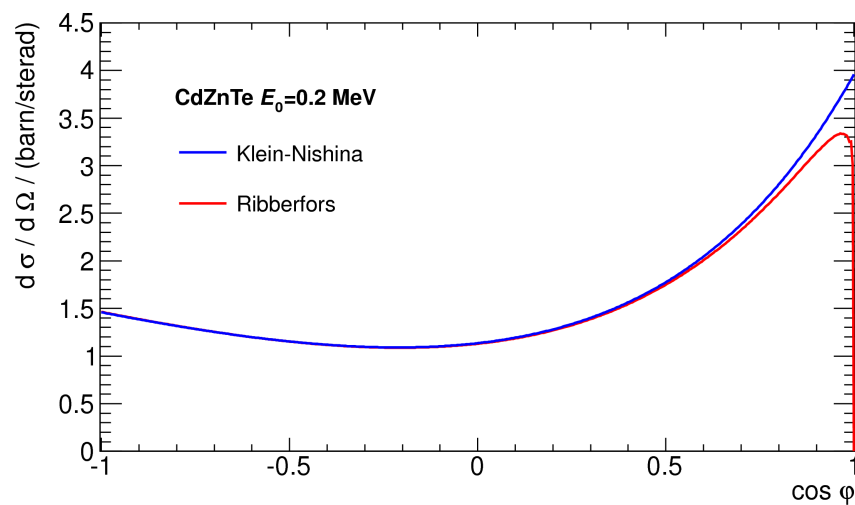


Figure 2.5: Ribberfors cross section and Klein-Nishina cross section for CdZnTe.

To translate the Ribberfors cross section into an angular distribution, the incident energy and the scattering angle have been kept fixed. Now the cross section becomes a function of the final energy E_1 . Assuming $L_2 = E_1$ and $L_1 = E_0 - E_1$ results in a reconstructed scattering angle $\varphi_{\text{rec}}(E_1)$ according to (2.2). Plotting the cross section as a function of the reconstructed angle instead of E_1 is the angular distribution which is looked for. An example for distributions of reconstructed scattering angles are plotted in figure 2.6 for incident energy 1 MeV and the scattering angle 30 degree for the three materials silicon, germanium and cadmium zinc telluride.

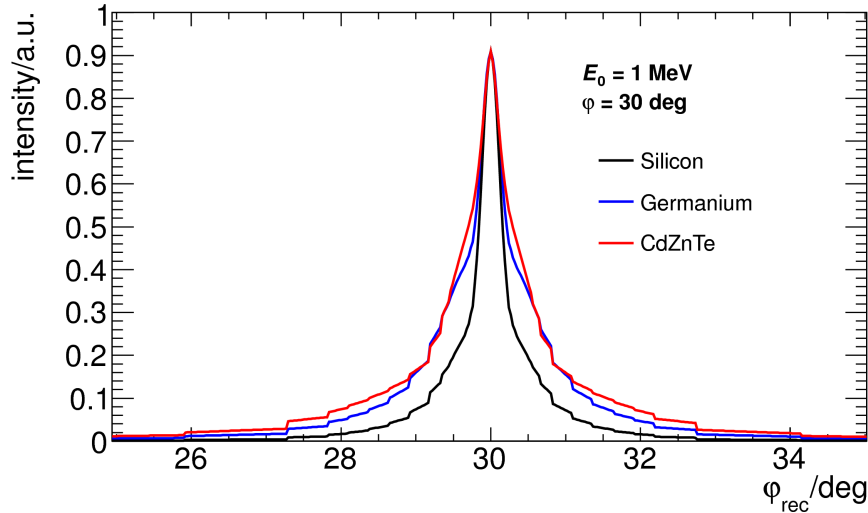


Figure 2.6: The distribution of the reconstructed scattering angle in 2-Compton mode due to Doppler broadening for three different scattering materials. The curves are normalized to the peak height.

In this representation the different orbitals can still be distinguished. There is a broad foot in each curve which is caused by the fast core electrons while the peak is due to the relatively slow valence electrons. It should be emphasized that in these calculations the atomic orbitals have been used. In the crystalline structure, the contribution of the valence electrons is different since they occupy de-localized states in the lattice. In this case, the Doppler broadening even becomes direction dependent and opens a possibility to measure the momentum density with high resolution detectors [Ree72]. These effects are however neglected here.

The distributions are centered around the true scattering angle and appear to be symmetric. However, a close look reveals that this is not the case. Since the total atom is at rest and has no momentum in the direction of the incident photon, this slight asymmetry is caused by the kinematic terms in front of $\mathcal{J}_n(p_z)$ in equation (2.10). Due to their nature of being asymmetric and having a narrow peak sitting on a broad foot makes the contribution from Doppler broadening hard to put into a single number to be compared to other factors. It was decided to use the full width at half maximum (FWHM). This approach however ignores parts of the broad foot which may contribute to image noise.

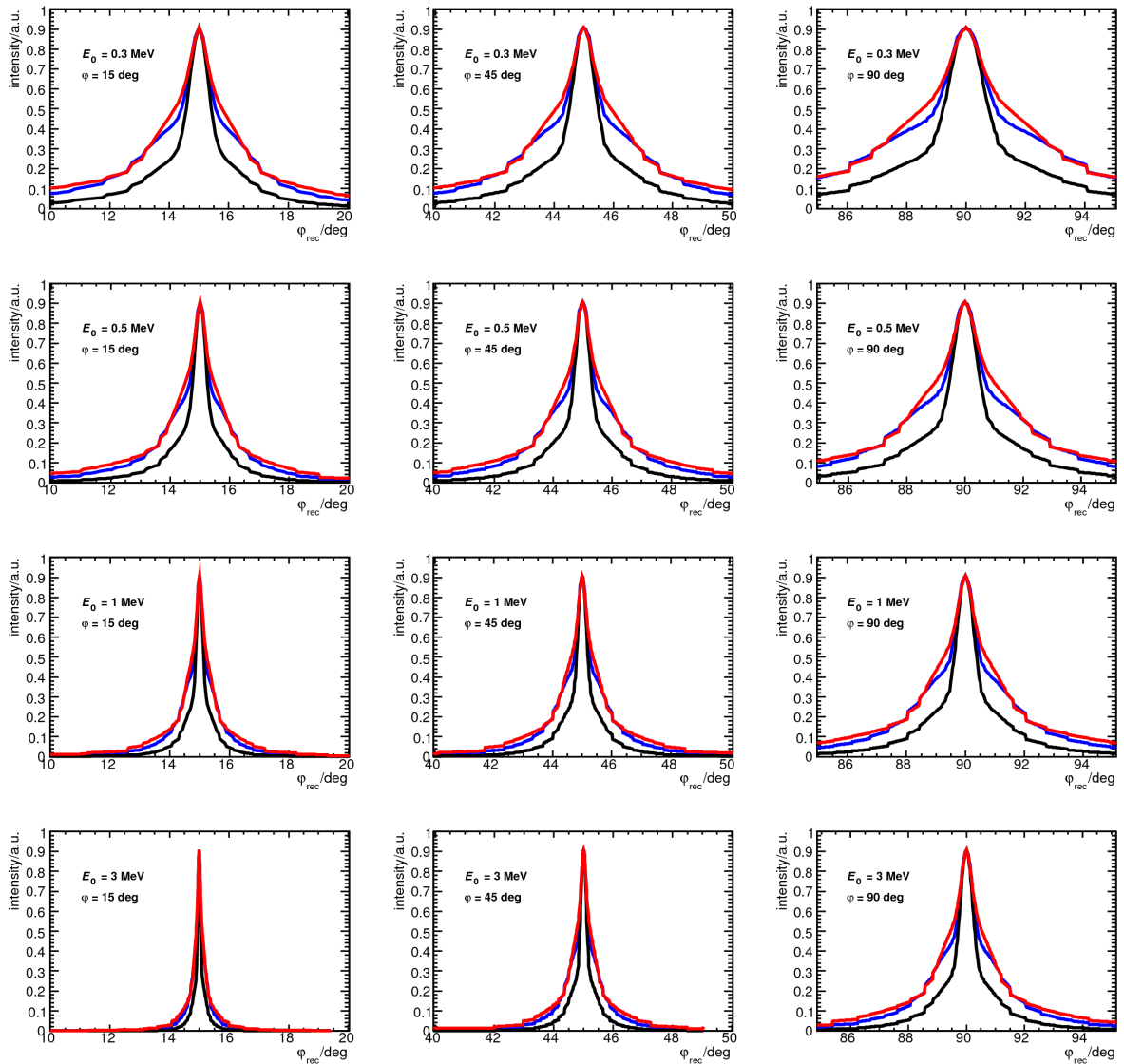


Figure 2.7: Profiles of the reconstructed scattering angle due to Doppler broadening in 2-Compton mode for different energies and scattering angles. Black: silicon, blue: germanium, red: cadmium zinc telluride.

In figure 2.7 the angular profiles at different energies and different scattering angles are plotted to explore the dependence of the Doppler broadening on these factors. It can be seen that lower energies and larger scattering angles produce broader distributions.

The discussion of Doppler broadening so far only covers the *scatter-absorber* technique. In scatter-scatter mode there is a second scattering event which involves moving electrons. To evaluate the total influence of these events on the reconstructed scattering angle, a simple Monte Carlo code was written. The calculation sequence is the following:

- (1) The Ribberfors cross section for E_0 and φ as a function of E_1 has been calculated.
- (2) E_1 has been drawn as a random number according to the cross section.

- (3) The Ribberfors cross section for the second event has been calculated with E_1 as incident energy and a fixed second scattering angle φ_2 as a function of the remaining energy E_2 .
- (4) The remaining energy E_2 has been drawn as a random number according to the cross section from (3).

Step (2) gives a deposited energy in the first scatterer $L_1 = E_0 - E_1$. Step (4) gives $L_2 = E_1 - E_2$. Together with the second scattering angle φ_2 which is fixed, a reconstructed scattering angle φ_{rec} could be calculated with (2.3). One run results in a single tuple $(E_0, \varphi, \varphi_2, \varphi_{\text{rec}})$. To get a distribution, the steps (2) to (4) have been repeated and the resulting φ_{rec} have been filled in a histogram. The cross section data is handled within the `CXSection` class of *libCompton* while the random number generation according to any distribution is efficiently managed by the class `CSpectrum`. The same task sharing was applied in the efficiency simulations which is described in section 2.2.2.

An example of resulting histograms is presented in figure 2.8. The form of the distribution requires the use of histograms with variable bin size. Near the peak the bins have to be smaller in order to reflect the steep slope. In the part outside the peak wider bins are advantageous in order to achieve good statistics despite the low probability of an event occurring in this region.

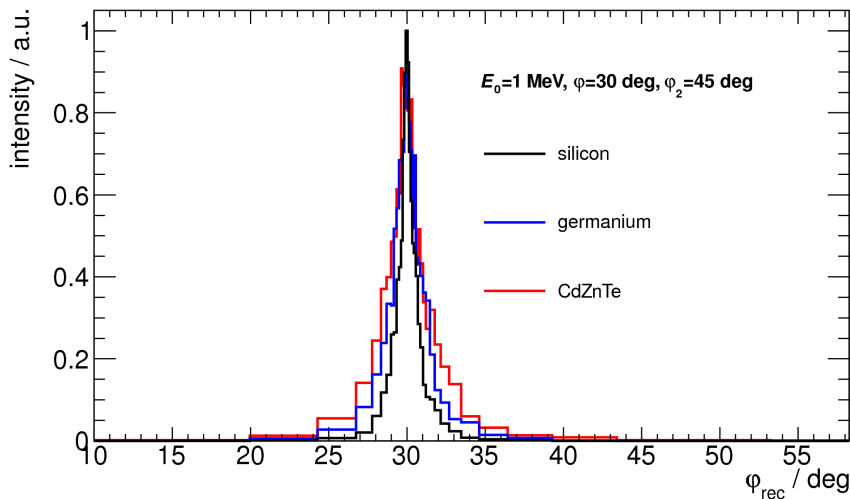


Figure 2.8: Distribution of the reconstructed first scattering angle in 3-Compton mode calculated for 2000 events in each distribution.

Silicon clearly stands out with a lower Doppler broadening similar to the situation in figure 2.6. CdZnTe performs slightly – but not dramatically – worse than HPGe. To quantify the width of the distribution, the FWHM has been used in the *scatter-scatter* case as well*.

*) The results published in [Kor11] were obtained by fitting a function to the distribution so that the FWHM was acquired as one of the fit parameters. The results in this section however were determined by a simple algorithm which runs over the distribution and compares the values to the peak value. Both methods yield approximately the same results. While the fit method is more robust to noisy distributions, the simpler approach requires less computation time.

A similar dependence on E_0 and φ is expected like in the *scatter-absorber* mode. Figure 2.9 is the analog to figure 2.7. In the data presented here, the second scattering angle was fixed to 45 degree. The general trend is clearly verified. High energies and small scattering angles result in narrow profiles. Large angles and low energies produce very broad profiles. Yet, this is not the regime where the scatter-scatter technique is expected to be efficient. Since a second scatter event is needed, there must be enough energy to let the scattered photon undergo scattering as well instead of being absorbed. Large angles in the first event are not only improbable, but can also result in a photon leaving the detector stack.

The same procedure as for the energy resolution of getting rid of the dependence on φ_2 was applied. The angle was simply fixed to 45 degree since it has a very limited influence on the total shape of the distributions.

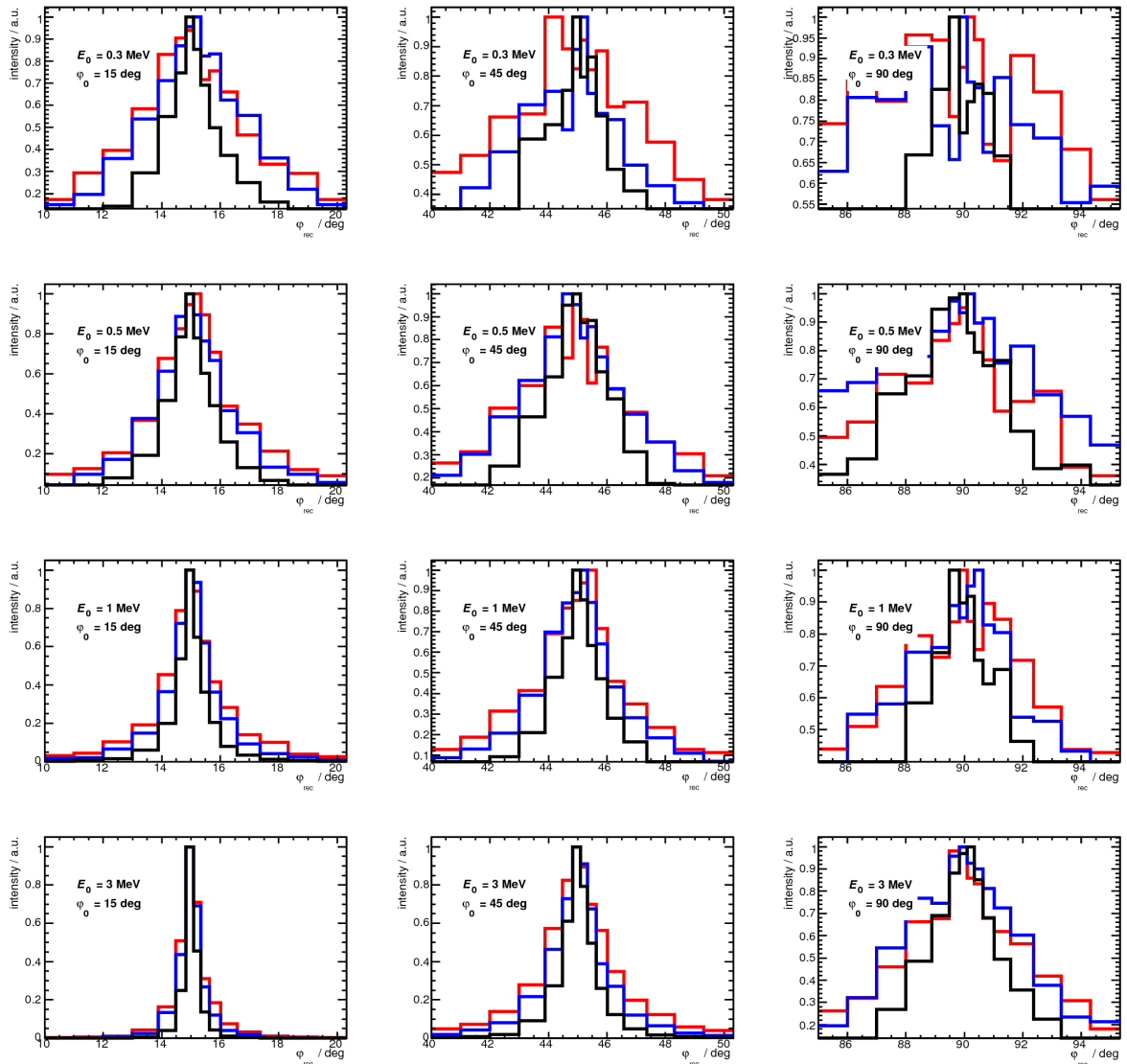


Figure 2.9: Profiles of the reconstructed scattering angle due to Doppler broadening in 3-Compton mode for different energies and scattering angles. The curves were calculated with 3000 events. Black: silicon, blue: germanium, red: cadmium zinc telluride.

Geometry

The spatial resolution, with which the interaction can be determined, influences in the *scatter-absorber* mode the reconstructed cone axis only. The localization of the first and second energy deposition both contribute to the overall uncertainty. Both parts can further be divided into a transversal and a longitudinal component. Longitudinal and transversal in this context means relative to the axis of the detector stack. The latter classification is arbitrary and based on the different spatial resolution expected from planar detectors. Lateral to the stack axis, it is the pixel size which determines the resolution. In the longitudinal direction, the depth-of-interaction capability is the crucial feature. If ϕ is the angle between the axis of the detector stack and the cone axis and x_1 and x_2 are the lateral distance of the two interaction sites to the axis and l the distance along this axis, ϕ can be calculated according to

$$\tan \phi = (x_1 - x_2) / l. \quad (2.12)$$

Applying error propagation to (2.12) results in

$$(\mathrm{d}\phi)^2 = \underbrace{\frac{\cos^4 \phi}{l^2} [(\mathrm{d}x_1)^2 + (\mathrm{d}x_2)^2]}_{\text{transversal}} + \underbrace{\left(\frac{\cos \phi \sin \phi}{l} \right)^2 (\mathrm{d}l)^2}_{\text{longitudinal}}. \quad (2.13)$$

In the chosen coordinate system along the stack axis, the total uncertainty comprises one term from the lateral detector resolution and one from the depth-of-interaction resolution. Both terms decrease with increasing detector distance l .

The parameter space for the angular resolution measure ARM has gained a new dimension with the cone axis angle ϕ . To eliminate this dimension and keep the parameter space to the dimensions E_0 and φ , the following estimation has been used:

$$(\mathrm{d}\phi)^2 \leq \frac{1}{l^2} [(\mathrm{d}x_1)^2 + (\mathrm{d}x_2)^2 + (\mathrm{d}l)^2]. \quad (2.14)$$

In *scatter-scatter* configuration, there is an additional geometrical contribution to the cone opening angle from the measurement of the second scattering angle φ_2 . It has also been calculated as the term T_3 in (2.5). T_3 nonetheless still depends on φ_2 . To explore this dependence, T_3 has been plotted over φ and φ_2 for different energies E_0 in figure 2.10.

For all energies, the term becomes very large if $\varphi_2 < \varphi$. This is however the unlikely case compared to the opposite situation since there is less energy available in the second event. Less energy results in larger scattering angles. Applying an event filter to the data that allows only events with $\varphi_2 > \varphi$ will therefore keep the major part of the data valid. This filter will beyond that assure that T_3 remains low. Under this condition, $\varphi_2 = \varphi$ gives an upper estimate for T_3 . Setting the second scattering angle equal to the first angle reduces the number of degrees of freedom and makes T_3 a function of E_0 and φ only.

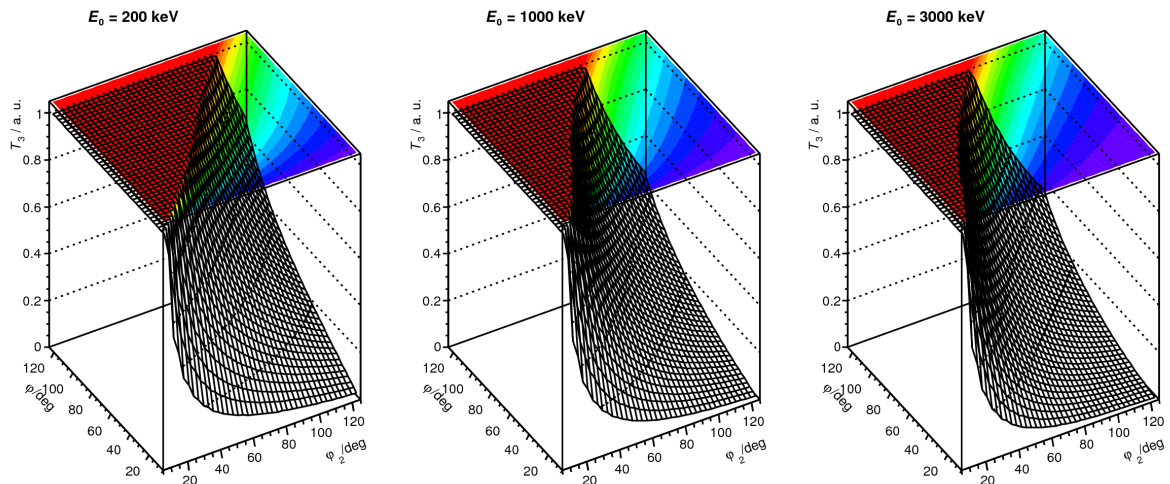


Figure 2.10: Geometrical contribution to the ARM in 3-Compton mode from the measurement of φ_2 at three different incident energies.

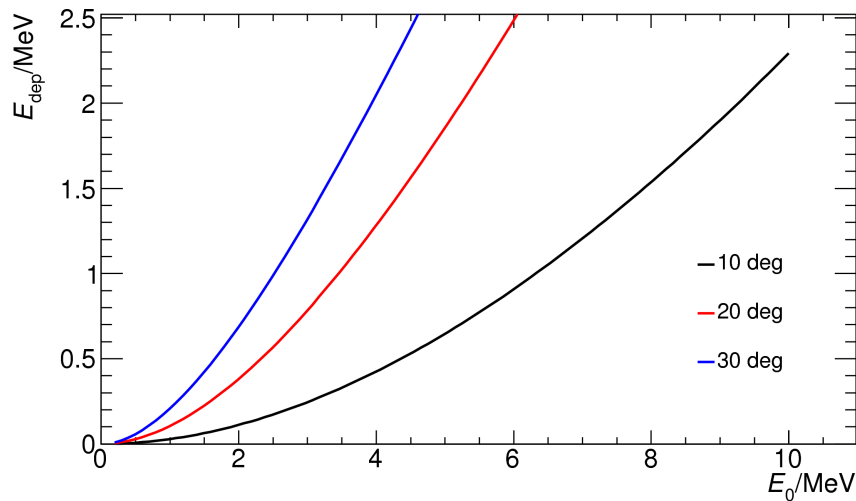


Figure 2.11: Deposited energy in Compton scattering over the incident energy for three different scattering angles.

Since the camera is meant to resolve structures in the millimeter range, the intrinsic resolution must not be worse than several millimeter. Therefore, there is no sense in a detector with a lateral resolution, i.e. pixel size in pixelated detectors, larger than 1 mm because this measure translates geometrically into the image plane and the detector distance is smaller than the distance to the patient. On the other hand, pixels much smaller than that might also be not feasible. The reason is that the charge cloud generated in semiconductors is the bigger the larger the energy deposition is. In [Zha09] the charge cloud diameter in CdZnTe was simulated. An energy deposition of 1.3 MeV can cause a charge cloud whose diameter ranges up to 1 mm. Such events lead to charge sharing among the pixels. This value can easily be reached in this application as figure 2.11 illustrates because the incident

energy is in the range of several MeV. A pixel pitch much smaller than 1 mm would therefore be of no advantage since the generated charge always extends over several pixels. A pixel pitch and thereby a spatial resolution in the worst case of 1 mm was assumed in the calculations.

The distance l of detector layers was set to 4 cm in the resolution calculations. This number is in a practical range of what is expected from an actual prototype. It has been chosen to be comparable to the expected detector size of the prototype system. The closer the layers are together the better the efficiency because more scattered photons can reach the second detector. On the other hand, the geometrical uncertainty becomes larger.

The longitudinal uncertainty, i.e. the depth-of-interaction resolution, was set to 0.5 mm. This should be within practical reach with the methods explained in section 1.3.1.

These numbers translate to a geometrical error of about 2.2 degree when using the approximation (2.14). This value has been used for the uncertainty on the measurement of φ_2 .

2.2.2 Efficiency

The efficiency ε in the context of this analysis is defined as follows:

$$\varepsilon = \frac{\text{number of photons with a valid event history for cone calculation}}{\text{number of photons incident on the first detector layer}}. \quad (2.15)$$

As emission scenario for this analysis it has been decided to have the photons evenly distributed over the first layer. The momentum is perpendicular to the detector surface. This scenario corresponds to a point source at infinite distance. In practice, photons will enter from various directions as the emission distribution will be of finite size in finite distance. However, this highly depends on the irradiation target and it has been decided to keep this analysis independent of a specific target. The evenly distributed, parallel photon field is the one generic scenario which is closest to the practical case.

The “valid event history” is a sequence of interactions which makes it possible to calculate a cone for image reconstruction. Dependent on the Compton camera technique, this can be different. In 2-Compton mode, the valid sequence is:

- (1) The incident photon is Compton scattered.
- (2) The scattered photon leaves the detector layer in which it was scattered.
- (3) It reaches another detector layer which is behind the scattering layer.
- (4) The photon is completely absorbed in this layer.

In 3-Compton mode, the sequence is:

- (1) The incident photon is Compton scattered.
- (2) The scattered photon leaves the detector layer in which it was scattered.
- (3) It reaches another detector layer which is behind the scattering layer.
- (4) Another scatter event occurs.
- (5) The scattered photon leaves the layer.
- (6) It reaches another detector layer which is behind the second scatter layer.

- (7) An interaction in this layer of any kind takes place.

In these histories, the layers which are hit are required to be ordered. Backscattering events are considered to yield invalid histories. The assumption behind this criterion is that the actual detectors will not have a sufficient time resolution to order the hits according to their occurrence. Since forward scattering is preferred for all materials under consideration in the MeV energy range, this is assumed to be a weak restriction which will most probably be realized in a real system.

The probability with which a photon incident on the detector stack undergoes an event sequence which is suitable for cone reconstruction cannot be evaluated by analytical means. Although a semi-analytical model has been developed for the simpler *scatter-absorber* technique by decomposing the total efficiency in the probability for

- a Compton event,
- the scattered photon leaving the scatter layer and
- of being absorbed in another detector.

However, many simplifications are required to keep the calculations feasible so that results from this approach are questionable. The most significant simplifications are the assumption of axial symmetry and Compton interactions were assumed to happen at a fixed depth in the detector. The first assumption becomes problematic if the detector distance is of the order of magnitude of the detector side length. The second assumption requires that the layer thickness is much smaller than the distance. Both suppositions restrict the camera geometry which can be handled in the analytical model.

For the *scatter-scatter* technique, an analytical approach is not feasible because of the many combinations of scatter events in different layers that lead to valid photon histories. Therefore, the analytical model has been abandoned and a Monte Carlo approach was pursued.

A particle transport code for evaluating ϵ has to support the following features:

- Photon transport with the following interaction modalities:
 - Photoeffect,
 - Incoherent scattering,
 - Pair production;
- Geometry support for stacks of rectangular layers;
- Material support for germanium, cadmium zinc telluride and silicon.

Only very few features are required. For the efficiency calculation, only photon transport is needed. Since photon interaction happens in discrete points, this is simple to treat computationally compared to the interaction of charged particles. For this work, the transferred energy can be considered to be deposited locally. This holds as long as the detector granularity is large compared to the secondary particle range. The same restriction appeared in the treatment of the angular resolution and has to be fulfilled anyway in this study. No advanced geometry has to be treated as long as the influence of passive construction material can be disregarded. Only very few material tables have to be present in the code. It is even possible to omit the air since the interaction of photons between layers is negligible.

In principle, a fully featured code like Geant4 [Ago03] is suitable for this task. Nevertheless, it would have had to be down-tuned in order to assure efficient calculations. Additionally, the implementation of the event analysis would be prone to errors due to the many available quantities simulated in a comprehensive particle transport code. Therefore, it was decided to implement a custom photon transport which is restricted to the simulation of efficiency data.

The Monte Carlo code is realized in the framework of the Root library *libCompton*. The central class managing the transport is `CTrackManager`. It has to be initialized with the geometry including the layer materials. These information are encapsulated in the `CEventHeader` class. Cross section data stem from the XCOM database [XCOM]. Photoelectric absorption, incoherent scattering and pair production in the nuclear electric field are handled. All physical material data is managed within the `CXSection` class. With geometry and material data available, `CTrackManager` provides the `CTrackManager::Run` public member function that actually performs the simulation. This includes the propagation of a photon which is described in terms of a `CPhotonState` object which includes energy, position and direction. The physical interaction is performed as follows. `CXSection` provides a member function `CXSection::GetProcess` which returns a process name and a depth at which this process would occur. Two random numbers r_1 and r_2 are required. r_1 is drawn from the interval $[0,1)$ and decides on the type of process based on the total XCOM mass attenuation coefficients $(\mu/\rho)_{\text{ph}}$ for the photoelectric effect, $(\mu/\rho)_{\text{incoh}}$ for incoherent scattering and $(\mu/\rho)_{\text{pair}}$ for pair production:

$$\begin{aligned}
 0 \leq r_1(\mu/\rho)_{\text{total}} < (\mu/\rho)_{\text{ph}} & \Rightarrow \text{photoelectric effect} \\
 (\mu/\rho)_{\text{ph}} < r_1(\mu/\rho)_{\text{total}} < (\mu/\rho)_{\text{ph}} + (\mu/\rho)_{\text{incoh}} & \Rightarrow \text{incoherent scattering} \\
 (\mu/\rho)_{\text{ph}} + (\mu/\rho)_{\text{incoh}} < r_1(\mu/\rho)_{\text{total}} < (\mu/\rho)_{\text{total}} & \Rightarrow \text{pair production}
 \end{aligned} \tag{2.16}$$

$$(\mu/\rho)_{\text{total}} = (\mu/\rho)_{\text{ph}} + (\mu/\rho)_{\text{incoh}} + (\mu/\rho)_{\text{pair}}$$

The second random number r_2 is the depth of interaction and is generated according to an exponential function whose parameter depends on the type of process which has been selected. The distribution function $f(r)$ from which r_2 is generated is

$$f(r) = \exp(-r\rho(\mu/\rho)_{\text{process}}). \tag{2.17}$$

`CTrackManager` verifies if the interaction depth lies within the volume. If not, the photon is not supposed to interact in the volume.

If the interaction is an incoherent scatter event, the member function `CXSection::GetCosScatterAngle` is called which returns a scatter angle and a new energy by using the Klein-Nishina expression for the differential cross section (1.3). The scatter angle is drawn by using the Klein-Nishina cross section as distribution function. The `CPhotonState` object is then updated with its new energy and direction.

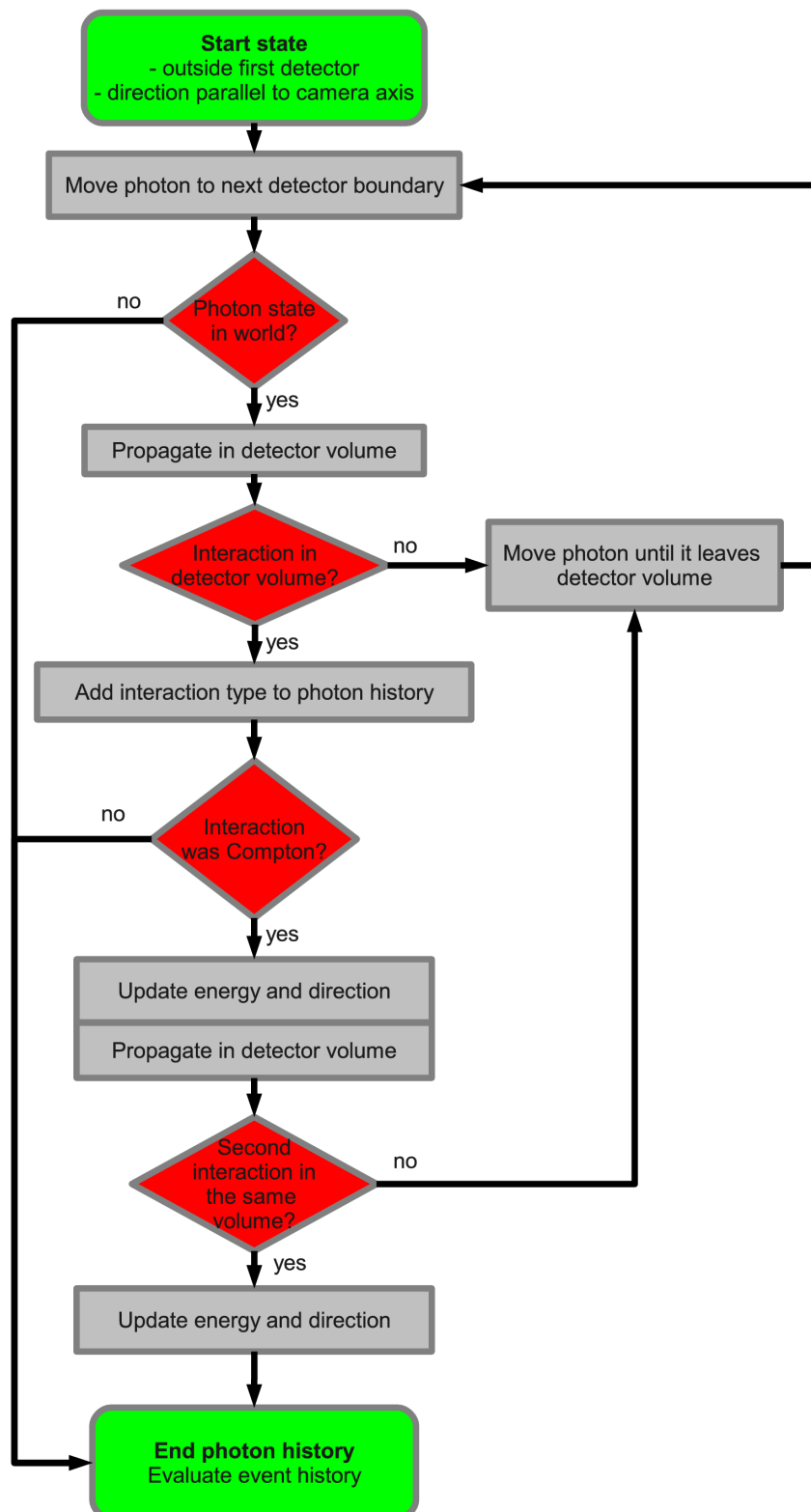


Figure 2.12: Flowchart of the simulation of a single photon history in the efficiency simulation.

How the simulation of a photon history is handled in the `CTrackManager::Run` method is illustrated in the flowchart in figure 2.12. The simulation is aborted in three cases:

- The photon leaves the “world”, i.e. it leaves a bounding box around the detector stack with no chance of hitting it again.
- An interaction other than incoherent scattering happens.
- The photon interacts in the same detector layer twice.

If something different than a scatter event happens, there is no scattered photon which can be further tracked by the code. The third point has been implemented in the assumption that the detector will not be able to distinguish two events happening at nearly the same time. There are detector concepts in which this is possible. However, the effort on the front-end-electronics side is very high[†]. Such events can also be caused by two independent photons.

All interaction types are recorded and at the end of the run the sequence is evaluated whether it is a valid sequence in the sense explained above. The number of valid sequences is divided by the total number of simulated photons. The efficiency in 2- and 3-Compton mode is stored together with the geometry and the energy of the incident photons in a `CRunResult` object which is available for later analysis.

2.3 Results

The expected angular resolution in 2-Compton mode is plotted in figure 2.13 as a function of the scattering angle for three different incident energies. The upper row displays the result for silicon, the middle row for germanium and the lower row was calculated for cadmium zinc telluride. The total ARM is the square root of the quadratic sum of all contributions.

The geometric error affects the cone axis. Therefore, these components are independent of the scattering angle. The shown curves have been calculated for a pixel size of $1\text{ mm} \times 1\text{ mm}$ and a depth resolution of 0.5 mm . The energy resolution of the scatter detector is important at small scattering angles while the energy resolution in the absorber detector dominates at large scattering angles. The same holds for the Doppler broadening. It is less important in the case of small angle scattering.

When comparing the three simulated energies of 0.5 MeV , 1 MeV and 2.2 MeV , one finds that energy and Doppler components decrease with increasing energy. Their influence on the total ARM disappears first in the small scatter angle regime and then also at larger angles. The geometry errors remain constant in this model. However, in reality they will be larger at energy depositions above 1 MeV like its was discussed above.

A comparison of the three materials yields that CdZnTe performs considerably worse at 500 keV than silicon and germanium. The ARM of the latter two materials are already close to the geometric limit of 2.2 degree while Doppler broadening and energy resolution cause

[†]) Pixel detectors with depth-of-interaction information are for example capable of evaluating such events. Neither the strip detector layout nor the Anger principle block detector which has been used in the prototype system are able to distinguish two simultaneous hits.

an ARM of more than 3.5 degree at most scattering angles in CdZnTe. Nevertheless, already at 1 MeV CdZnTe is nearly as good as the other two materials up to 45 degree. One has to have in mind that the larger scattering angles become less likely with increasing energy. At 1 MeV, a CdZnTe system is therefore expected to perform nearly as good as a HPGe system in most cases. This trend is continued at 2.2 MeV.

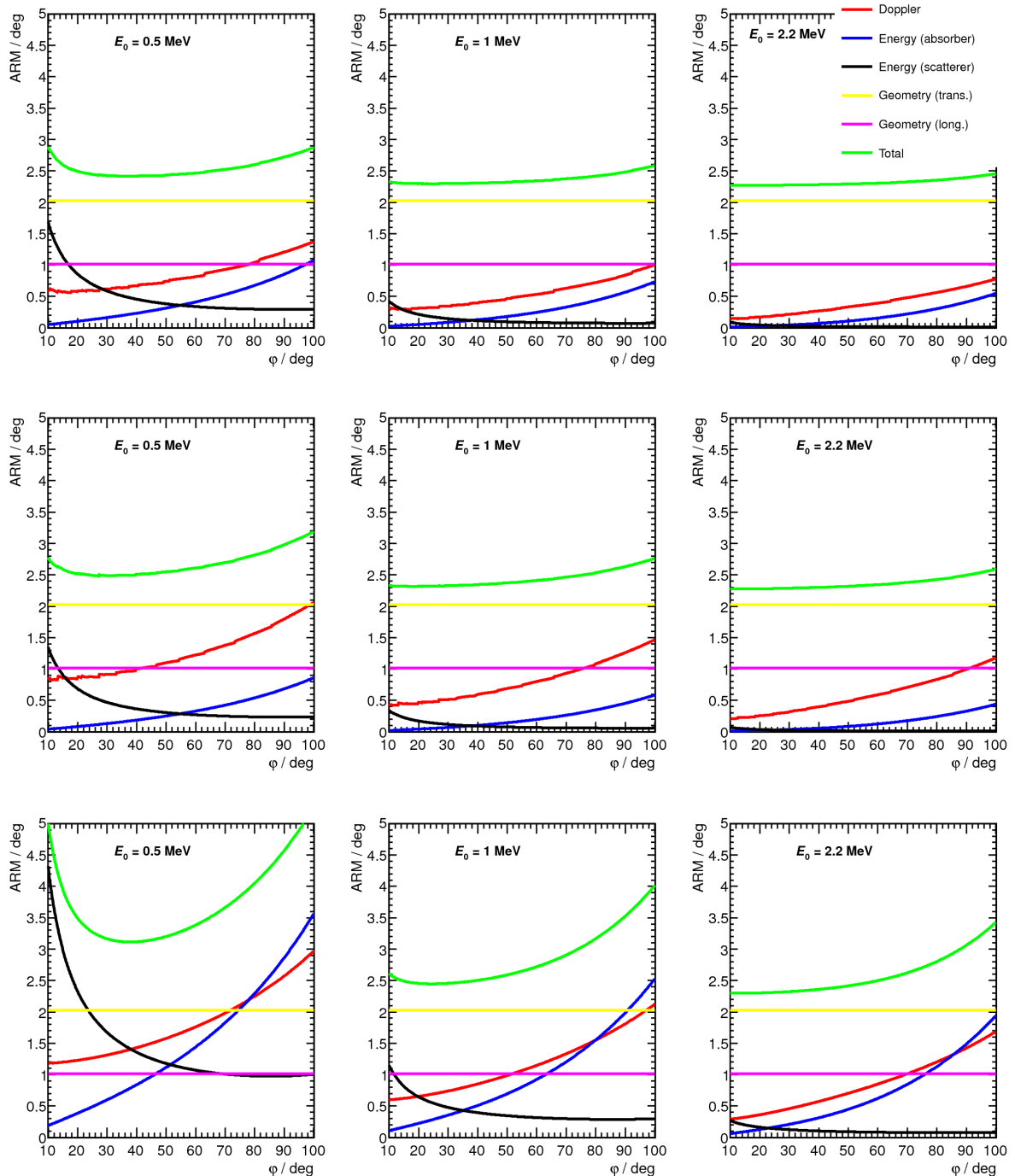


Figure 2.13: The contributions to the ARM in 2-Compton mode for three different energies. The upper row is for a homogenous silicon system, the middle row for germanium and the lower row for cadmium zinc telluride.

2.3 RESULTS

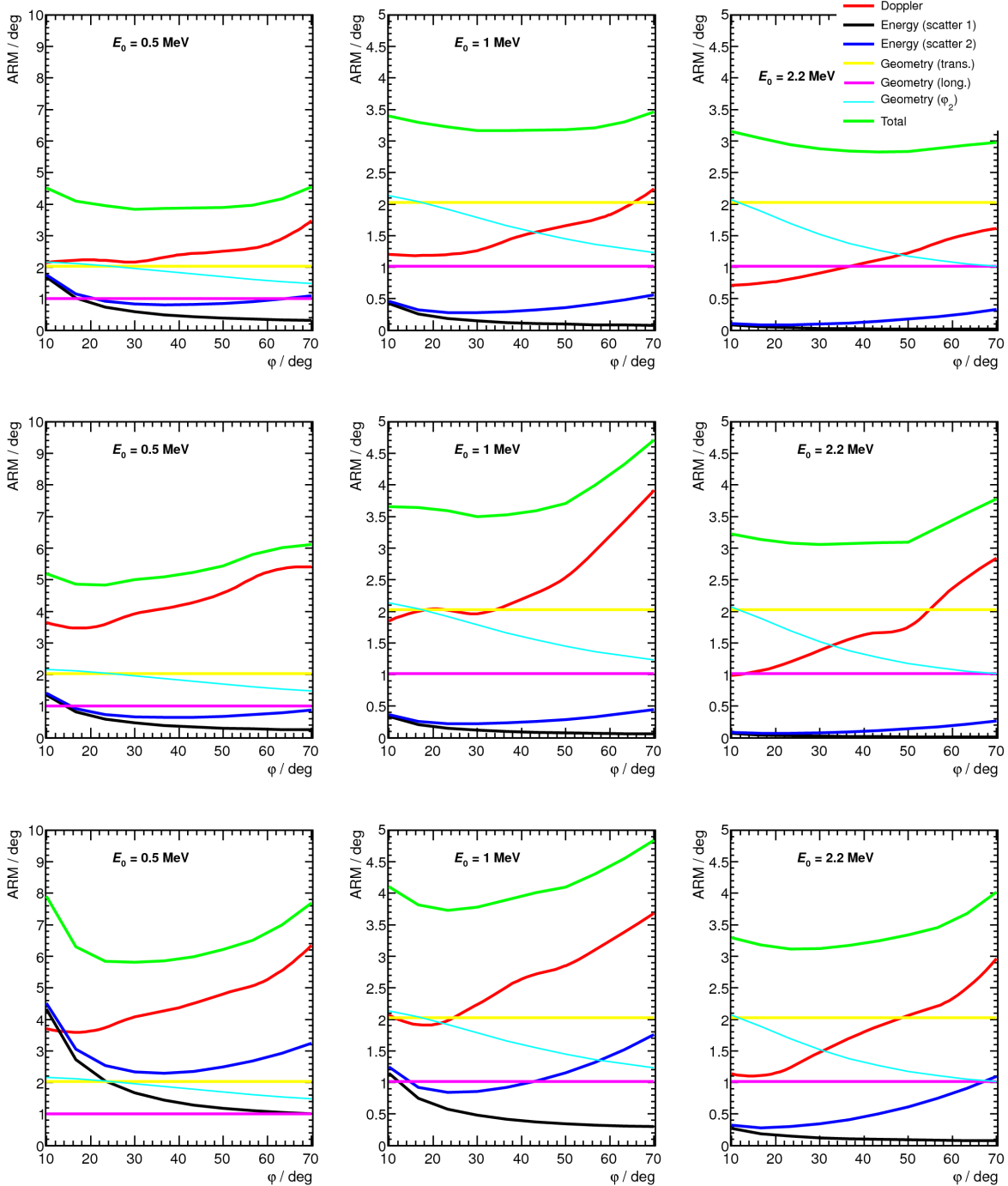


Figure 2.14: The contributions to the ARM in 3-Compton mode for three different energies. The upper row is for a homogenous silicon system, the middle row for germanium and the lower row for cadmium zinc telluride.

The results for the *scatter-scatter* mode are shown in figure 2.14 in the same manner than in the previous figure. There is an additional component due to the additional measurement of ϕ_2 . The ordinate at 0.5 MeV is scaled from 0 to 10 degree while the scale reaches only up to 5 degree at the other energies. Another feature of these plots is that the Doppler curves are less smooth than in the scatter-absorber case. The Doppler results originate in simula-

tions whose results are subject to statistical fluctuation. For the results in this graphic, 10 000 events have been simulated for each point on the curves.

The contribution from the energy resolution are comparable to those in 2-Compton mode. Doppler broadening has a larger influence than before since it occurs in two interactions instead of one. The increased Doppler component and the additional geometrical contribution result in a considerably worse performance than in the case of the simpler technique. While the tendency of better ARM the higher the energy is reproduced. The overall resolution does not drop below 3 degree. At 1 MeV it is even above 4 degree for most angles in a CdZnTe system.

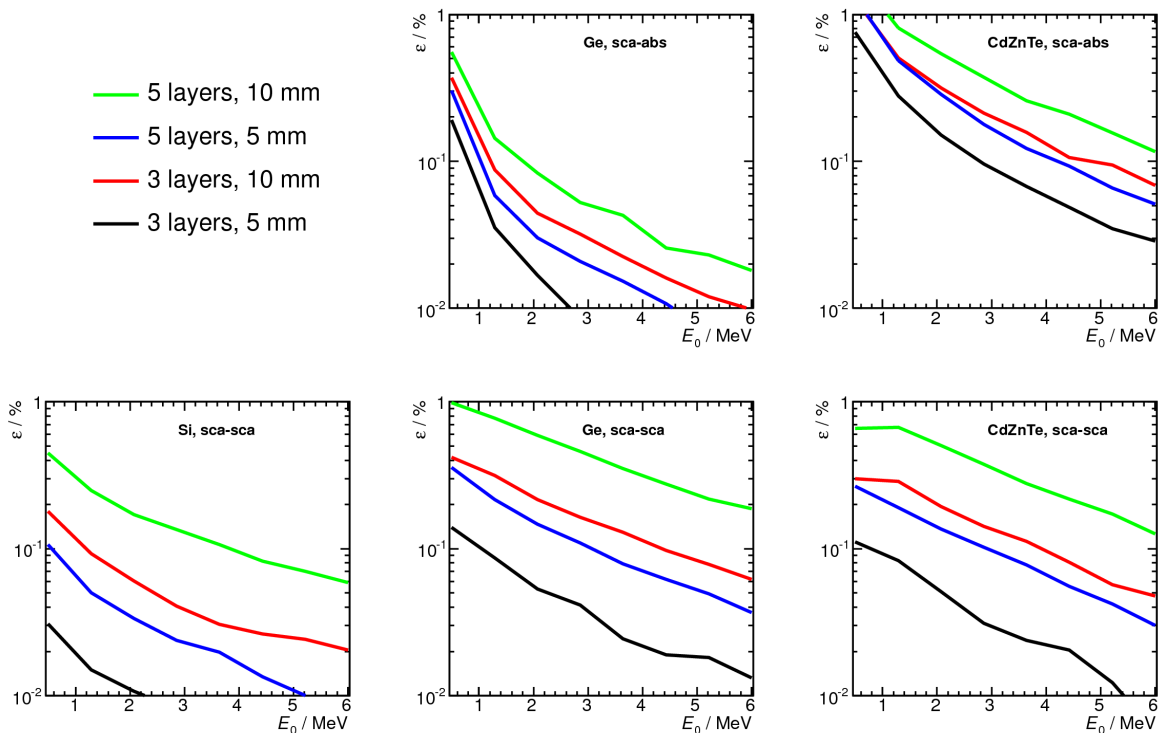


Figure 2.15: Simulated efficiency for homogeneous stacks of detectors of different material. The data was simulated with 400 000 events for each point (“sca-abs”: scatter-absorber mode, “sca-sca”: scatter-scatter mode).

The simulated efficiency over the energy of the incident photons is plotted in logarithmic scale in figure 2.15. Systems of three and five identical layers with a quadratic surface of $12\text{ cm} \times 12\text{ cm}$ have been simulated. The layer thickness was chosen to be 5 mm and 10 mm. The upper row is the efficiency in *scatter-absorber*, the lower row in *scatter-scatter* mode, i.e. only events of the respective type contribute to the efficiency. The data for the silicon system is shown in the left column, germanium in the middle column and cadmium zinc telluride in the right column.

There is no data displayed for silicon in the scatter-absorber mode. The efficiency of this configuration is at least three orders of magnitude lower compared to the other setups. The reason is the very low probability for an absorption of an MeV photon in a silicon slice of a couple of millimeters thickness. Using silicon in the absorber stage is therefore futile. However, in *scatter-scatter* mode, silicon is reasonably efficient so that this data is shown here.

All curves drop steeply with increasing energy. However, the decrease is less steep in the *scatter-scatter* mode. More and thicker layers naturally results in higher efficiency. Increasing the number of layers from three to five approximately doubles the efficiency. If more material is available, it is therefore advantageous to add more layers instead of increasing the detector area.

A comparison between the materials reveals that a higher atomic number gives more valid events in *scatter-absorber* mode. Nevertheless, germanium is the most efficient material in *scatter-scatter* mode, although CdZnTe performs nearly as good. In the curves which were simulated for the thick CdZnTe setup, an increase in efficiency at low energies is visible until the curves reach their maximum and drop off. This is due to the absorption in the material which competes with incoherent scattering.

2.4 Conclusions

Based on data from this design study, the following conclusions can be drawn:

- (1) A Compton camera system based on semiconductor detectors with a plausible geometry and a practically manageable readout scheme would be able to deliver cone data with an angular resolution measure of about 2 to 3 degree. If this number would directly translate into the final image, the spatial resolution would be around 10 mm if the detector system is placed at a distance of 25 cm. What is required for clinical applicability cannot be answered in general. PET monitoring reaches millimeter accuracy from approximately 6 mm spatial resolution and is thereby well below the positioning uncertainty of 3 mm [Hel12]. The expected Compton camera resolution might therefore be still sufficient but still on the brink of what is required for clinical relevance. There are however two points which suggest that such a system might nonetheless deliver valuable data:
 - The sources of uncertainty are well known and they can be modeled and included in the image reconstruction algorithm. The algorithm could be capable of recovering a part of the resolution lost in the various processes like it has been shown for the image blurring due to the positron range in PET (e.g. [Bai03]).
 - The final purpose is to detect deviations from the planned dose. If this works like in the case of in-beam PET by means of the comparison of an expected emission distribution and an actually measured distribution, deviations in the order of one millimeter could even be detected if the two data sets do not have this intrinsic resolution. This requires validated simulations to have reliable reference data.
- (2) The total efficiency drops steeply with increasing incident energy. Although high energies are preferred in terms of angular resolution, low statistics will degrade the image quality. Concentrating on the 2.2 MeV γ -ray-emission and the statistical γ -rays with lower energy is therefore recommended. If a Compton camera can be efficient enough for reconstructing relevant images from the data taken during irradiation cannot be answered easily. As discussed in the introduction to this section, beam delivery and target properties are crucial. But even assuming certain numbers in this respect still leaves open how many events at which quality are needed for a useful

image. And finally, the number of valid events also depends on detector speed and the capability of reconstructing the actual hit sequence.

- (3) The simple 2-Compton mode results in good angular resolution and even has a good efficiency as long as there is an efficient absorber stage. The advanced 3-Compton technique can deliver data of useful quality only above an energy of about 1 MeV. Although an additional interaction is required, it can be more efficient as the 2-Compton mode. A camera module capable of both techniques should therefore be pursued in order to combine the both efficiencies in the same hardware. Filters can then be implemented to decide which type of data has to be used in what energy range.
- (4) Thick silicon detectors are only useful in the *scatter-scatter* regime since they lack any absorption qualities. Germanium combines an excellent resolution with a reasonable efficiency in the *scatter-scatter* technique. CdZnTe is affected by large Doppler broadening and a low energy resolution compared to the other two types of detectors. However, the difference in terms of angular resolution becomes marginal above 1 MeV. CdZnTe offers also good absorption properties and thereby a good efficiency in *scatter-absorber* mode. CdZnTe should therefore be further investigated.

This design study has given an idea about what can be expected from a Compton camera system with in-vivo dose monitoring in mind. It has however also been revealed where there is a lack of practical data. The following three open questions became obvious:

- (1) What are the demands of the image reconstruction in terms of data quality and quantity?
- (2) How efficient can the event selection be under clinical conditions?
- (3) Is the CdZnTe detector technology feasible for this application?

These cannot be answered in terms of simulation but require the construction of a minimal detector system which has to be deployed in beam experiments. This detector system and its performance will be described in the next section.

3 Prototype System

The previous chapter resulted in a number of questions which can be answered by the construction of a minimal Compton camera system. Minimal in this sense means that the system has to be capable of delivering data suitable for image reconstruction. However, it is not aimed to implement the final design for a clinical prototype nor is it meant to be scalable or to provide the needed data rate for clinical imaging. The system designed and constructed in this work is intended as an evaluation platform for the CdZnTe technology in the in-vivo dosimetry context and to generate real data to challenge the image reconstruction.

The results presented in this chapter stem from measurements in the laboratory with radioactive point sources. The camera system and results from these experiments have been published in [Kor11a] and [Kor12]. The system has also been deployed at a hadron beam line. Those experiments are presented in section 4.

3.1 Overview

The initial design foresaw a detector stack with three layers: two identical CdZnTe detectors followed by a scintillation detector. This is the minimal design to be able to record *scatter-scatter* events if there is no way of discriminating multiple hits in the same detector volume. CdZnTe is available in the standard size 20 mm × 20 mm × 5 mm. Larger crystals are available, but those are special productions with high prizes and long delivery times. Moreover, each of those detectors is a prototype with unforeseen properties. The major aim of this project is technology evaluation. The standard detectors are well suited for this purpose. However, the small area will result in a poor efficiency. To allow measurements with decent event numbers, the efficiency is in this design boosted by an absorption stage with larger dimensions. Readily available is an integrated LSO block detector which comprises a crystal matrix of 52 mm × 52 mm × 20 mm coupled to 2 × 2 photomultipliers. The design is schematically shown in figure 3.1.

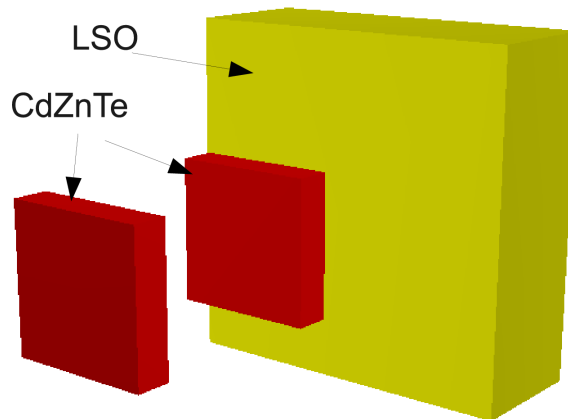


Figure 3.1: The initial detector design was supposed to be constituted of two layers of CdZnTe detectors followed by a larger scintillation plane.

The second cadmium zinc telluride detector which was delivered by the manufacturer had a very poor electron lifetime-mobility product in the order of $\mu\tau = 4 \times 10^{-4} \text{ cm}^2/\text{V}$ (data from the manufacturer) such that it was not suitable for spectroscopic measurements. The camera system therefore lacks the ability to explore the *scatter-scatter* mode. Nevertheless, all other components have been developed with an additional detector layer in mind so that it can easily be added without further modifications at a later time when an appropriate crystal is available.

Besides the detectors, front-end(FE)-electronics, data acquisition (DAQ) hardware and readout software with a decent connection to the image reconstruction are needed for successful measurements. An overview of these elements is schematically shown in figure 3.2. All these components and their interplay are presented in the following section.

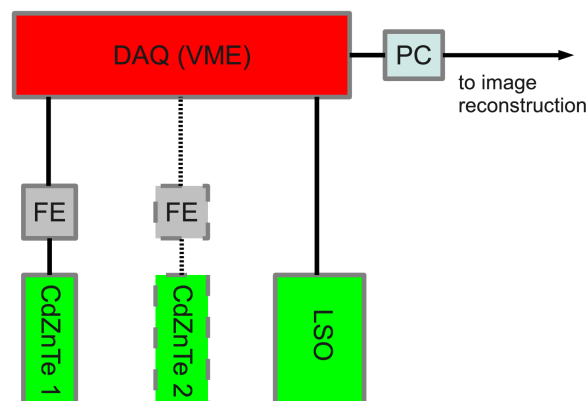


Figure 3.2: Schematic overview of the camera system. The second CdZnTe detector is foreseen.

3.2 System Components

3.2.1 CdZnTe Detector and its Front-End-Electronics

The cadmium zinc telluride crystals for this project have been obtained from Baltic Scientific Instruments, formerly Bruker Baltic, in Riga, Latvia. The one crystal which has been deployed in the camera system was grown by Redlen Technologies, Saanichton, Canada, and has been contacted and assembled in Riga. The mobility-lifetime product $\mu\tau$ for electrons was given by the manufacturer to be around $10^{-2}\text{cm}^2/\text{V}$. The dimensions of the crystals are $20\text{ mm} \times 20\text{ mm} \times 5\text{ mm}$ which is a standard size in crystal production.

It has been decided to apply a double sided cross strip electrode layout instead of a pixelated design. This means that anode and cathode are segmented in strips in such a way that anode and cathode strips are orthogonal to each other. A single hit in the detector would ideally induce charge on one anode and one cathode strip only. Reversely, a hit that triggered one strip on each side can be mapped back into the detector volume where the two strips intersect. The mapping process is however not bijective in the case of more than one hit at approximately the same time. Two hits can produce up to two triggered electrodes on each side which intersect in four places. A cross strip design implies that the count rate on the whole detector must not be too high to exclude such events which a pixel detector would be able to resolve. This is feasible in an evaluation system but has to be questioned when it comes to clinical applicability.

What makes the strip detector very attractive for an evaluation system is that considerably fewer readout channels are required to achieve a given spatial resolution compared to a pixel detector. A cross strip detector with n strips of equal pitch on each side has $2n$ channels, but is segmenting the detector volume into n^2 segments. This makes it possible to implement front-end-electronics based on discrete readout channels while the high channel density in a pixel detector could not be handled efficiently with standard components. The use of integrated circuits would be required. A scalable camera module will certainly have compact, integrated electronics. But for the evaluation and research approach of this study, the discrete electronics design offers more flexibility like quick access to detector pulses or the possibility to replace components easily.

Electrode Design and Crystal Mounting

The design parameters of the electrodes have been sent to Baltic Scientific Instruments whose engineers developed the final electrode layout. Both anode and cathode are segmented into 16 strips with a pitch of 1.05 mm. The anode is surrounded by a guard ring which will be grounded in order to keep surface currents and its fluctuations from the anodes. Furthermore, there is a steering electrode in grid shape on the anode. It will not be read out but be kept at a certain potential. The anode strips are chosen to be line-like with a thickness of 0.1 mm to achieve a good small-pixel effect. The grid is with 0.2 mm twice as wide as the strips. The cathode strips cover the inner area of the grid so that they do not sense charge that would be visible to the anodes. The cathode strip pitch is the same as for the anodes. But the strips are wider; they are covering the whole area with only 0.2 mm gaps in between. The technical drawing from Baltic Scientific Instruments is attached in appendix A.1. The electrodes on the detector before being assembled are shown in figure 3.3.

The electrode design is inspired from the design developed in [Gu11]. The weighting potential of an anode strip is expected to be of the shape shown in figure 1.9. Although $\mu\tau$ is not known prior to designing the electrodes and the weighting potential has not been calculated, it can be expected that the condition of eq. (1.22) is approximately met. Furthermore, the implemented electrode design will give depth-of-interaction information through the cathode-to-anode signal ratio C/A according to eq. (1.23).



Figure 3.3: Left: anode electrode of the CdZnTe detector. Right: cathode side (images by Baltic Scientific Instruments).

The crystal cannot be glued to a substrate because it has segmented electrodes which have to be electrically isolated. Additionally, it is unwanted to have material in front of and behind the detector to avoid scattering in non-sensitive substance. The only way to mount the crystal is to glue it into a frame which supports the crystal and provides connections to the individual electrodes while it leaves the anode and cathode side untouched. A frame with connectors has been developed by Baltic Scientific Instruments. The assembly is shown in figure 3.4.

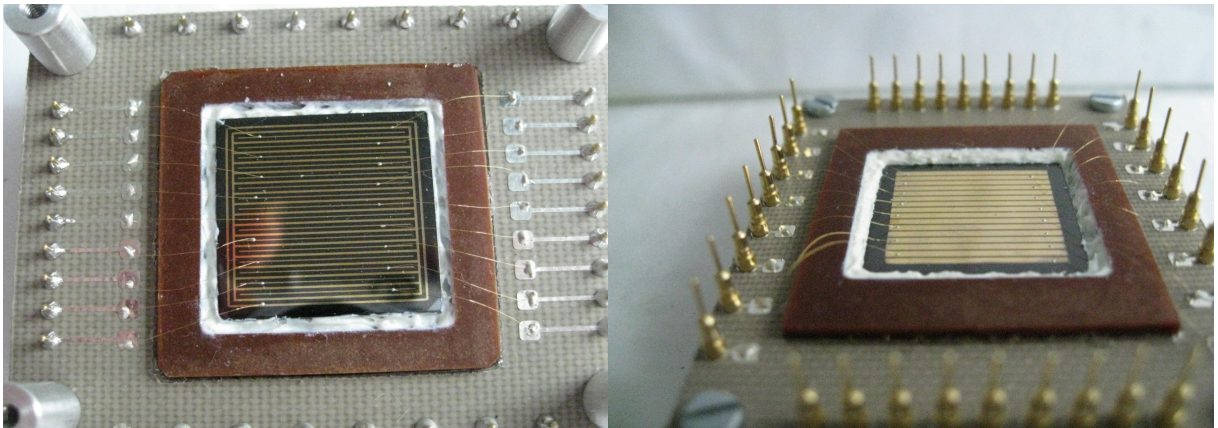


Figure 3.4: Left: detector assembly from the anode side. Right: cathode side view (images by Baltic Scientific Instruments).

The electrodes are wire-bonded to pads on the frame which are connected to pins. The strips are connected in alternating order to left and to right. The guard ring and the steering grid have their own pins as well. The pins stand out on the cathode side where the assembly is mounted to the front-end(FE)-board.

3.2 SYSTEM COMPONENTS

It can be seen that the crystal is not entirely in line with the frame. It is a bit tilted to the left in the view on the anode. This adds up to other sources of uncertainty in the detector positioning in the entire system.

This assembly is not directly mounted on the FE-board but confined in an aluminum housing for electromagnetic and light shielding. The housing has windows in front of and behind the detector which are covered with black tape. The pin connectors are repeated on the back side of the housing to connect to the FE-board.

Front-End-Board

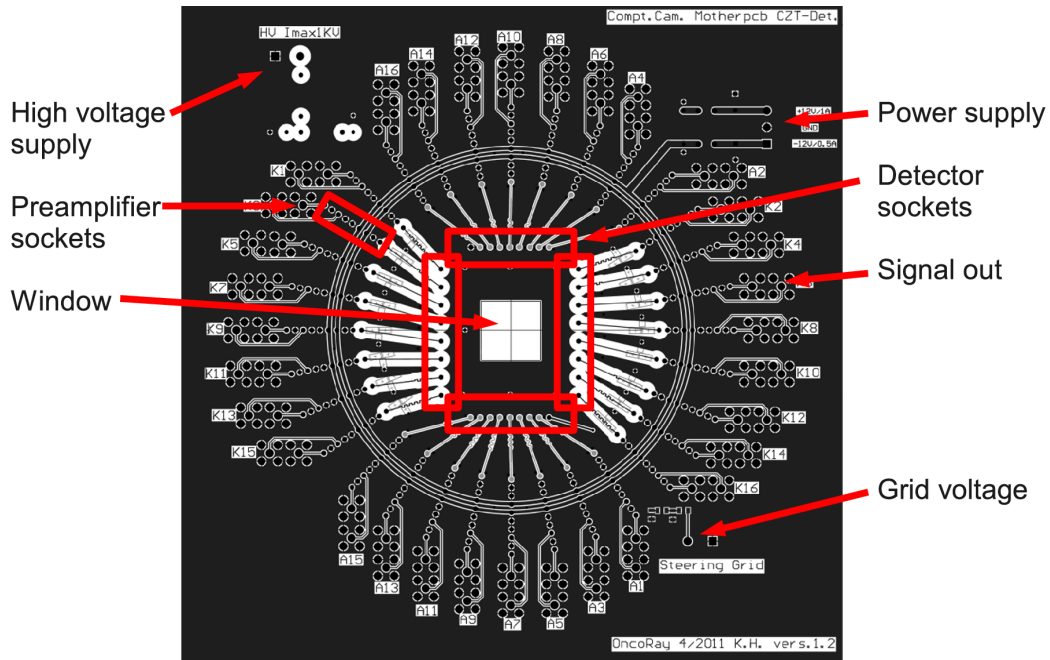


Figure 3.5: Front side of the front-end-board which supports the CdZnTe detector and its preamplifiers (drawing by Klaus Heidel, HZDR).

The FE-board (figure 3.5) supports the preamplifiers and provides the high voltage to the electrodes and power to the preamplifiers. Each anode and cathode strip is connected to an individual preamplifier. The preamplifiers and the FE-board have been developed by Klaus Heidel at the Helmholtz-Zentrum Dresden-Rossendorf (HZDR), formerly Forschungszentrum Dresden-Rossendorf. The FE-board is a printed-circuit-board (PCB) of 200 mm × 200 mm. It features a window at the detector position which is surrounded by the pin connectors to the preamplifiers and to the bias supply for the grid and the grounded guard ring. The 32 preamplifiers are connected as daughter boards to the FE-board and are arranged in a circle around the detector. The anode channels are situated on the top and bottom, the cathode channels left and right in figure 3.5 in alternating order. The PCB tracks from the pins to the preamplifier inputs are designed in such a way that they are of equal length for all channels. The cathode channels are biased why their conductive paths are separated from the ground by 1 mm.

Nanosecond Preamplifier

The preamplifiers are of the type Nanosecondpreamplifier (NSP) and are a development by Klaus Heidel, HZDR. The NSP are based on a development of the Max-Planck-Institute in Munich for the readout of avalanche photodiodes. Referring to these modules as preamplifier is not entirely correct. The NSP contains not only the AC coupled preamplification stage, but also a simple shaper comprising one differentiator element and pole-zero cancellation. (c.f. figure 3.6).

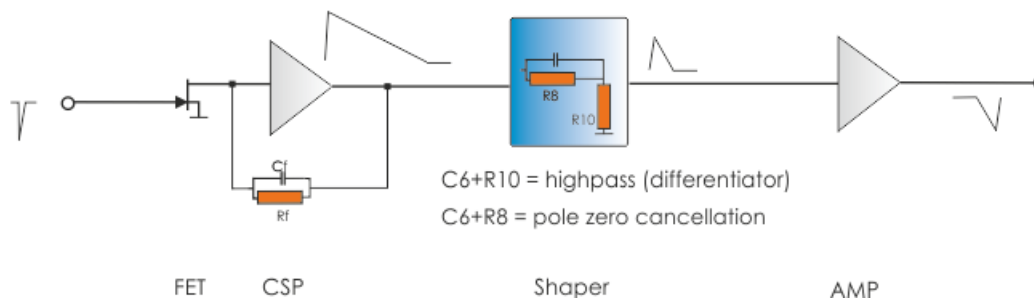


Figure 3.6: Block diagram of the Nanosecondpreamplifier (by Klaus Heidel, HZDR).

Furthermore, a slight negative offset of -5 mV is added to the output. The resulting signals are suitable to be fed into a charge-to-digital-converter (QDC). There is also a split incorporated into the NSP to provide two identical outputs. One of the signal branches is needed for trigger generation. This is discussed in section 3.2.4. The preamplifiers have been configured to work with the segmented CdZnTe crystals. Since both cathode and anode have very different characteristics, this development led to two types of preamplifiers.

The NSPs for the cathode side have to provide the negative bias to the detector. Furthermore, they must deal with positive pulses since they sense the hole motion. Because the QDCs require negative input, an inverter is included in the cathode side modules.

The anode channels do not need inversion. However, the geometry of the anode strips differs considerably from the cathode strips. This results in a different input capacity which has to be accounted for in the phase margin (i.e. the rise time the preamplifier can handle).

Each NSP module consumes 0.4 W of power. The total 32 preamplifiers dissipate 12.8 W. This power is supplied by an external power supply with passive cooling to avoid any high frequencies to leak into the signals. The power dissipation around the detector causes a rise in temperature on the detector from 20 degree Celsius to 35 degree after an hour of operation. Although no negative effects have been observed from the higher temperature, an air cooling by two fans below the upright FE-board was implemented. This keeps the crystal at room-temperature despite active preamplifiers.

A photography of the FE-board with attached NSP modules and the detector in its housing is shown in figure 3.7. The front cover of the housing is removed to have clear view on the anode side of the crystal. The housing is externally grounded. The NSP features a control diode showing the state of operation. Green shows normal operation while a red light indicates a failure on this module. Each channel has two connectors in SMB form factor for signal output.

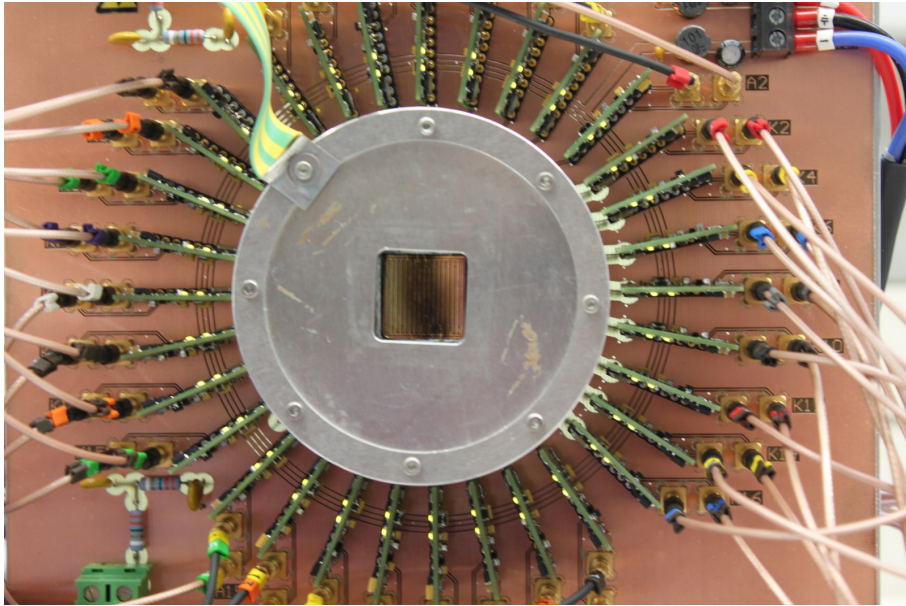


Figure 3.7: The FE-board fully populated with the detector and all powered up NSP modules.

3.2.2 LSO Block-Detector

The LSO detector is an integrated block-detector by Siemens. It is the very same detector module which is used in recent PET scanners. It features a matrix of 13×13 LSO crystals with a total size of $52 \text{ mm} \times 52 \text{ mm} \times 20 \text{ mm}^*$. Unlike in the preceding bismuth germanate (BGO) detector [Cas86], the matrix consists of discrete crystals. The matrix is coupled to 2×2 photomultipliers (PMT). The PMT have to be biased to -1050 V . The output is directly fed into QDC.

A photography of the LSO detector is shown in figure 3.9 where it is mounted together with the CdZnTe detector in a frame.

In the case of one hit in a crystal segment, the scintillation light is shared among the four PMT. All four PMT channels have to be read out to get information on the fired pixel and the deposited energy. Before however the four signals can be used together, they have to be corrected for a possibly different gain among the PMT. The total sum of all four gain-corrected channels is proportional to the deposited energy E_{dep} . If A_i are the raw signal amplitudes of the PMT $I = 0 \dots 3$ and g_i are their gain factors compared to the first PMT (implying $g_0 = 1$), the energy proportional spectrum from the block-detector is

$$E_{\text{dep}} \propto A_{\text{sum}} = \sum_{i=0}^3 \frac{A_i}{g_i}. \quad (3.1)$$

The pixel index of the fired crystal segment is found with the help of the geometrical mean of the four recorded signals. The coordinate system and the channel number of the PMT is illustrated in figure 3.8. The origin is in the center. Each hit can be mapped in the (x, y) plane with the following equation:

*) The dimensions have been verified by means of a computed tomography scan of the detector.

$$\begin{aligned}
 x &= \frac{1}{A_{\text{sum}}} \left[\left(\frac{A_2}{g_2} + \frac{A_3}{g_3} \right) - \left(\frac{A_0}{g_0} + \frac{A_1}{g_1} \right) \right] \\
 y &= \frac{1}{A_{\text{sum}}} \left[\left(\frac{A_0}{g_0} + \frac{A_2}{g_2} \right) - \left(\frac{A_1}{g_1} + \frac{A_3}{g_3} \right) \right]
 \end{aligned} \tag{3.2}$$

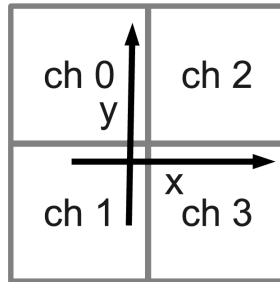


Figure 3.8: Coordinate system and channel arrangement in the LSO detector.

Signals from different pixels should be distinguishable by their (x, y) coordinates. The continuous (x, y) coordinates are mapped to discrete pixel indices (i, j) , $i, j = 0 \dots 13$. Each pixel produces a signal close to a certain point (x_{ij}, y_{ij}) . It is checked for each hit, if its (x, y) coordinates are within a certain distance to a reference point. If yes, the hit is attributed to this pixel. If it is too far from each reference point, it is discarded. Interaction maps resulting from this method are shown in the results section.

The procedure for hit mapping (3.2) is the same as for the preceding BGO detector formerly used in Siemens PET hardware (e.g. [Wur07]). The algorithm accounts for inhomogeneities among the PMT but not among the crystals. This is sufficient in the case of the BGO detector since it features a continuous crystal. In the LSO detector, the pixels are individual crystals. It has been reported that a per-pixel energy calibration can improve the detector performance[†]. This advanced method was however not implemented in this work.

3.2.3 Mounting Frame

The CdZnTe and the LSO detector are mounted on the frame shown in figure 3.9. The CdZnTe FE-board is mounted upright. The center of the LSO detector is at the same height as the center of the CdZnTe detector. The distance of the two detectors to each other can be adjusted by moving either the CdZnTe mounting or the LSO mounting. A second CdZnTe with the same geometry is foreseen on the frame. Below the CdZnTe board, the cooling fans are installed.

[†]) M. Kempe, Helmholtz-Zentrum Dresden-Rossendorf, private communication.

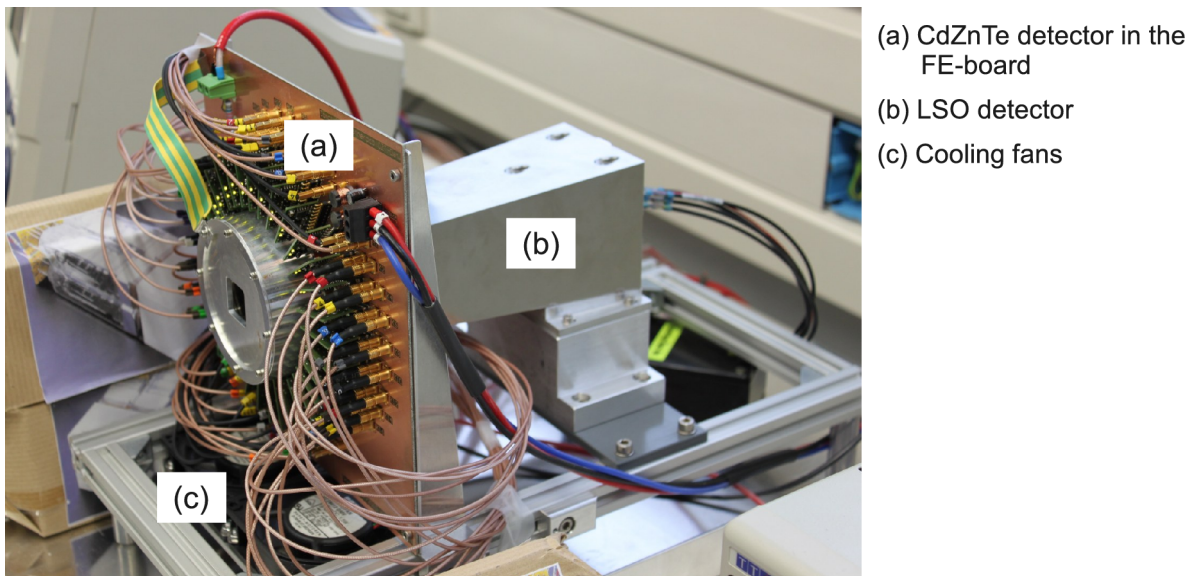


Figure 3.9: The detectors in the mounting frame.

3.2.4 DAQ Hardware and Software

The data acquisition (DAQ) system is implemented in VME modules. VME (Versa module eurocard-bus) is a backplane bus system which allows different DAQ modules to be connected via a common data bus to a controller board. This controller board can communicate with the modules and transfers the data to a PC where additional data evaluation can be programmed. All modules are housed in one dedicated VME crate. The data flow will be described from the detector to the image formation algorithm in this section.

The DAQ implements a classical fast-slow signal chain. In such a scheme, the analogue signal is split into two paths. One signal is used to generate a fast trigger signal. The other branch is delayed about the time the logic needs to generate the trigger. Once an event is registered, the delayed signal is spectroscopically evaluated.

Trigger Logic

The actual implementation of this readout principle of the detector system is outlined in figure 3.10. The four analogue signals from the block-detector are fed into a custom built combined split/discriminator. This module in VME form factor has four separate inputs and four analogue and four digital outputs. The analogue output is just the same as the input. The digital outputs provide a signal of ECL level which is generated by a leading edge (LE) discriminator.

From the CdZnTe detector, only the cathode signals are used for trigger generation because they appear always before the anode signals. The anode signal rises when the electrons are very close to the anode while the cathodes are not shielded and sense therefore any charge movement instantly. This is also the reason why the anode signals do not need any delay. The signal splitter is already incorporated into the NSP. One branch is fed into another custom built LE discriminator VME module. It features 16 channels. Each channel has an own ECL output. The LE modules have been developed by Klaus Heidel, HZDR.

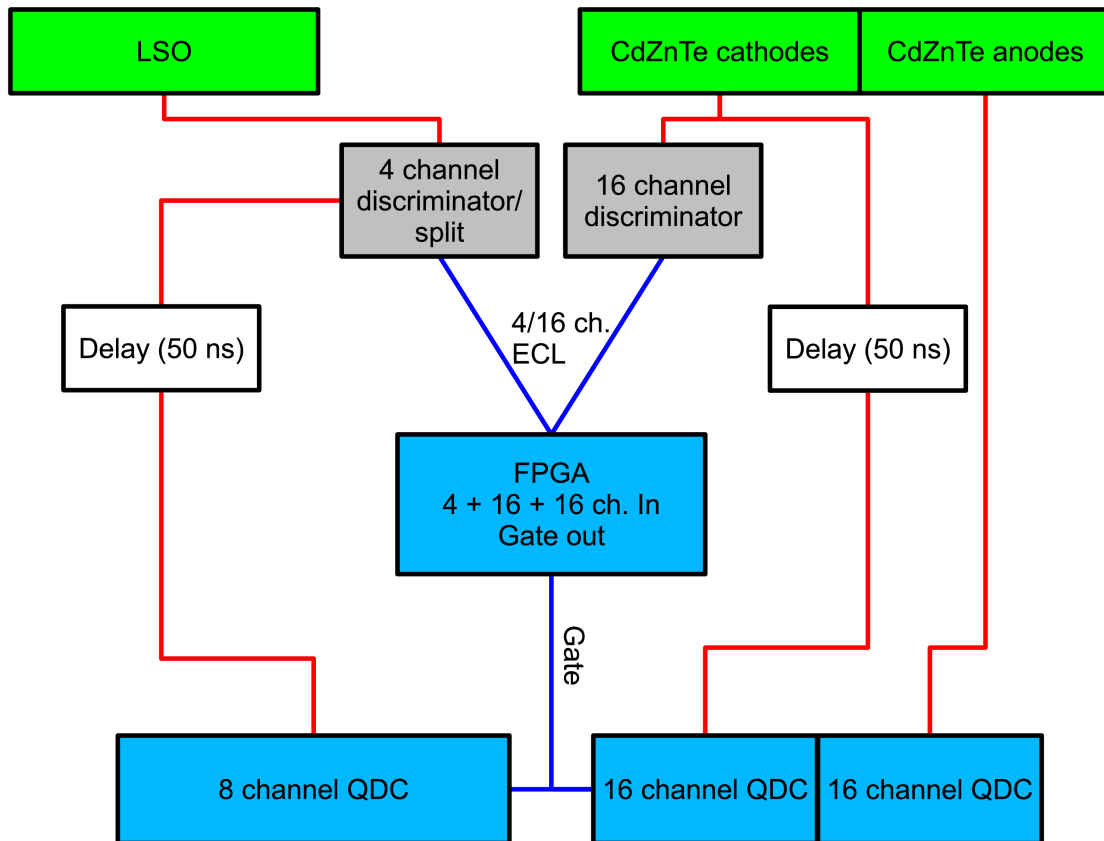


Figure 3.10: Signal paths in the DAQ system. Analog signals are colored in red, digital signals are drawn in blue.

All digital signals are fed into a V1495 FPGA board by CAEN S.p.A., Viareggio, Italy. This board provides numerous digital input and output channels. The board can be programmed via the VME bus to react on any pattern of input signals with output signals of definable lengths. The V1495 acts in this application as the central trigger instance which decides what hit pattern is required for the event to be recorded. The logic pattern programmed on the FPGA of the V1495 is illustrated in figure 3.11. The shown pattern has been translated into VHDL code by Mathias Kempe, Helmholtz-Zentrum Dresden-Rossendorf. The channel 0 to 15 on input port A come from the cathode of the first CdZnTe detector. The channels 16 to 31 are reserved for a future second CdZnTe detector. The LSO trigger signals are on the channels 0 to 3 of the input port B. Each channel can be masked, i.e. ignored in the trigger generation. Channels from one detector are combined in a non-exclusive OR. This OR operation results in 1 if at least one of the activated channels in the respective detector has been triggered. These detector triggers can be masked with an additional mask which allows to ignore the triggers from a certain detector without having to mask all channels individually. Finally, it is evaluated if at least N detectors have triggered in the event. If this is the case, a gate is generated on the output G_DOUT0. All masks, the majority number N and the gate length can be programmed by VME write operations to registers of the V1495.

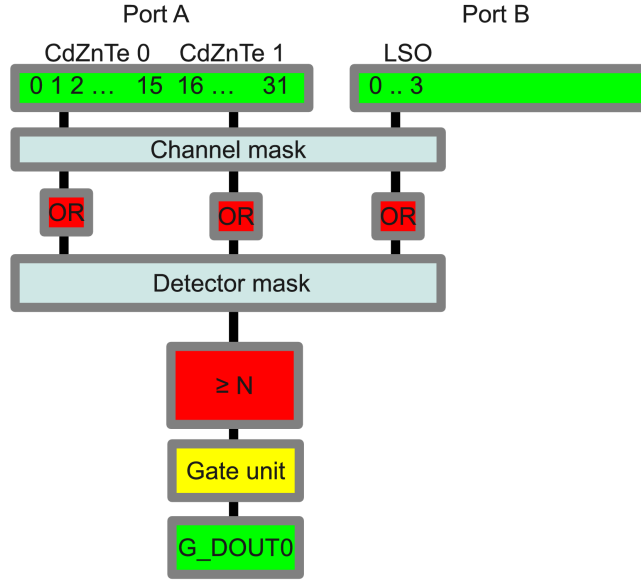


Figure 3.11: The logic which is programmed on the V1495 FPGA module.

Signal Digitization

As illustrated in figure 3.10, the gate signal gained from the V1495 is used by QDC modules to record the delayed analogue signals. The delay in this application is chosen to be 50 ns. The time required by the FPGA to generate a gate is 40 ns. The delay is realized by 8 m of coaxial cable per channel.

16 channel QDC modules of the type V965 and one 8 channel V965A modules by CAEN are used to record the signals. A QDC works by integrating a negative signal and digitizing the result. The analogue to digital converter (ADC) employed in the CAEN modules features 12 bit resolution (i.e. 4096 ADC channels). The gate signal is provided on the front panel. It is the integration interval of the analogue signal. There is one V965 module for the anode and cathode signals each. The four PMT signals from the LSO detector are recorded in the first four channels of a V965A module. The system has been designed to have one common gate for all three QDC. It has to be assured that the later arriving anode signals fall also within the integration gate. This determines the minimum gate length which is the maximum delay of the anodes t_{delay} and pulse length t_{pulse} . The value of t_{delay} is determined by the detector bias U and the charge transport properties. Using eq. (1.15) and assuming that the anodes are perfectly shielded until the electrons are very close, one gets

$$t_{\text{delay}} = \frac{d^2}{\mu_e U}. \quad (3.3)$$

d is the detector thickness and μ_e the electron mobility. Inserting $U = 500$ V, $d = 0.5$ cm and the numbers from table 1.1, t_{delay} is expected between 500 ns and 625 ns. The chosen gate length was 840 ns which includes the decaying pulses and a margin.

Stretching the gate longer than needed is disadvantageous. Theoretically, the integration result from the baseline in the absence of pulses is zero. However, the QDC sense a finite value which is referred to as *pedestal* which is due to the integration of the *pedestal current*.

This current fluctuates so that in the absence of signals, a peak is measured at the pedestal value with a certain width. The pedestal is an offset to the values returned by the QDC. This has to be corrected for and the distribution has to be chopped off before the pedestal in order not to spoil the data flow with values coming from empty signals.

The pedestal is mostly a property of the electronic QDC channel which has been found out by exchanging detector signals which left the pedestal nearly untouched. Moreover, the value is a function of the module temperature. It increases as the modules warm up. This drift affects also the measured values. Therefore, the following routine was implemented: the VME crate was turned on one hour prior to measurement. After one hour the crate has reached a stable temperature and an empty measurement with false triggers was initiated to record the pedestal of any QDC channel. A peak finding routine was applied to find and correct for the pedestal values per channel.

Bias Supply

The bias to the LSO detector, the CdZnTe cathodes and the grid is supplied by VHQ202M modules by Iseg Spezialelektronik GmbH, Radeberg, Germany. Each module has two channels which can provide up to 2 kV with a maximum ripple of 2 mV_{pp}. There is one module for the bias and grid voltage of the CdZnTe detector and a second module for the supply of the LSO detector. A third module for a second CdZnTe detector is foreseen. The modules can be completely programmed via the VME bus which makes remote measurements convenient.

Crate Layout

Figure 3.12 shows the fully populated crate with the measurement PC and the delay lines. Since all modules fit into a single crate and no more bulky components are required, the camera system is mobile and can be assembled and set to operation in less than one hour.

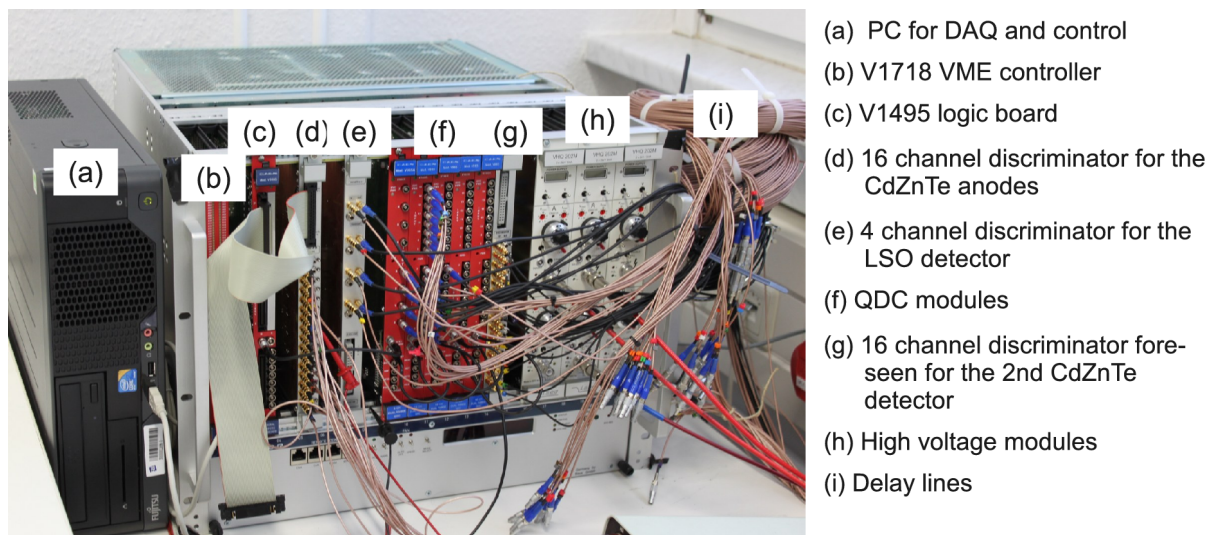


Figure 3.12: The populated VME crate with the measurement PC and delay lines.

Data Transfer and Processing

The VME crate is connected to a measurement PC running Linux via a V1718 VME-USB bridge by CAEN S.p.A., Viareggio, Italy. CAEN provides a Linux kernel driver which required modification and recompilation in order to address the V1718 correctly. CAEN also supplies a software library with functions for reading and writing data from and to specified VME bus addresses. Inserting addresses and data words in hexadecimal format quickly leads to cumbersome and unmanageable code. Due to the complexity of the Compton camera readout, a wrapper interface for convenient module access was implemented. Furthermore, the data acquisition and data processing tasks have to run in parallel in order not to delay the DAQ.

Due to these reasons, the software library *libCVME* was written. Similar to *libCompton*, it builds upon the Root framework. *libCVME* bundles the hardware access and data processing. It is on the one hand designed to have a generic architecture so that different hardware can easily be added for further expansion of the system. On the other hand it provides classes which perform very specific tasks to the Compton camera in its current implementation. Like *libCompton*, *libCVME* in the implementation used for this study is my work with minor contributions from Christian Golnik.

Writing an own DAQ library has been preferred over the option to modify existing solutions for VME readout like the Multi Branch System developed at GSI and in use at the Helmholtz-Zentrum Dresden-Rossendorf because of the very specific tasks to be performed with the data. In retrospective, this was the right decision since the resulting library has been proven to be robust and sufficiently fast. By the time of writing, the code is being in use and further developed for ongoing Compton camera research.

Key design features are the wrapping of VME module access into C++ classes with member functions corresponding to the module features and multi-threaded data processing.

Module access is managed by the `CVME::Controller` class which provides a handle to the V1718 interface. The `Controller` is the only object which may access the VME bus. Additionally, all bus operations are locked with a mutual exclusion lock. The `Controller` also has an address table with VME base addresses and can provide access to modules via the static `Controller::GetModule` (e.g. `GetQDC`) functions. Modules which need bus access are instantiated only once. The `Controller` class always keeps book about bus access. The objects returned by the `GetModule` function all derive from the pure virtual `CVME::Module` class. This parent class contains a VME base address and a pointer to the `Controller` object through which all read and write operations are performed.

The classes inheriting from `Module` declare and implement their own functions for setting parameters on the VME modules (e.g. `QDC::SetLowThreshold`) and for retrieving data (e.g. `QDC::ReadAllData`). The access model is outlined in figure 3.13. The module classes implemented in this application are

- `QDC`: provide access to the QDC modules; setting all parameters and retrieving data from the internal data buffer.
- `VHQ`: access to the VHQ202M high voltage modules; setting voltage parameters and turning the voltage on and off.
- `Logic`: interface to the V1495 logic board; setting the masks (enabling/disabling detectors and channels), setting gate length.

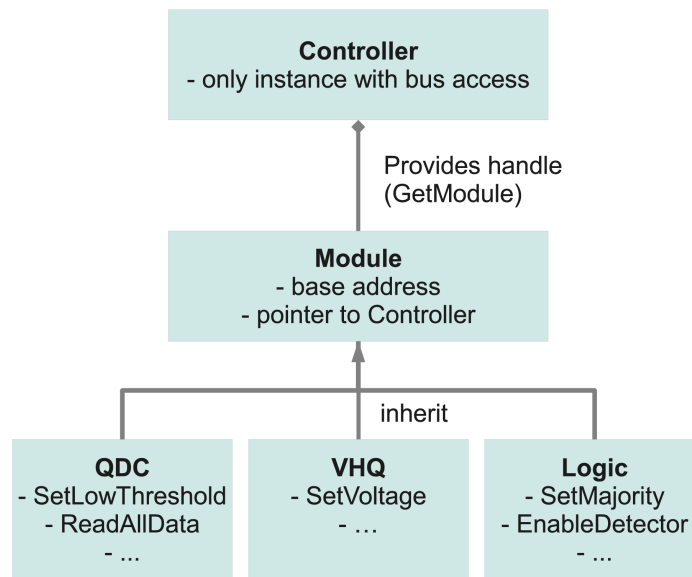


Figure 3.13: Implementation of the interface to VME bus operations in libCVME.

Data readout and processing is organized in threads which pass data on via buffers. The data flow is illustrated in figure 3.14.

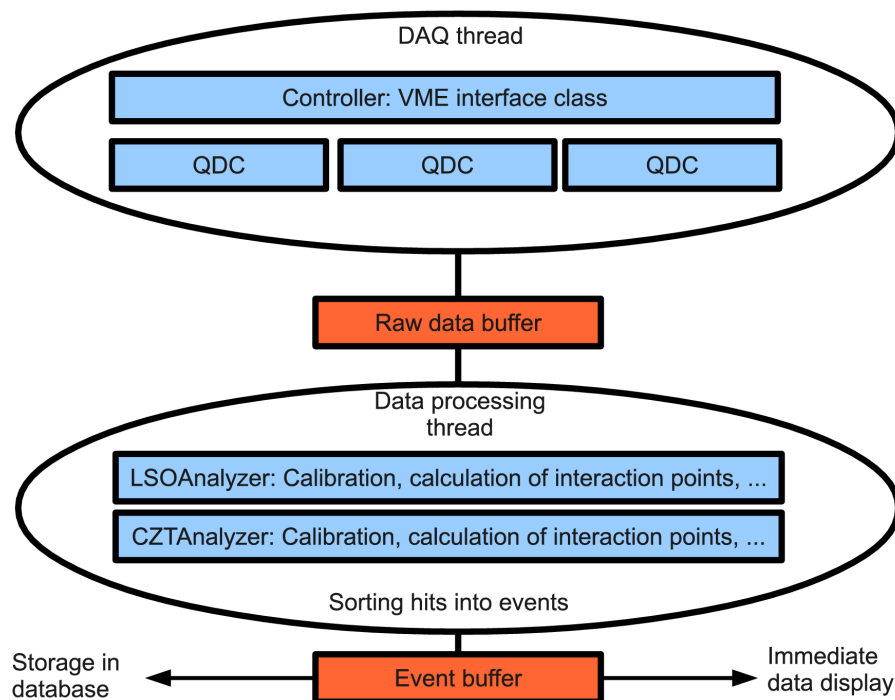


Figure 3.14: Data flow and thread organization in libCVME.

Retrieving the data from the VME system is done by one single thread which does nothing but reading available data from the QDC buffers and writes this raw data to a raw

data buffer. The raw data buffer contains objects of the type `QDC::ValidData` which comprise their origin (trigger number, module number, channel number) and the QDC value.

The raw data has to be processed to `CEvent` objects. A `CEvent` is made of `CHit` objects which contain the following information:

- detector index (CdZnTe or LSO),
- interaction position in x , y and z (if available) and
- deposited energy.

Calculating these information from the raw data is done via a separate thread. Data from the LSO detector is handled by the dedicated class `LSOAnalyzer`, CdZnTe data is processed by `CZTAnalyzer`. These classes have access to calibration information which have been saved prior to measurements.

The `LSOAnalyzer` performs the following:

- Correct for the pedestal,
- correct for the PMT gain,
- convert total signal sum to deposited energy with a linear calibration function and
- identify the fired pixel according to the procedure explained in section 3.2.2.

The `CZTAnalyzer` does these calculations:

- Correct for the pedestal,
- calibrate the channel values to deposited energy with linear calibration functions,
- calculate the energy-weighted interaction position and
- estimate the depth-of-interaction via eq. (1.23).

The most time consuming task of the data processing thread is however to sort the hits into events. The raw data contains a trigger number assigned by the QDC modules which counts the gates. This number allows identification of hits that belong together.

After the event has been assembled, it is fed into an event buffer. Different threads can register to have access to the data in this buffer. The buffer model makes sure that all registered data sinks receive the same data. Data is removed from the buffer after it has been sent to all receivers. From here, it is possible to send the data to the Compton Camera Imaging Database (CCIDB). CCIDB and its access functions have been written by Sebastian Schöne, Helmholtz-Zentrum Dresden-Rossendorf. It provides a fast buffered data transfer into a PostgreSQL database which can be accessed by the image reconstruction algorithms. Reconstruction results are also managed within this database.

Event data can also be processed by a graphical data display thread which offers the immediate inspection of gathered data during a measurement. It provides also a graphical interface which allows to start and stop measurements. Since it runs within a separate thread, it does not interfere with the DAQ thread on a multi-core computer. A screenshot of displayed elements during a measurement is shown in figure 3.15. In the upper left, control elements for starting and stopping the DAQ thread, the database access thread and the immediate data display are shown. There are also buttons for saving the displayed histograms and for simulating data for debugging purpose. The green timer shows the measure-

ment time. In the lower left, the control elements for the high voltage modules are shown. The other three windows hold histogram data of the whole event (upper right), the CdZnTe detector (middle right) and the LSO detector (lower right). In the background, the console output is shown which displays error messages and the connection state.

libCVME builds upon the Root framework. This allows to start measurements script controlled. Parameters are set within a Root script which at the end starts the interface shown above.

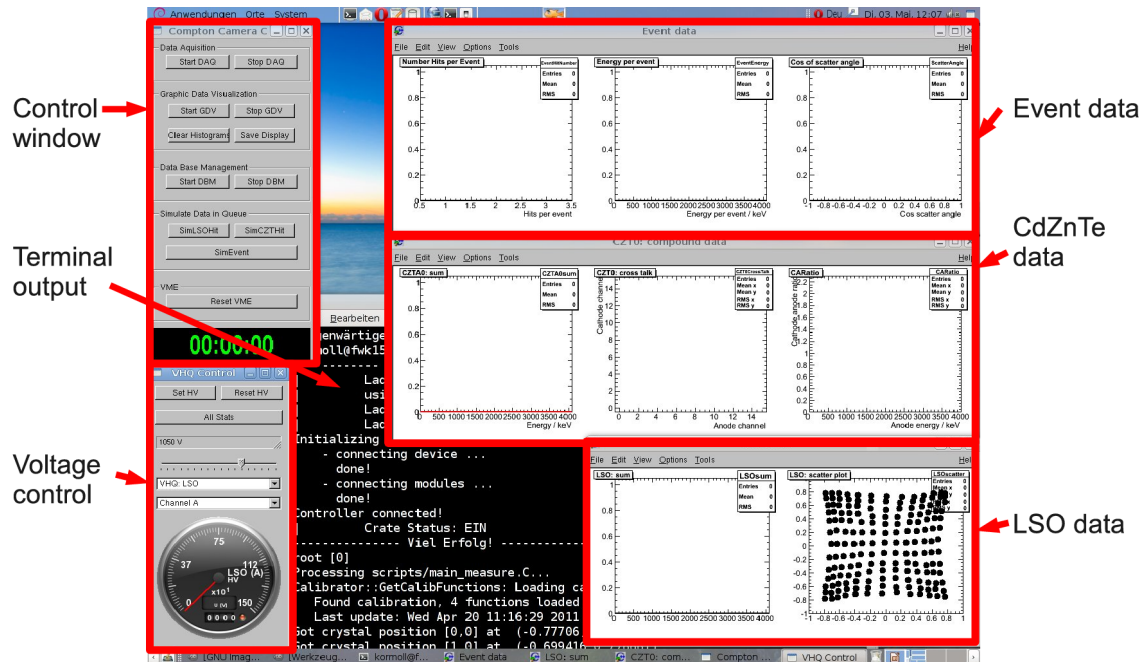


Figure 3.15: Elements for measurement control and data inspection during a measurement.

3.3 Results

The presentation of measurement results is divided into two parts. The first part in section 3.3.1 concerns itself with the characteristics of the two components CdZnTe detector and LSO detector.

In section 3.3.2, the total performance of the system in coincidence mode is shown. These are primarily imaging results from point source measurements.

3.3.1 Detector Performance

All experiments presented in this section were conducted using a ^{22}Na point source with 900 kBq activity. ^{22}Na emits one positron per decay and one photon with 1275 keV. The positron annihilates close to the source so that two opposing photons with 511 keV and the one γ -particle at 1275 keV leave the source.

Pedestal Alignment

Prior to measurements, the VME crate has to warm up to operational temperature and the QDC channels have to be aligned as described in 3.2.4. The trigger logic is set to accept events from each one of the LSO channels to produce a gate signal. Due to the natural radioactivity of LSO, this results in numerous events without pulses present on the CdZnTe detector. This is even suitable to align the LSO channels since a signal in one channel is not necessarily registered on another channel due to the small energy deposition of many events.

Figure 3.16 shows the raw data from eight randomly selected CdZnTe anode channels. These curves are representative to illustrate the mean variation among the channels and the width. The pedestal value is mostly in the range of several hundred channels. On the scale of 4096 available ADC channels this is considerable and even the variation around 100 channels is not negligible. This illustrates why channel alignment in these QDC modules is mandatory.

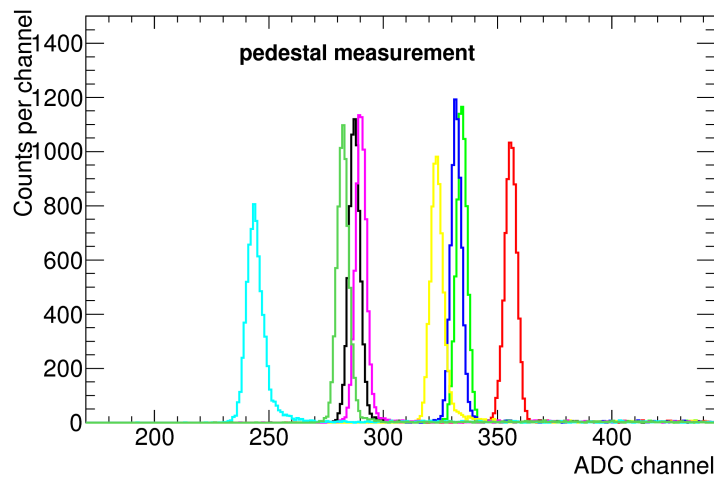


Figure 3.16: Pedestal measurement for QDC channel alignment.

CdZnTe Detector

In figure 3.17, two typical pulses from the NSP output at the anode and at the cathode are shown. The bias was set to -500 V which corresponds to an electric field of -1000 V/cm. The grid voltage on the detector was set to -100 V.

The anode pulses have a rise time of about 30 ns. Varying the grid voltage has no obvious effect on this number. The energy resolution does also not strongly depend on the grid voltage in this detector. Since the overall energy resolution is as expected (see below), no additional effort was undertaken to modify the voltage parameters.

In figure 3.18 the pulse height spectrum of a single anode channel linearly calibrated to energy deposition is shown. One can clearly see the lines at 511 keV and 1275 keV with their respective Compton edges. There is hardly any low energy tailing apparent around the peaks. This indicates that there is negligible electron trapping and/or that the condition of eq. (1.22) is fulfilled. Methods to compensate for electron trapping have therefore not been implemented.

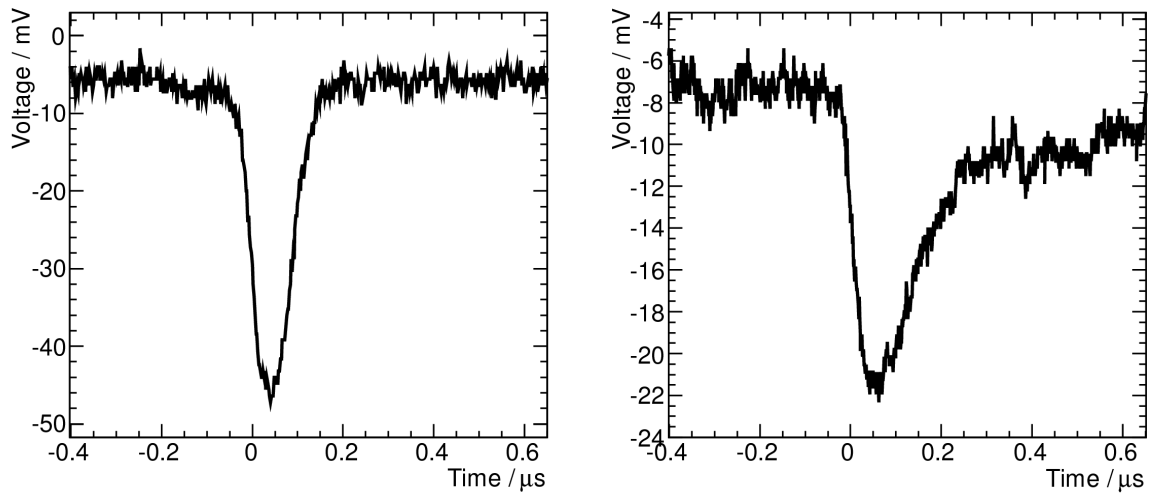


Figure 3.17: Typical pulse shapes from the CdZnTe detector. Left: anode, right: cathode.

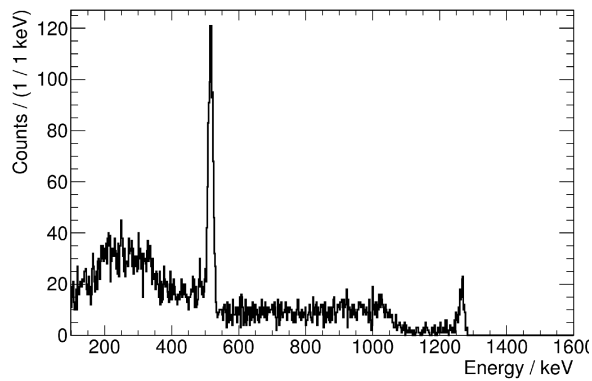


Figure 3.18: Single anode pulse height spectrum from the CdZnTe detector.

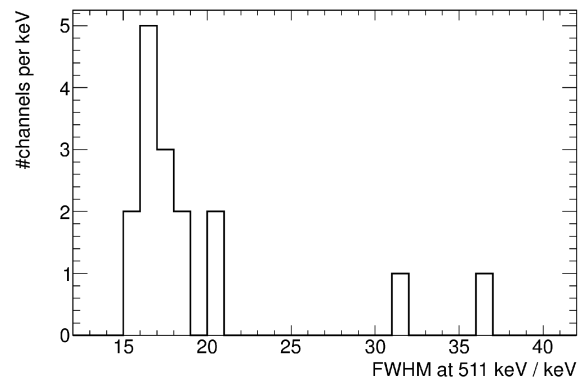


Figure 3.19: Distribution of the FWHM at 511 keV among the anode channels.

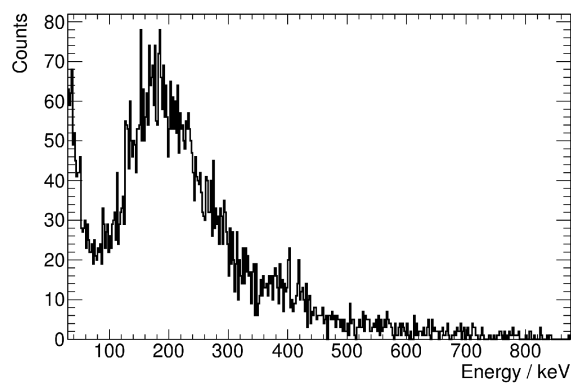


Figure 3.20: Single cathode pulse height spectrum.

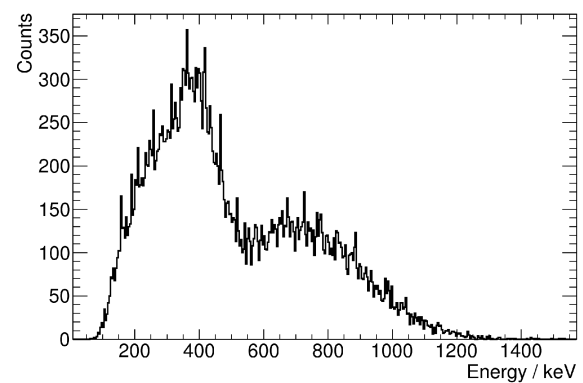


Figure 3.21: Spectrum of the sum of all cathode signals per trigger.

The FWHM of the 511 keV peak has been determined for all anode channels. The distribution of the width is shown in figure 3.19. There are two outliers with worse resolution.

3.3 RESULTS

Their resolution is dominated by preamplifier characteristics. Mounting the same NSP boards to different anode channels yields a similar resolution than the same preamplifier has shown before. The mean value disregarding the two outliers is 17 keV which corresponds to a resolution $R = \text{FWHM} / E$ of 3.3 %.

A signal height spectrum from one single cathode channel is plotted in figure 3.20. The drop in counts per channel on the lower end is caused by the threshold of the LE-trigger. There is no structure on the spectrum that reveals the peaks at 511 keV and 1275 keV. However, when plotting the sum of all cathode channels per event, a structure is unveiled that can be correlated to deposited energy. This has been done in figure 3.21. This is no effect of statistics. Even very long measurement time does hardly improve the picture in figure 3.20.

The reason why there is no apparent structure on the single cathode spectra is that there is no charge focusing the cathode strips. Due to the weighting potential, the charge is steered towards the anode strips which lead to complete charge collection on the anode side in most cases. There is no such steering momentum for the cathodes. The sum of all cathodes however sense the whole charge which is geometrically available.

A scatter plot of the energy-weighted anode and cathode channels illustrates this difference in charge collection intuitively. Figure 3.22 shows such a plot. In the anode dimension, most events fall directly on a channel number, which means that the whole charge is collected on a single anode. In the cathode dimension, the charge is evenly distributed along the entire range.

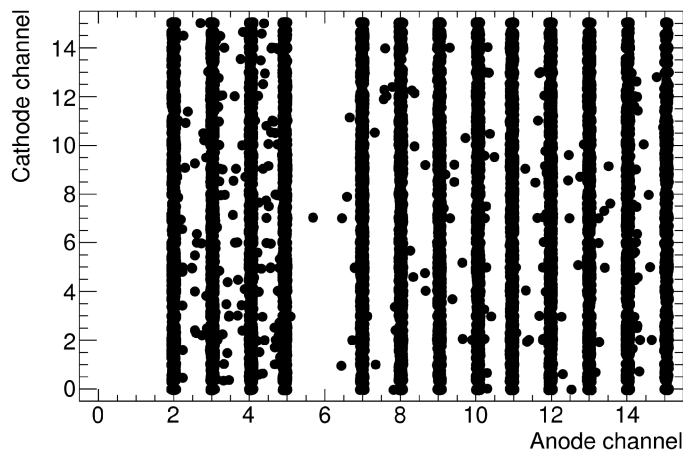


Figure 3.22: Scatter plot of the energy-weighted anode and cathode channel. The anodes 0, 1 and 6 were turned off during this measurement.

There is however considerable charge loss in the cathode signal depending on the interaction depth, c.f. equation (1.21). The maximal signal height occurs when the interaction is close to the cathode and the full energy of 1275 keV is deposited. The full deposition of 511 keV near the cathode causes the maximal possible signal due to the 511 keV line. These two endpoints can be seen in figure 3.21. The energy calibration has been done with respect to these points.

The procedure is not ideal since the endpoints are not as easy to determine like the peak position in the anode spectra. This leads to uncertainties in the depth-of-interaction measurement where the cathode signal relative to the anode signal is needed.

In figure 3.23 the cathode-to-anode signal ratio (C/A) is plotted over the deposited energy. The full energy line at 511 keV is clearly visible. Also the 1275 keV line comes out clearly, although a slight misalignment of the various anode channels causes this line to widen. Most of the entries fall within a C/A of 0.4 to 1.2. At lower energies, even higher C/A values occur. According to eq. (1.23) C/A is expected to be within the range from 0 to 1.

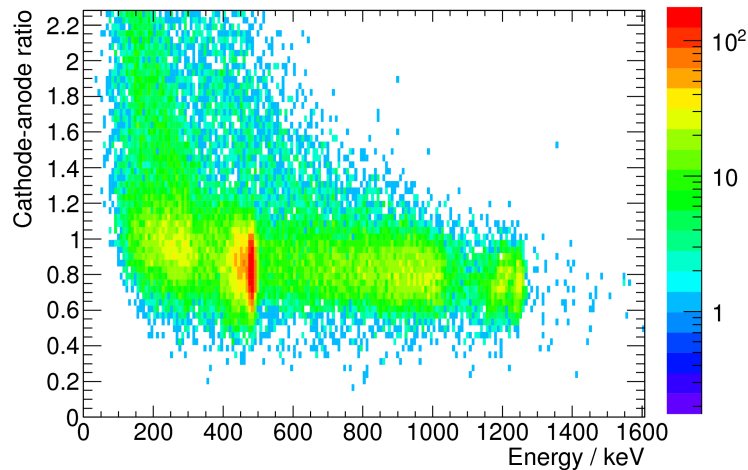


Figure 3.23: Cathode-to-anode ratio over the energy measured on the anode. The color scale indicates the number of entries per bin and is logarithmic.

There are various reasons for the observed structure and the deviation of C/A from the expected range. Events with $C/A = 1$ are expected to happen at the cathode with complete charge collection on the anodes. Incomplete charge collection on the anode would result in higher C/A values. However, the anode measured energy is not less for the high C/A events. This is consistent with the observation that there is no considerable electron loss in the anode spectra.

The following two reasons are considered to cause the observed C/A behavior:

- (1) The system uses the value of a single cathode channel for trigger generation. This causes events with low C/A or, when the charge is shared among several cathodes so that the individual signal is lower, to be registered with less sensitivity. This explains partly the lack of events below $C/A = 0.4$.
- (2) The cathode energy calibration is affected by uncertainties. As mentioned above, the sum spectrum is calibrated to the endpoints of full-energy depositions. No energy calibration of the individual cathode channels is possible due to the charge sharing. Although the crystal seems to be homogeneous, there might be minor differences among the cathode channel sensitivity due to minor variations among the gain of the NSP. This might affect the reliability of the cathode sum signals.

There are two ways of treating the depth-of-interaction determination: tuning the cathode calibration to fit the major part of the events in figure 3.23 into the range of $C/A = 0 \dots 1$, or mapping the depth to the observed C/A ratios. The second approach was taken in this work. Due to the preamplifier mounting and the casing, the setup does not allow the detector to be scanned with a pencil beam from the side to achieve a depth calibration. One has to keep in mind that the detector volume near the anode is less sensitive due to the trigger pattern which is sensitive to the cathode signal height and that the acquired depth information are

3.3 RESULTS

not as reliable as it would be desirable. The depth values are therefore only considered to be estimates.

LSO Detector

The typical pulse shape of an output of one of the four PMT of the LSO block-detector is shown in figure 3.24. The rise time is around 10 ns. The oscillation on the tail does not influence the measured energy values since it is leveled out in integration in the QDC.

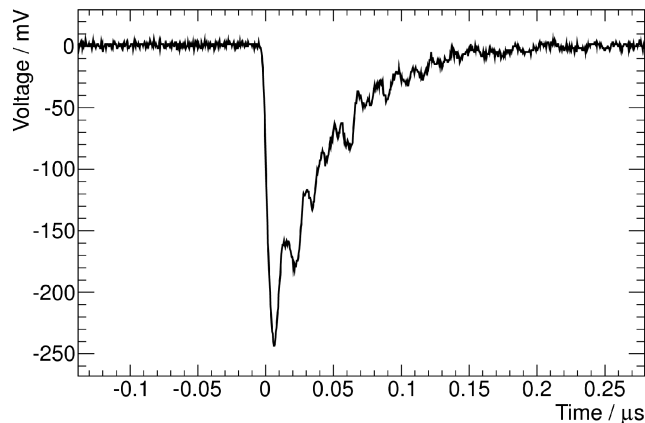


Figure 3.24: Typical pulse shape of one of the four PMT from the LSO block-detector.

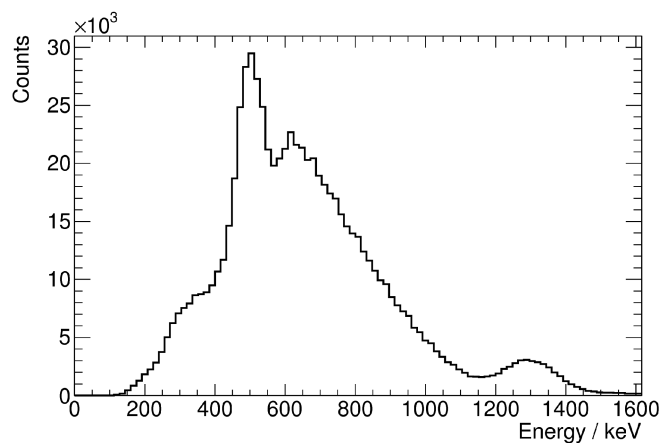


Figure 3.25: LSO sum spectrum from a ^{22}Na measurement.

The sum spectrum of the LSO detector calibrated to energy is shown in figure 3.25. The full energy peaks at 511 keV and 1275 keV clearly appear. The background caused by the β -decay of ^{176}Lu with a Q value of 1193 keV is significant. The FWHM at 511 keV is 94 keV which corresponds to a resolution R of 18.5 %. This spectrum is recorded with gain adjustment of the PMT.

The gain has been determined with the help of the interaction map which shows the hit coordinates (x, y) according to equation (3.2). The map is shown in figure 3.26 without gain adjustment, i.e. $g_i = 1$ for all PMT. One can identify all 169 pixels in the map. It also appears to be symmetric at a first glance what indicates that there is no major inhomogeneity in the

gain factors. If all PMT and crystals were homogeneous, the peaks from the pixels which are situated half way along the edges would appear at $x = 0$ or $y = 0$, respectively. Their displacement in figure 3.26 is used to calculate the gain factors. If y_a is the displacement in the map of the pixel at the center of the left edge, the gain factor of the PMT of channel 1 is $g_1 = 1 - y_a$. Similarly, one gets $g_2 = 1 + x_a$ (x_a : displacement of the center pixel on the upper edge) and $g_3 = 1 + x_a - y_b$ (y_b : displacement of the center pixel on the right edge). The resulting gain factors are $g_0 = 1$, $g_1 = 0.99$, $g_2 = 0.92$ and $g_3 = 0.91$. The corrected interaction map is shown in figure 3.27. The difference is only subtle since the g_i are all close to unity. The map is not entirely symmetric because the different light yields of the crystals have not been corrected. Nevertheless, there is a slight improvement in the edges. Here, the rectification leads to better differentiability of the pixels.

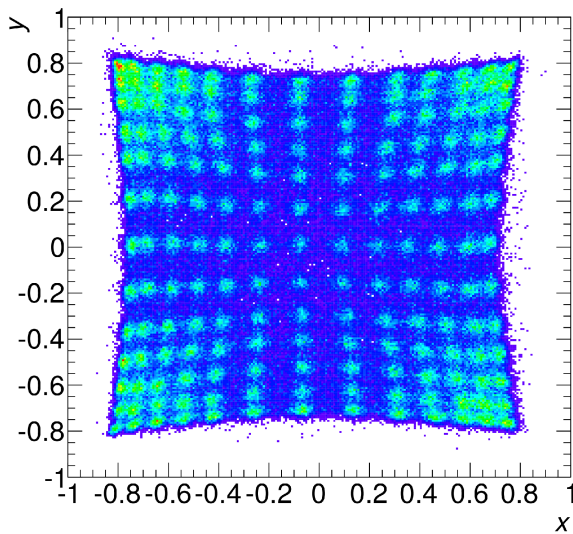


Figure 3.26: LSO interaction map without gain adjustment.

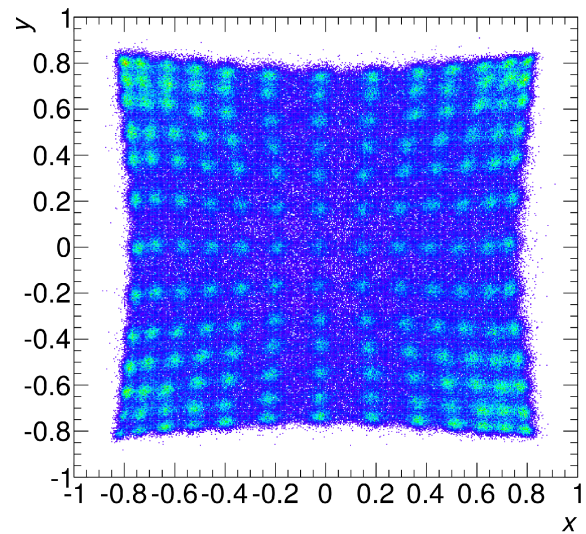


Figure 3.27: LSO interaction with gain adjustment.

3.3.2 System Performance

For imaging tests, the ^{22}Na point source has been placed at 7 cm distance from the CdZnTe layer. From an irradiated target, a background of 511 keV from β^+ -emitters and prompt γ -rays are expected. The radiation field from a ^{22}Na source resembles this case. However, the energy of 1275 keV is considerably lower than 2.2 MeV which is expected to be the least energetic prominent γ -ray in beam experiments. Using the 1275 keV γ -rays for imaging with the background of 511 keV photons has been chosen as the laboratory scenario to test the imaging capabilities of the camera system.

An image requires several hundred valid events. It took 10 minutes to reach 900 such events. This gives an estimated efficiency for true events around 10^{-4} .

The camera layers were set to a distance of 3.5 cm. The trigger control was set to accept events if there was a hit in the CdZnTe or the LSO detector. However, only events with an energy deposition in both detectors were sent to the database. This trigger pattern is more sensitive than setting the logic to read data if both the LE-discriminator of the CdZnTe and

3.3 RESULTS

the LSO detector have triggered. Low energy deposition might not be sufficient to trigger the LE-discriminator, but may be registered in the QDC, especially when charge is shared among several cathodes in the CdZnTe detector.

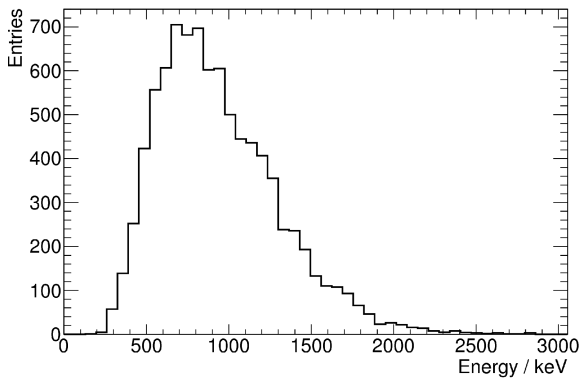


Figure 3.28: Total event energy (CdZnTe + LSO) in a ^{22}Na measurement.

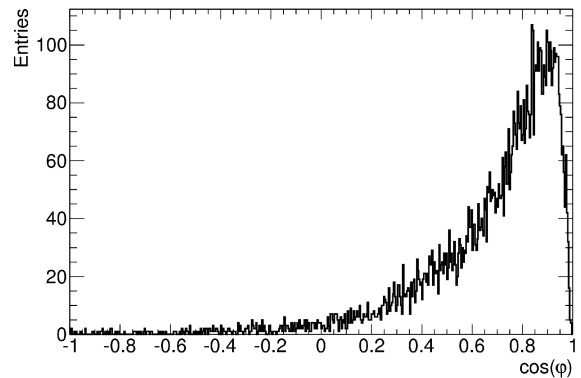


Figure 3.29: Cosine of the measured scattering angle corresponding to the events in figure 3.28.

If the only restriction to the data is that the deposited energies in the two detectors must yield a valid scattering angle, i.e. $\cos \varphi \leq 1$, the resulting spectrum of the total deposited energy is shown in figure 3.28. The distribution of $\cos \varphi$ is shown in figure 3.29.

The angular distribution shows that most events are forward scattered events with very few events with scattering angles larger than 90 degree ($\cos \varphi < 0$).

In the energy spectrum, there is no peak structure at 511 keV or 1275 keV. Instead, it is a continuous distribution which reaches its peak value around 700 keV. There is some structure in form of a steeper decrease above 1275 keV which might be the indication for some events with the total energy deposition of this γ -line which sits on top of a continuous background of false coincidences. The background is however very pronounced. Since a measured energy which is not around 1275 keV (or 511 keV) cannot yield correct scattering angles and thereby valid cones for image reconstruction, the raw events cannot be used for reconstruction without further filtering.

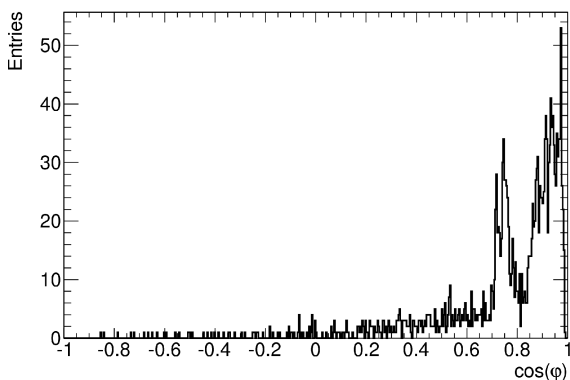


Figure 3.30: Cosine of the scattering angle for events with a total energy around 1275 keV.

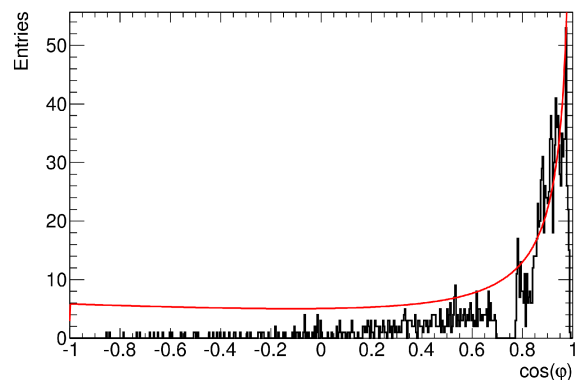


Figure 3.31: The same data as in figure 3.30 without energy depositions in the CdZnTe detector around 511 keV. In red: incoherent scattering cross section of 1275 keV.

When accepting only events with a measured total energy of $1275 \text{ keV} \pm 130 \text{ keV}$, the resulting distribution of $\cos \varphi$ is plotted in figure 3.30. Forward scattering is more pronounced than in figure 3.29. However, there is a peak at a value of 0.75 which seemingly is an unwanted effect. Cutting out the data which have an energy deposition of $511 \text{ keV} \pm 30 \text{ keV}$ in the CdZnTe detector removes this structure (figure 3.31). However, also valid events in this region are cut out so that a hole is left in the distribution. Thus, the peak was caused by the absorption of 511 keV photons in the CdZnTe detector. In the LSO detector, the values of $\cos \varphi$ and the energy deposition in the CdZnTe detector correspond to an energy deposition of 785 keV. In this range, many events occur in the LSO due to its natural radioactivity (c.f. figure 3.25). The structure in figure 3.30 is therefore caused by random coincidences. In figure 3.31, the cross section for incoherent scattering at 1275 keV in CdZnTe is plotted in red over the data. The curve was approximately scaled to fit the data in the forward scattering regime. It can be seen that the distribution follows the form of the curve. This is an indication, that the applied event filter separates relevant data.

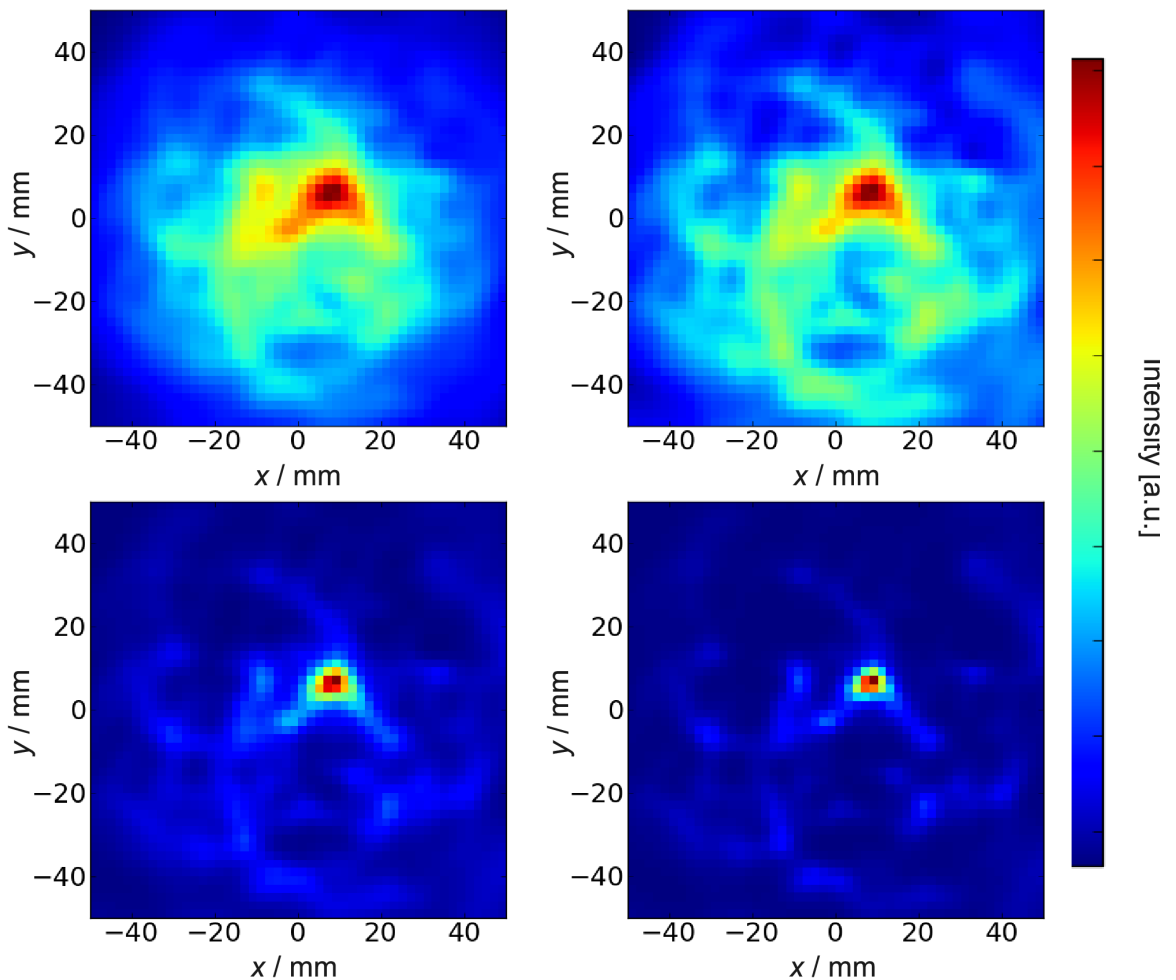


Figure 3.32: Image reconstruction of a ^{22}Na point source. Upper left: backprojection, upper right: first iteration ML-EM, lower left: fifth iteration ML-EM, lower right: tenth iteration ML-EM. 900 events were used for the image reconstruction.

3.3 RESULTS

The application of the energy filter requires knowledge of the expected γ -ray energy. This knowledge can be further exploited by fixing the total energy to this value which further reduces uncertainties in the scatter angle calculation. In this setup, the scatter detector has a much better energy resolution than the absorber. Therefore, the energy information from the LSO was only used to select what event fall into the given energy window. The scatter angle was calculated with the assumed total γ -ray energy and the measured energy deposition in the CdZnTe detector only.

The filter on the total energy was the only criterion which was able to separate valid data from background. The requirement to know or at least guess the incident energy influences the measurement strategy. This is discussed at the end of this section.

In figure 3.32, reconstructed images with an energy window $1275 \text{ keV} \pm 130 \text{ keV}$ are shown. The source is situated at $(x, y, z) = (10 \text{ mm}, 10 \text{ mm}, 0)$. In this coordinate system, the z direction points from the origin to the camera position. Shown are slices through the three-dimensionally reconstructed image at $z = 0$, i.e. at the distance of the source to the camera. The simple backprojection algorithm is compared to the image after different numbers of iterations in the ML-EM algorithm.

The center of gravity in the summed backprojection already reflects the actual source position very well. There is however a significant reduction in image background when moving to the advanced ML-EM algorithm. After ten iterations, the source very clearly stands out from the rest of the image. This illustrates how well the ML-EM reconstruction is suitable for identifying point-sources.

In figure 3.33, slices of 4 mm width along the x and y direction through the image after the tenth iteration are shown. The slices run through the source position. The FWHM of the profiles is 5.9 mm in x direction and 5.6 mm in y direction.

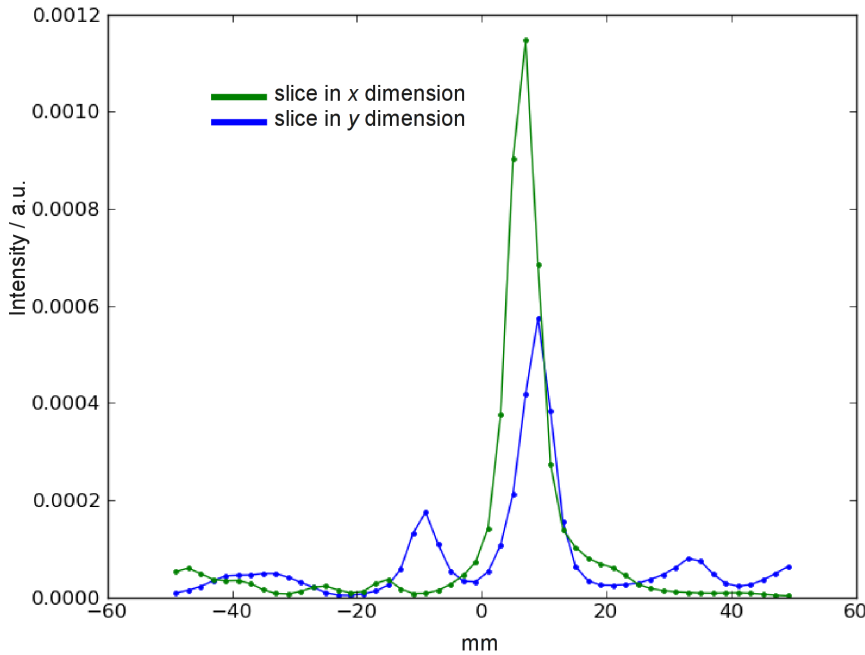


Figure 3.33: Slices through the tenth iteration reconstruction of a point source measurement at the source distance.

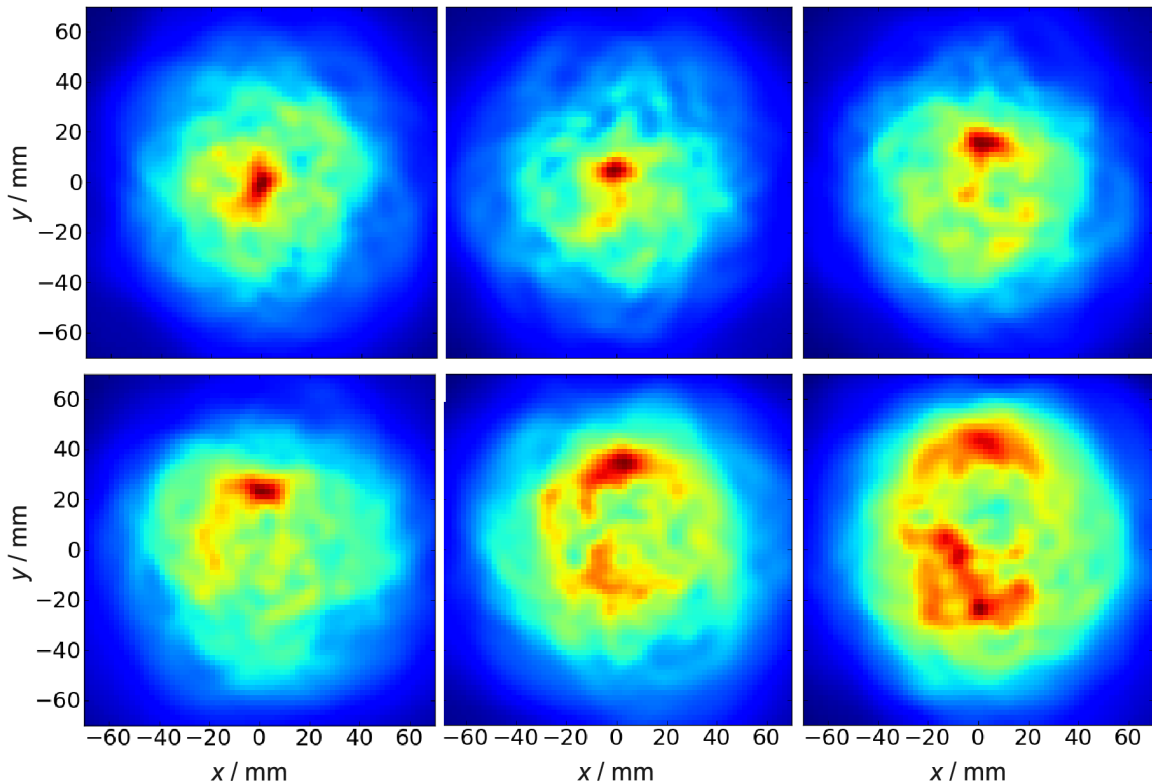


Figure 3.34: Reconstructed images of a point source at different positions, first iteration ML-EM.

To study the imaging performance for sources which are not in the center of the field of view, the point source has been moved in steps of 10 mm from the center at $(0, 0, 0)$ upward to $(0, 50 \text{ mm}, 0)$. The results after the first iteration of the ML-EM algorithm with the same energy filter as explained above are shown in figure 3.34. In the upper row of images, the source starts left at the center and is moved to $y = 20 \text{ mm}$ in the upper right image. In the lower row, the source is further moved from $y = 30 \text{ mm}$ on the left side to $y = 50 \text{ mm}$ in the lower right image. Each image contains around 900 events.

The maximum intensity in the reconstructed images again reflects nicely the actual source position. At $y = 40 \text{ mm}$ and $y = 50 \text{ mm}$ there appear areas with high intensity mirrored on the $y = 0$ line in the area with negative y . This effect is caused by the cones which form the image. In the shown slice at $z = 0$, the cones show up as ellipses. These ellipses come close to each other and overlap at the actual source position but also opposite to it. This is only observed at large displacements compared to the detector dimensions.

The same data is shown in figure 3.35 after five iterations. ML-EM is capable to reduce the image of the “mirror source” significantly. However, the spatial resolution remains best in the center of the field of view. The source appears elongated in the x direction, i.e. along the ellipses forming the image.

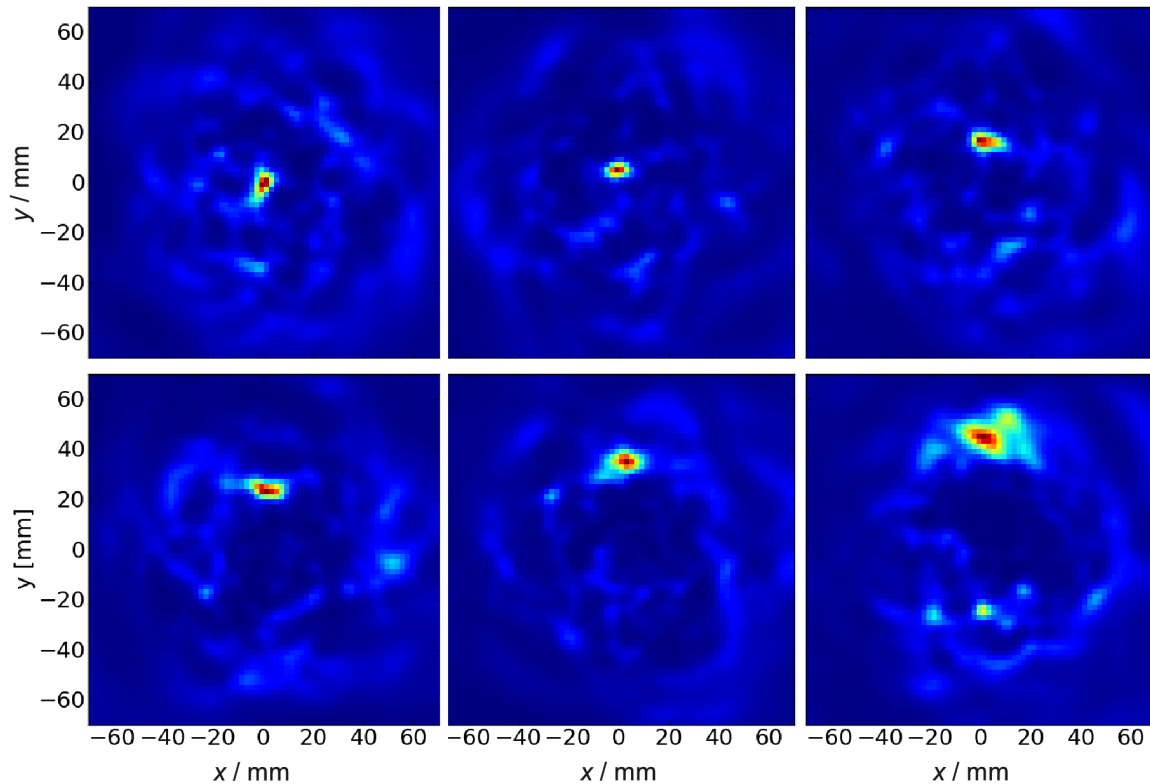


Figure 3.35: The same data as in figure 3.34 after five iterations.

3.4 Conclusions

The CdZnTe detector performs sufficiently in this evaluation system. Very clear energy spectra are recorded from the anode signals and the energy resolution is comparable to that of similar systems (e.g. [Gu11]). This indicates that the chosen electrode layout is a good match for the detector material. The preamplifiers together with the QDC readout on the anode side also deliver signals of good quality. Besides the temperature dependent pedestal, the readout chain works fast and reliable.

The segmented readout of the cathodes works not as flawlessly as the anode readout. The cathode signals are small and rise not as quickly as the anode signals. They appear however first and are therefore required for trigger generation. The charge sharing on the cathode can be exploited for more precise hit localization in the cathode dimension, but it is problematic at the trigger generation stage. This effect also avoids clear single channel spectra to be measured which would allow a better channel alignment.

It has been tried to feed the analogue output of the cathode NSP into an analogue adder whose sum output was fed into the LE discriminator. However, adding the signals after the preamplification stage also adds the noise. The signal is usually shared by not more than two channels. The noise however is added from all 16 channels, which reduces the signal to noise ratio in the analogue sum by a factor of eight compared to the signal to noise ratio of

a single channel. What finally made this solution unfeasible was the occurrence of a coherent interference present on all channels. It was hardly visible on a single channel but was considerably amplified in the analogue sum.

In conclusion, the segmented cathode readout is problematic and prevents a reliable depth-of-interaction determination via the cathode-to-anode ratio. A pixel detector with a continuous cathode avoids these problems for the price of a high channel number. An intermediate solution is a design with the same anode layout but with wider cathode strips. This sacrifices some spatial resolution but increases the cathode pulse height and reduces the charge sharing.

The LSO detector provides sufficient performance to be suitable for this project. Since its energy information is only used to select suitable events for image reconstruction, but not for the calculation of the scattering angle, there would be very limited gain in the current implementation of better energy resolution. This requires however, that the γ -lines to be measured can be separated by the energy information from the LSO detector. This is however the case in this application and is also expected in beam experiments.

The LSO detector is larger than the CdZnTe detector what increases the efficiency of the system. However, the natural radioactivity leads to many triggers from the large LSO. The CdZnTe detector is less efficient due to its smaller size and the event loss due to the cathode problem. This inhomogeneity in the system leads to false coincidences on the trigger level. Nevertheless, the data processing is able to filter out valid events by the energy criterion and the condition of a valid cosine of the scattering angle. A detector with no intrinsic radioactivity would be preferable since it would reduce the load on the DAQ system. In this implementation it was however not observed that the data rate limits the count rate.

With all imperfections, the constructed system is able to produce images of a point source with a resolution below 6 mm FWHM at 7 cm distance. This however is only achieved with iterative image reconstruction algorithms. Simpler algorithms result in images with the right center of gravity with a very extended intensity. It is not feasible to compare the spatial resolution to the angular resolution measure from chapter 2 since the angular resolution depends strongly on the image reconstruction.

The system lacks the ability to record events with more than two interactions. It was however found that starting with the simpler technique of scatter-absorber events only is in this first stage sufficient to develop a solid base for Compton imaging in the radiotherapy context. Since all infrastructure is foreseen to extend the system, the advanced imaging method can be implemented at a later time.

Judging from the source measurements in the laboratory, the designed Compton camera is capable to record emission scenes with a reasonable accuracy, even if the source position extends well beyond the dimensions of the small scatter detector. Therefore, from the evaluation possible at the laboratory, the system is expected to show the feasibility of prompt γ -imaging in a phantom experiment.

4 Beam Experiments

With a fully functional Compton camera at hand, the next step is to evaluate the Compton camera technology in a phantom experiment at a proton beam line. The aim is to show the principle feasibility of the technique of prompt γ -imaging with this device under conditions that resemble the clinical application. The proof of principle would be successful if it is possible to correlate the intensity in recorded images to the position of the proton beam or, ultimately, determine the Bragg peak position. In case this is not successful, the experiments are expected to derive further demands on a Compton camera to be applicable under beam conditions.

4.1 Introduction

The most common proton accelerators in radiotherapy are cyclotron machines. To have a beam structure comparable to that which is expected in medical treatment, the beam experiments should also be conducted at a cyclotron.

The AGOR (Accélérateur Groningen-Orsay) accelerator situated at the KVI (Kernfysisch Versneller Instituut) in Groningen, the Netherlands, is a superconducting cyclotron which is able to produce proton beams with primary energies of 90 MeV, 150 MeV and 190 MeV [AGOR]. The RF system of AGOR operates between 24 MHz and 62 MHz.

The experiments were set up at the AGORFIRM beam line (AGOR Facility for Irradiation of Materials) at KVI [Gra09]. The energy of the proton beam was fixed to 150 MeV and current was varied from 5 pA to 200 pA. The highest frequency is applied for the 190 MeV proton beam. At 150 MeV, the frequency is somewhat lower than that*. The accelerator was set up to produce a pencil beam with lowest possible divergence. The beam pipe was extended to reach close to the target so that the beam travels only a few centimeter through air to keep the beam focused. A well concentrated beam results in a small volume in the phantom from which prompt γ -rays are emitted. A small γ -ray emitting volume is expected to be easier to identify in front of the background in reconstructed images than a more extended volume.

*) Private Communication Harry Kiewiet, KVI Groningen, November 2012.

4.2 Materials and Methods

The irradiation bunker of the AGORFIRM beam line features all needed infrastructure for remote measurements. There is an Ethernet connection available to remotely control the measurement PC and coaxial cables are provided between the bunker and the control room for direct access to signals during the irradiation. The complete measurement setup including the camera itself, the VME electronics and the measurement PC was placed inside the bunker. The PC is probably the least radiation hard component since it incorporates the most dense integrated circuitry. It was therefore placed a few meters beam up from the phantom. Neutrons emitted from the phantom are expected to be directed beam downwards. Therefore, the lowest neutron dose is expected beam up from the target.

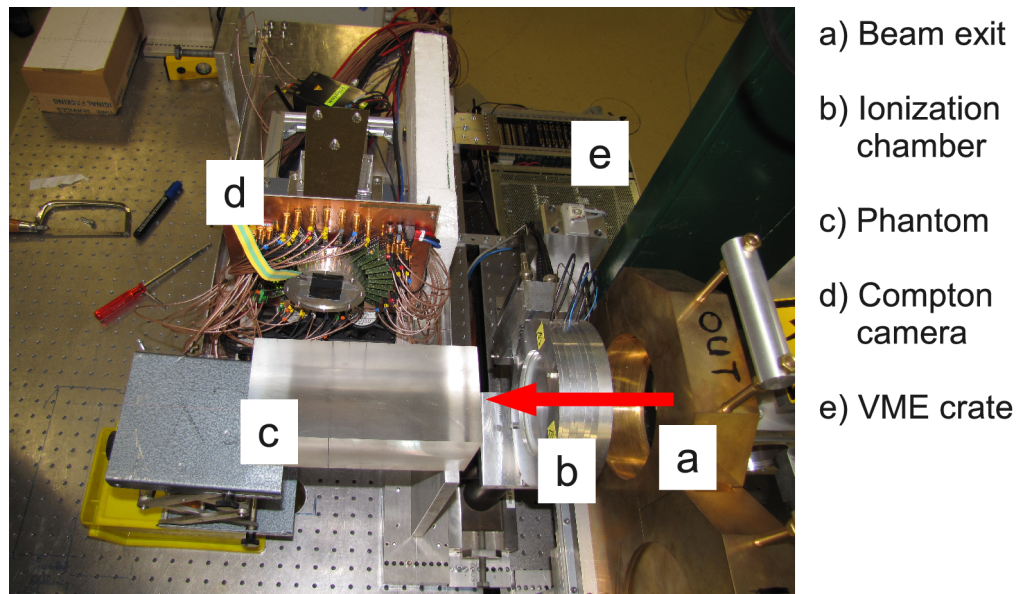


Figure 4.1: The setup at the AGORFIRM beam line. The beam direction is indicated with a red arrow.

The setup in the AGORFIRM bunker is shown in figure 4.1. The proton beam exits the evacuated beam pipe in the lower right part of the picture. For monitoring the beam current, an ionization chamber is in place at the beam exit. After less than 10 cm of air, it hits the phantom whose position is adjusted with the help of the room laser system. The center of the Compton camera detectors is at the same height as the beam. The distance to the phantom surface is 7.4 cm. The coordinate system in these experiments has its origin at the entry point of the beam into the phantom. The x direction points in beam direction and the z direction towards the camera. The VME crate is placed on the floor approximately 1.7 m below the beam. The measurement PC stands right to the crate and is not shown in this image.

In these experiments, simple phantoms have been used which are cuboids with a quadratic cross-sectional area of 10 cm \times 10 cm. The length was 30 cm. In most experiments, the beam was centered on the cross-sectional area. Most experiments were conducted using polyethylene (PE) phantoms. The chemical formula for PE is $(C_2H_4)_n$. There are many protons and no oxygen so that a prominent γ -ray line at 2.2 MeV is expected and no signal at the oxygen de-excitation energy of 4.4 MeV which could spoil the signal at lower energies.

At 150 MeV, the proton beam penetrates 14.8 cm into PE. At this distance, the camera was centered in most experiments.

Before imaging experiments were conducted, the trigger rate in dependence of the beam current was measured in order to choose an appropriate current that allows a decent event rate without overloading the detectors. For this purpose, the gate signal was carried out after the last QDC in the gate chain with a coaxial cable to a 874 Timer/Counter by ORTEC, Oak Ridge, Tennessee, USA.

Prior to beam experiments, the camera was tested with a ^{60}Co source with 700 kBq activity. The source was taped on the phantom surface in a distance of 7.4 cm to the CdZnTe detector. ^{60}Co is a β^- -emitting nuclide whose decay is accompanied by two γ -rays with 1173 keV and 1333 keV.

4.3 Results

4.3.1 Source Test

The imaging results of the source measurements are shown in figure 4.2. The source was located at $(x, y, z) = (150 \text{ mm}, -10 \text{ mm}, 50 \text{ mm})$. The shown slice is taken at $z = 50 \text{ mm}$. The energy selection criterion was applied with

- a window of $(1170 \pm 60) \text{ keV}$ and fixed energy of 1170 keV (left image),
- a window of $(1330 \pm 65) \text{ keV}$ and fixed energy of 1330 keV (middle image) and
- both windows with the respective fixed energy (right image).

The shown images are the results from ten iterations and contain 3776 events in the total image which are nearly equally shared among the lower energy window and the upper energy window.

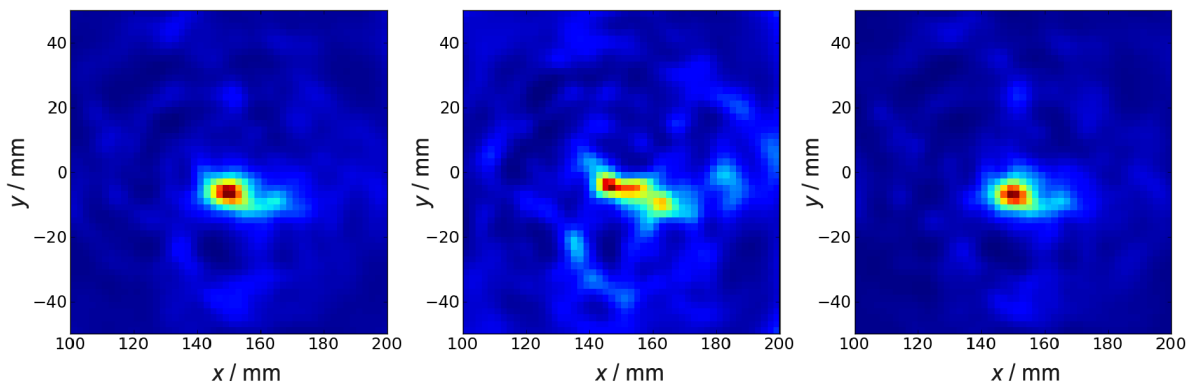


Figure 4.2: Reconstructed images of a ^{60}Co source taped on the phantom.

The image of the source appears larger than the laboratory measurement of the ^{22}Na source. The FWHM is approximately 10 mm. Especially in the middle image the source is elongated in x direction. However, the source position below the $y = 0$ line is reproduced very nicely. There is no information on the actual size of the activity in the source. Hence, it

is possible that the recorded images reflect the real activity distribution. The camera is therefore considered to be operational.

4.3.2 Beam Profile

The beam profile was analyzed with radiochromic film which shows a dark stain when exposed to ionizing radiation. One slice of film was placed where the beam hits the phantom surface. Another slice was placed at 10 cm depth. This was realized by placing one phantom upright and another one in normal orientation behind the first phantom. The film was placed between the two phantoms at 10 cm depth from the beam entrance. The film was irradiated for 1.5 minutes with 150 pA.

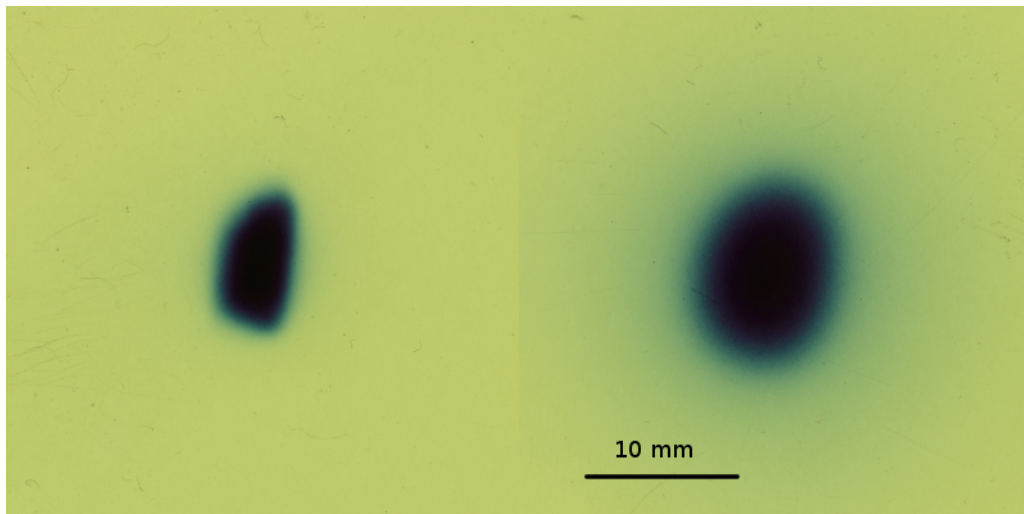


Figure 4.3: Beam profile at the entrance (left) and in 10 cm depth (right).

The resulting stain on the film is shown in figure 4.3. The left half of the image shows the film which was placed at the entrance, the right half was situated at 10 cm depth. At the phantom surface, the extension of the beam is 5 mm horizontal and 8 mm vertical. At 10 cm depth, it has broadened to 10 mm horizontal and 13 mm vertical. These are the dimensions of the volume from which prompt γ -rays are emitted. This volume is expected to show up in reconstructed images from beam measurements.

4.3.3 Trigger Rate

The rate of the gate signal was recorded at different beam currents. The trigger logic was programmed to trigger either on the LSO detector or on the CdZnTe detector. In figure 4.4, the trigger rate for the two settings is plotted over the beam current. With the LSO, the rate is one order of magnitude higher than with the CdZnTe detector only. Both trigger rates scale linearly with the beam current and go into saturation at 60 pA. The LSO trigger rate has a saturation level of 10^5 counts per second and the CdZnTe rate goes up to 10^4 counts per second. Even the LSO rate can securely be handled by the DAQ system which is limited by the gate length of approximately 1 μ s. The gate therefore does not limit the rate capability of the camera system during these beam experiments. It was decided to make most experiments at 50 pA.

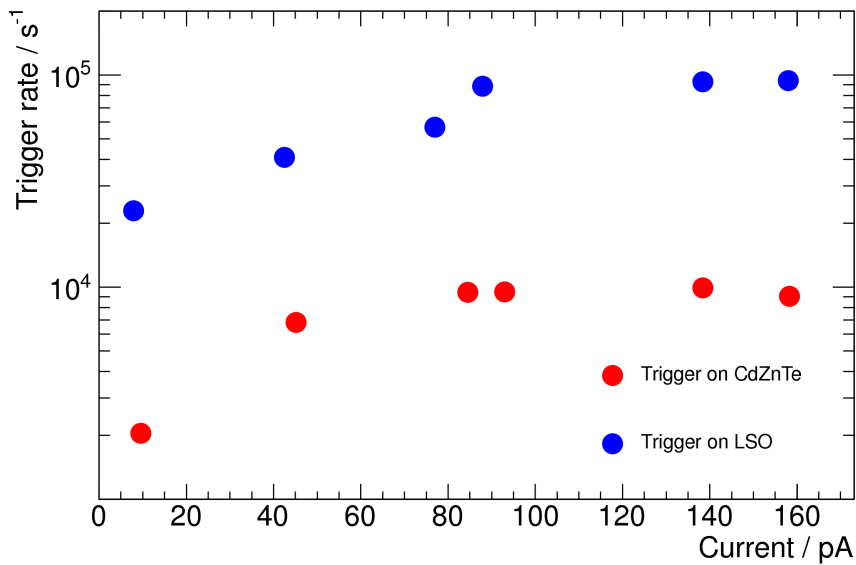


Figure 4.4: Trigger rate in dependence on the beam current.

4.3.4 Pixel selection in the LSO

It has been observed that the LSO interaction map is distorted during the beam experiments. A typical map is shown in figure 4.5. When comparing this map to the interaction map taken during source measurements of figure 3.27 one notices a distortion especially on the edges where the pillow like shape of figure 3.27 is partly abolished.

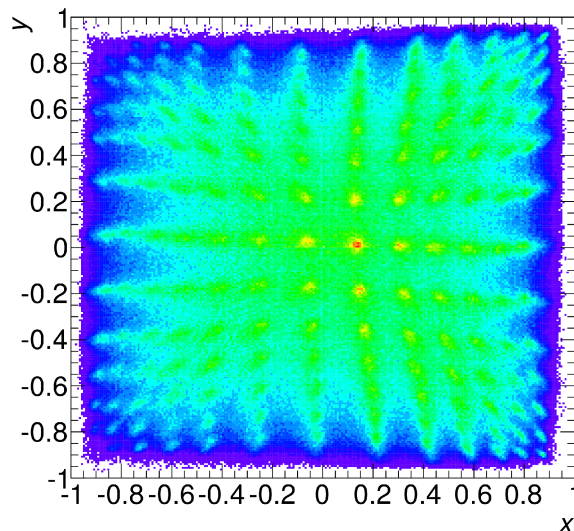


Figure 4.5: LSO interaction map recorded during a beam experiment at 50 μA .

A possible explanation is that there is more light in the scintillator due to the larger energy deposition of beam induced prompt γ -rays compared to photons emitted from radioactive sources. The pixel positions in the map from source measurements include light

loss on the edges what yields to the cushion like shape. These light losses become irrelevant when much light is available due to high energy depositions. The pixel calibration is therefore energy dependent.

To handle this problem, it was decided to restrict the interaction map instead of the deposited energy. The energy is needed to reach up to the expected γ -line at 2.2 MeV. Instead, only hits in the corner pixels have been considered since there is less distortion. Signals from the middle and on the middle part of the edges have a strong signal in more than one PMT while hits in the corners leave one strong signal in one PMT and three smaller signals in the others. The corner signals are therefore expected to be more trustworthy than hits with more than one PMT with a very high signal.

In the following results, only the outermost 4×4 pixels in each corner have been considered.

4.3.5 Phantom Measurement

A PE phantom was irradiated with a beam current of 50 pA. The camera was centered at the depth of the Bragg peak. The energy spectra recorded in the two detectors and the spectrum of the sum energy of recorded events is shown in figure 4.6. In the spectra of the individual detectors, only hits from coincident events have been considered.

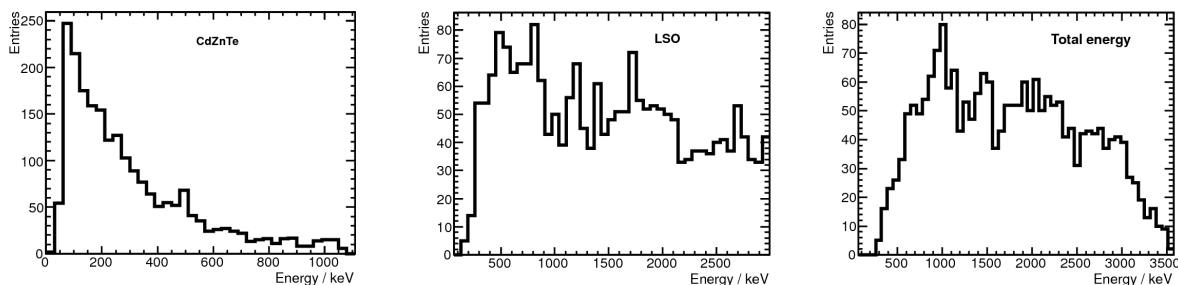


Figure 4.6: Energy spectra in the CdZnTe and LSO detector and the sum spectrum from coincident data taken during a PE irradiation.

There is a 511 keV line visible in the CdZnTe and the LSO spectra which shows up in the sum spectrum around 1000 keV (figure 4.6, right). These are full absorptions of annihilation photons. Those are false coincidences and spoil the data in this energy range. There is no structure in the sum spectrum visible at 2.2 MeV. However, the full energy of the 1275 keV emission of ^{22}Na measurements did not show up clearly either (c.f. figure 3.28).

Images have been reconstructed with this data with different energy windows. The results after five iterations are shown in figure 4.7. In this figure, the left column shows the slice at $z = 0$, i.e. through the center of the phantom where the beam is located. The right column shows the slice in the xy -plane at $y = 0$, i.e. the top-down view. The energy windows from top to bottom are:

- (600 – 800) keV,
- (1000 – 1500) keV,
- (1500 – 2000) keV,
- (2000 – 2400) keV and

4.3 RESULTS

- (2800 – 3500) keV.

Due to the restriction on the LSO corner segments, there are only few events used in these reconstructions despite an irradiation time of 15 minutes. The event numbers in the same order as the energy windows are 155, 426, 416, 362 and 345.

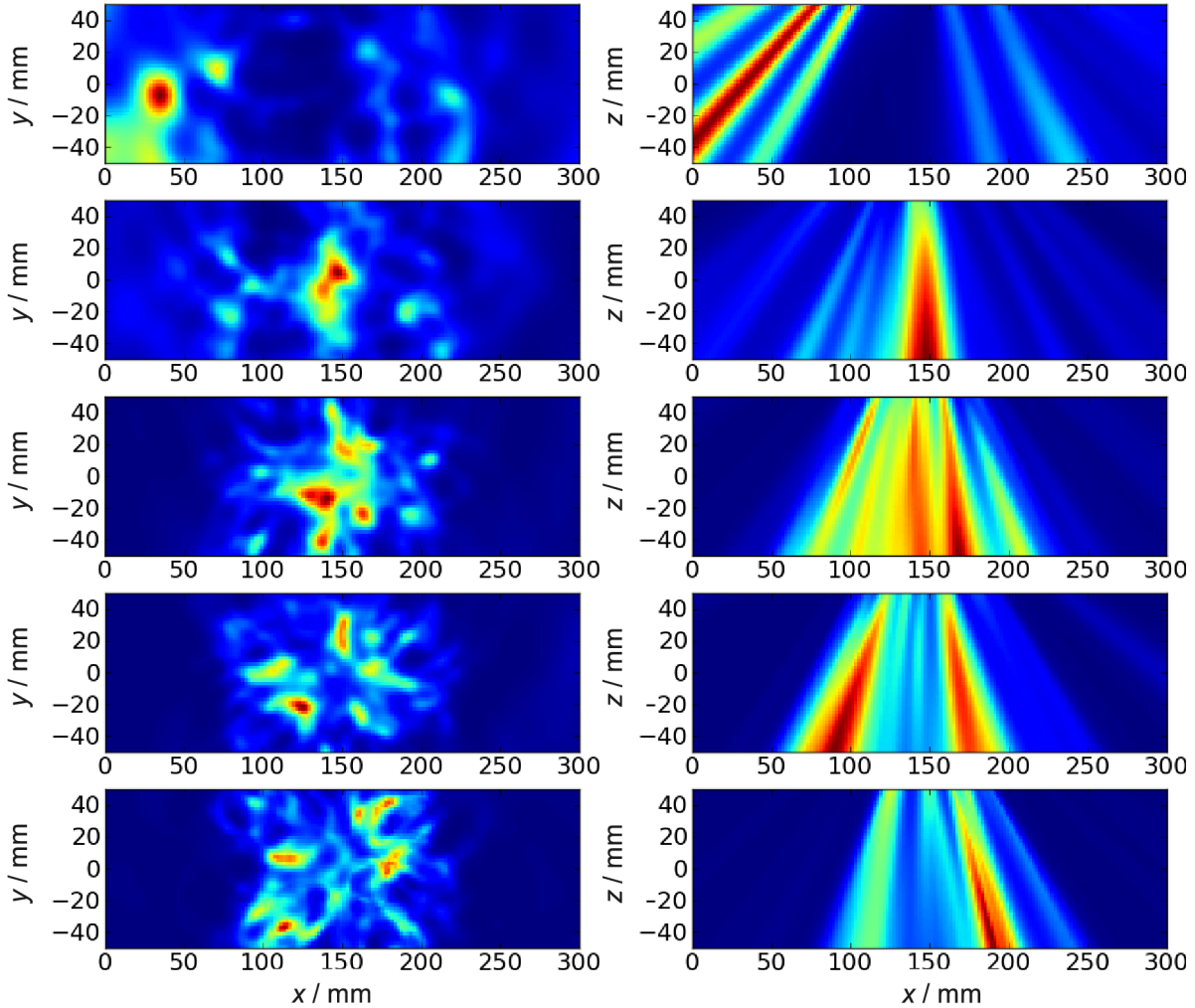


Figure 4.7: Reconstruction results from a PE phantom measurement.

The intensity in the lower energy reconstructions is less concentrated on the middle part of the xy -images like it is the case for the reconstruction for photons of 1.5 MeV and above. This is due to the acceptance of the camera which is low for high energetic photons not incident from the front since those photons are not likely to be scattered with higher scattering angles so that they do not reach the absorber. The intensity of the images reflects this energy dependent acceptance of the Compton camera.

In the xy -plane, there are spots with high intensity which are randomly scattered. In the xz -slice, these spots appear as beams outgoing from the camera. The reconstruction in the energy window of 1000 keV to 1500 keV shows a prominent structure at 150 mm which is about the depth of the Bragg peak. However, this structure could not be reproduced at the Bragg peak position when the phantom was moved a few centimeters along the x axis. The intense points in the images of figure 4.7 are therefore considered to be randomly distributed and not being related to the beam position.

4.4 Conclusions

The experiments failed to yield reconstructed images which gave any information on the beam position. Neither was any spectroscopic data recorded in which the expected γ -line of 2.2 MeV was obvious. Despite this outcome, valuable findings were made concerning the detector components and the overall Compton camera design.

The Anger principle LSO detector was problematic to operate in a radiation field that differs considerably from that of PET measurements with 511 keV photons only for which this kind of detector is designed. The distorted interaction map clearly indicates that this detector was operated beyond its limitations. Reconstruction trials including the events in the middle resulted in images with an extended spot in the center of the field of view not related to the phantom or beam position. The reduction of the sensitive area of the LSO detector was therefore the effort to extract the data with the highest quality. Through the loss of position information in the center of the detector however, the sensitivity for forward scattered photons incident perpendicularly on the CdZnTe detector was reduced.

Furthermore, the count rate experiment emphasized that the LSO detector is much more efficient than the CdZnTe detector mostly due its larger size. Multiple hits in the LSO and random coincidences therefore further spoil the data. The inhomogeneity of the Compton camera design is a very important point and will be discussed in more detail in the final discussion section of this work.

Possibly a better data quality could have been achieved by further reducing the beam current. This would have reduced the occurrence of random coincidences.

There was no indication that the CdZnTe detector was not working as intended. Multiple hits during one gate would have been visible in form of an ambiguous anode channel number. This was not observed. The channel number was in the majority of cases unique. This also suggests that the expected charge sharing among anode channels at large energy depositions does not limit the performance of the CdZnTe detector in a beam induced radiation field. The cross strip design can therefore be considered to be feasible at the chosen beam current.

The reason why there was no spectroscopic signal from expected γ -lines is most likely the small size of the CdZnTe detector. It is too small to absorb several MeV photons at a reasonable efficiency. Furthermore, the aluminum case might have scattered numerous photons into the detectors what could further obscure a signal in the spectrum.

5 Discussion

This work and its results have to be classified in the context of the greater task of bringing Compton imaging to clinical application for in-vivo dose monitoring – if possible. A possible roadmap towards this aim may consist of the following major milestones:

- (1) General feasibility considerations to verify the principle plausibility of the method for this task.
- (2) Develop the technology and methods needed for building a working Compton imaging device.
- (3) Gather practical experience with Compton imaging to derive further requirements and limitations with respect to the clinical application.
- (4) Deliver the proof-of-principle in form of a successful phantom experiment where the beam position has been derived from Compton camera data.
- (5) Develop a system design which achieves the same under actual clinical conditions.
- (6) Verify experimentally that this design is suitable for this task.
- (7) Scale the system up so that it can actually be deployed in therapy.

This study represents the first steps on this road. The method has been checked for plausibility in section 2 and the construction of a working Compton camera device and its application in a beam environment has led to further findings which points the way towards milestone (4) – the successful beam position verification by a Compton camera. The device was able to provide measured data which helped to develop the image reconstruction methods which by these means were not restricted to simulated data.

The gathered knowledge can be divided into conclusions on Compton imaging in general and on the performance and suitability of camera components.

It has been shown in the calculations of section 2, that the efficiency of the camera is generally low and that is further decreases with increasing energy. This is a general problem which can only partly be handled by an elaborated camera design. A Compton camera is a suitable device for the detection of radioactive sources whose γ -ray energies usually do not reach much higher than 2 MeV. This has also been proven in this study with the successful

imaging experiments of ^{22}Na and ^{60}Co sources. However, the raw data is not suited for image reconstruction due to high fraction of events from random coincidences and incomplete energy deposition. Knowledge about the expected γ -ray energy is needed to select data in a certain energy window for reconstruction. This is still a weak limitation in nuclide imaging since one can test the data for the presence of a certain nuclide by choosing the energy windows appropriately. This may still work in dose monitoring since the γ -ray emissions from irradiated material comprise discrete γ -ray lines attributed to certain target nuclei. To exploit the numerous statistical γ -rays, which form a continuous spectrum, requires a better data quality with fewer random coincidences because the energy criterion for event selection cannot be applied for these cases.

Another problem associated with the energy spectrum is the presence of the very high energetic emissions, e.g. from oxygen at 4.4 MeV and from carbon at 6.1 MeV. The efficiency of the camera is highest at the lower γ -ray energies. These line should therefore be easiest to detect. The efficiency for the higher energies is very low. This does however not imply that those photons do not leave a signal in the detector. They react as well but mostly in sequences that are not exploitable by Compton imaging. Much energy escapes from the detector in form of annihilation radiation following pair production in the detector or in form of scattered photons that do not interact further. Photons at higher energy spoil therefore the signal of photons at lower energy. Source measurement were successful because there was no radiation present at higher energies. In the phantom experiments, correctly registered γ -rays of lower energy were probably obscured by the higher energetic emissions.

Since all designs have a decreasing efficiency with increasing γ -ray energy, all Compton camera devices will suffer from this. One can however improve the event selection with the help of detectors with excellent energy resolution. The energy resolution is not only important for the angular resolution but also for the yield of number of good events. In this respect, the chosen design for the evaluation system with the LSO absorber and its low energy resolution was not optimal. High purity germanium should also be re-evaluated as a possible detector material.

Because of the lack of a second suitable CdZnTe detector, the camera developed in this work was designed as a scatter-absorber system only. Optimizing such systems always lead to inhomogeneous concepts with one detection stage optimized for scattering photons and another stage optimized for absorbing the remnants. The datasets for reconstruction always comprise coincident events from these two stages. Combining a slow and small – and thereby less efficient – semiconductor with a fast and large scintillation detector like it has been done in this work, is easily brought to its limits in the radiation field created by an ion beam hitting a phantom. Both detectors individually may be operable; the semiconductor can handle the event rate although it is limited by the charge drift time, because its small size makes it transparent for the majority of the high energetic photons. The scintillator registers many more hits, but is still operable due to its speed. The system as a whole however has to register coincident events. In the chosen layout, the absorber detects ten times as many hits as the scatterer does. During the beam pulses, the time between two hits in the absorber is exponentially distributed. There are numerous events with a small time delay in between. These might fall into the same gate which is triggered by the scatter detector. Through the common gate for both detectors, there is no possibility to detect

multiple hits in one gate. An improved system should therefore have separate gates together with measures to reject piled up events.

Better is however to avoid the very different detector characteristics already in the design. A stack of homogeneous detectors operating in scatter-scatter mode is a technically advanced, however elegant solution to the problems arising from system inhomogeneities.

Conclusions can also be drawn concerning the size and segmentation of a camera module. The CdZnTe detector with the size of 4 cm² saturates at a beam current of 50 pA in a distance of 12.4 cm from the beam axis. Doubling the distance would give an expected saturation current of 200 pA. A therapeutic proton accelerator however delivers a current of 2 nA to the target to achieve a decent treatment time [Mil95]. To bridge the gap between these number, a factor of 10 is needed which can be gained with the considered CdZnTe detectors by transitioning to pixelated readout. 1 mm × 1 mm pixels divide the 4 cm² into 400 segments which would saturate at a current of 80 nA. This is however at the pixel level which implies the assumption that pixels do not interact with each other and that there is no readout of the common cathode. The saturation currents mentioned here depend also on the beam pulse structure. When the same average current is remained, a higher pulse frequency means a more evenly distributed event rate and less pile-up during the pulses.

A stack with 1 mm² pixelated detectors with all pixels triggering at a rate in the order of 10³ counts per second generates a huge number of hits which would have to be sorted into sequences probably belonging to photons scattered in subsequent detectors. This can only be done with accurate timestamps on each hit. With a readout of the anode only, this is not feasible since the electron drift time is not known due to missing depth-of-interaction information. Therefore, thick CdZnTe detectors are only feasible with a segmented cathode readout. This has however other limitations as discussed in the following paragraph. Abandoning the thick detector concept in favor of a stack of many thin detectors is a possible way out if scintillation detectors are out of question due to energy resolution reasons. Thin detectors have shorter drift times and are therefore faster. They do not require depth-of-interaction readout which makes them easier to read out. However, to achieve the same efficiency, the total thickness of a thick detector would have to be reached. This comes at the cost of many electronic channels.

The detector components applied in this work performed differently. One purpose of the camera is to evaluate the suitability of the CdZnTe technology. The chosen cross-strip electrode design together with the front-end electronics worked very well. The energy resolution gained from the anodes was very good. Triggering on the segmented cathode however was only possible due to the relatively low noise on the cathode signals. Smaller cathode strips with smaller signals would probably not be suitable for this triggering mode. Since analogue addition of cathode signals was not feasible as discussed in section 3, only a pixel detector with a continuous cathode would improve the trigger situation. This comes however at the price of more electronic channels.

The depth-of-interaction determination was not working satisfactorily. The reason for this lies also in the segmented cathode readout with individual discrete electronics channels. If a pixel design is out of question, the other possibility is to read out the grid electrode as well and thereby transitioning to a coplanar-grid device.

Despite the good energy resolution achieved with this cross-strip detector, the pixel design would eliminate two problems which became apparent with the CdZnTe detector. It

is the clear recommendation for a future device if CdZnTe is pursued as detector material and not being abandoned in favor for HPGe.

The LSO block detector was suitable for source measurements but not in beam experiments. Neither was the energy resolution sufficient to allow a proper event selection, nor was the Anger principle of determining the fired pixel viable in the beam induced radiation field. If scintillation detectors are to be further pursued for this project, a one-to-one light coupling to the photosensor is mandatory. With the advent of modular SiPM-arrays on the market such detector concepts become feasible without the need for sophisticated light-guides.

The requirement of a good energy resolution restricts the choice of possible scintillation materials. LSO or similar crystals do not yield the needed resolution. Lanthanum bromide is a possible candidate with an excellent energy resolution of 2.6 % at 662 keV, but other materials might also be feasible [Che09].

The developed read-out system based on VME electronics and custom software was suitable for the constructed evaluation system. It has been designed with an additional CdZnTe detector in mind. The addition of this detector should be straightforward and opens the possibility to explore the scatter-scatter Compton imaging regime. The concept might however reach its limits if the recommendation for pixelated detectors is realized.

It emerges that the massive up-scaling of channel numbers is required to achieve the proof-of-principle both due to the required count rate and the failure of the Anger principle in beam conditions. Readout electronics must therefore be moved from the VME crate closer to the detector components in form of integrated circuitry to handle the high channel density. Not only the channel density requires a different approach. Also the amount of data will be multiplied. Therefore, a multi-level trigger system similar to concepts used in high energy physics experiments should be considered [Hau04]. In such a system, it is first decided what hits in the individual detectors meet the criteria to be of interest. Then, trigger patterns on the data from the whole system are applied. Those filters may work with data of lower quality to improve the selection speed. Data passing all criteria are eventually handed over to the image reconstruction.

A similar system is already implemented in the evaluation system constructed in this work with the leading edge triggers on the detectors, the majority number selection in the FPGA board and final energy selection criteria just before image reconstruction. However, increased data rates will probably require to rework some of these filters and implement them closer to the detectors to reduce the load on the final data acquisition system.

This work allows a glimpse on the challenges connected to Compton imaging for proton radiotherapy verification. Real data was acquired and first beam experiments were conducted. It became apparent that the proof-of-principle is beyond the possibilities of the developed camera system due to its simplicity. However, this first imaging device delivered valuable findings towards an advanced system which might eventually be successful in imaging the beam position during a proton irradiation. Moreover, the possibilities of the camera are not completely exploited, yet. The addition of a third detector will allow the exploration of the multiple Compton scattering technique and reveal the inherent limitations of this regime. This is especially important because one finding of this work is, that a homogenous camera in scatter-scatter mode is advantageous in a beam environment.

Appendix A

A.1 Technical Drawing of the CdZnTe Electrode Layout

The following drawings have been generated by Baltic Scientific Instruments. According to those drawings the photomasks for contacting the detectors have been fabricated. They may serve as reference for future projects where CdZnTe cross strip detectors are needed.

A.1 TECHNICAL DRAWING OF THE CDZNTe ELECTRODE LAYOUT

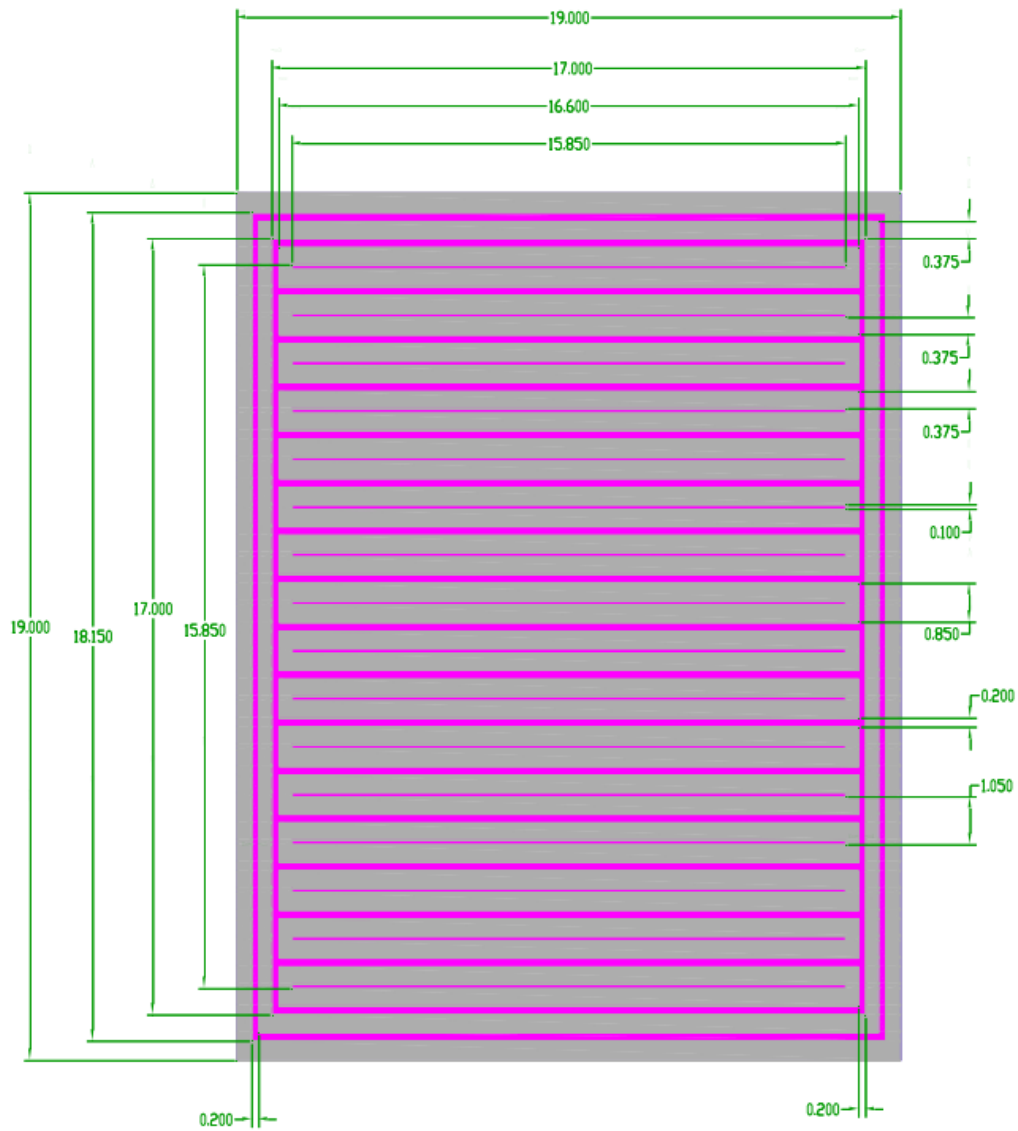


Figure A.1: Technical drawing of the CdZnTe anode layout. Measures are in millimeter. Generated by Baltic Scientific Instruments.

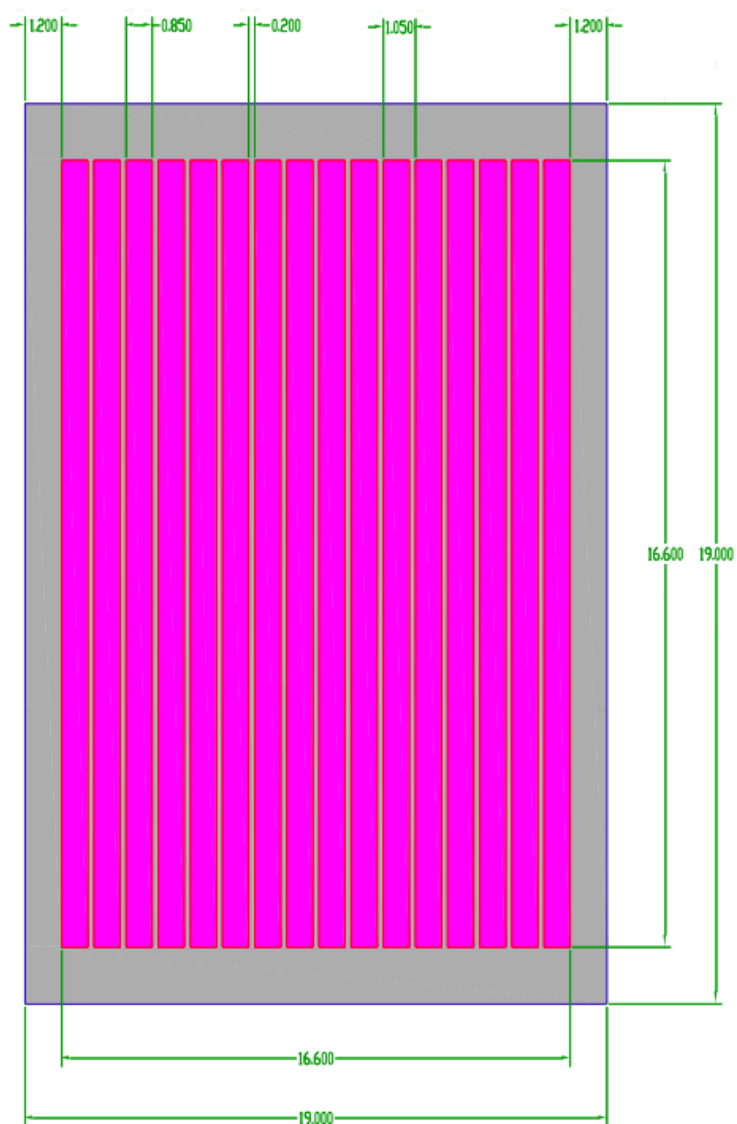


Figure A.2: Technical drawing of the CdZnTe cathode layout. Measures are in millimeter. Generated by Baltic Scientific Instruments.

Bibliography

- [Ago03] Agostinelli S, Allison J, Amako K, Apostolakis J, Araujo H, Arce P, Asai M, Axen D, Banerjee S, Barrand G et al., Geant4 — A Simulation Toolkit. *Nucl Instrum Methods Phys Res A* (2003) **506**: pp. 250 - 303.
- [AGOR] AGORFIRM website. <http://www.agorfirml.nl/>, accessed October 2012.
- [Amm97] Amman MS, Luke PN, Coplanar-Grid Detector with Single-Electrode Readout. *Hard X-Ray and Gamma-Ray Detector Physics, Optics, and Applications* (1997) **3115**: pp. 205 - 213.
- [Ang58] Anger HO, Scintillation Camera. *Review of Scientific Instruments* (1958) **29**: pp. 27 - 33.
- [Bai03] Bai B, Ruangma A, Laforest R, Tai Y, Leahy R, Positron Range Modeling for Statistical PET Image Reconstruction. *Nuclear Science Symposium Conference Record, 2003 IEEE*: pp. 2501 - 2505.
- [Bar95] Barrett HH, Eskin JD, Barber HB, Charge Transport in Arrays of Semiconductor Gamma-Ray Detectors. *Phys Rev Lett* (1995) **75**: pp. 156 - 159.
- [Bel09] Bellm E, Boggs S, Bandstra M, Bowen J, Perez-Becker D, Wunderer C, Zoglauer A, Amman M, Luke P, Chang H et al., Overview of the Nuclear Compton Telescope. *IEEE Trans Nucl Sci* (2009) **56**: pp. 1250 - 1256.
- [Bet32] Bethe H, Bremsformel für Elektronen relativistischer Geschwindigkeit. *Z Phys* (1932) **76**: pp. 293 - 299.
- [Big75] Biggs F, Mendelsohn L, Mann J, Hartree-Fock Compton Profiles for the Elements. *At Data Nucl Data Tables* (1975) **16**: pp. 201 - 309.
- [Bil67] Bilger HR, Fano Factor in Germanium at 77 K. *Phys Rev* (1967) **163**: pp. 238 - 253.
- [Bor96] Bortfeld T, Schlegel W, An Analytical Approximation of Depth-Dose Distributions for Therapeutic Proton Beams. *Phys Med Biol* (1996) **41**: pp. 1331 - 1339.

BIBLIOGRAPHY

- [Bru97] Brun R, Rademakers F, ROOT — An Object Oriented Data Analysis Framework. *Nucl Instrum Methods Phys Res A* (1997) **389**: pp. 81 - 86.
- [But97] Butler JF, Novel Electrode Design for Single-Carrier Charge Collection in Semiconductor Nuclear Radiation Detectors. *Nucl Instrum Methods Phys Res A* (1997) **396**: pp. 427 - 430.
- [Cas86] Casey ME, Nutt R, A Multicrystal Two Dimensional BGO Detector System for Positron Emission Tomography. *IEEE Trans Nucl Sci* (1986) **33**: pp. 460 - 463.
- [Cav71] Cavalleri G, Gatti E, Fabri G, Svelto V, Extension of Ramo's Theorem as Applied to Induced Charge in Semiconductor Detectors. *Nucl Instrum Methods* (1971) **92**: pp. 137 - 140.
- [Ces92] Cesareo R, Hanson A, Gigante G, Pedraza L, Mathabally S, Interaction of keV Photons with Matter and New Applications. *Phys Rep* (1992) **213**: pp. 117 - 178.
- [Che09] Cherepy N, Payne S, Aszatlos S, Hull G, Kuntz J, Niedermayr T, Pimputkar S, Roberts J, Sanner R, Tillotson T et al., Scintillators with Potential to Supersede Lanthanum Bromide. *IEEE Trans Nucl Sci* (2009) **56**: pp. 873 - 880.
- [Com23] Compton AH, A Quantum Theory of the Scattering of X-rays by Light Elements. *Phys Rev* (1923) **21**: pp. 483 - 502.
- [Cui11] Cui Y, Lall T, Tsui B, Yu J, Mahler G, Bolotnikov A, Vaska P, Geronimo GD, O'Connor P, Meinken G et al., Compact CdZnTe-based Gamma Camera for Prostate Cancer Imaging. *International Symposium on Photoelectronic Detection and Imaging 2011: Laser Sensing and Imaging; and Biological and Medical Applications of Photonics Sensing and Imaging* (2011) **8192**: p. 819255-1 - 819255-8.
- [Deg10] Degenhardt C, Zwaans B, Frach T, de Gruyter R, Arrays of Digital Silicon Photomultipliers; Intrinsic Performance and Application to Scintillator Readout. *Nuclear Science Symposium Conference Record (NSS/MIC), 2010 IEEE*: pp. 1954 - 1956.
- [Ein05] Einstein A, Über einen die Erzeugung und Verwandlung des Lichtes betreffenden heuristischen Gesichtspunkt. *Ann Phys* (1905) **322**: pp. 132 - 148.
- [Eng04] Enghardt W, Crespo P, Fiedler F, Hinz R, Parodi K, Pawelke J, Pönisch F, Charged Hadron Tumour Therapy Monitoring by Means of PET. *Nucl Instrum Methods Phys Res A* (2004) **525**: pp. 284 - 288.
- [EV11] Semiconductor Detector Material Properties. http://www.evmicroelectronics.com/pdf/material_prop.pdf, accessed May 2011.
- [Fie10] Fiedler F, Simulations of Single γ -ray Production During Therapeutic Proton Irradiation. *Forschungszentrum Dresden-Rossendorf* (2011).

-
- [Fie10a] Fiedler F, Kormoll T, Müller A, Enghardt W, Requirements on the Instrumentation of a Prompt Gamma Measuring Device. *Nuclear Science Symposium Conference Record (NSS/MIC), 2010 IEEE*: pp. 1047 - 1049.
- [For07] Forot M, Laurent P, Lebrun F, Limousin O, Compton Telescope with a Coded Aperture Mask: Imaging with the INTEGRAL/IBIS Compton Mode. *Astrophys J* (2007) **668**: pp. 1259 - 1265.
- [Fou10] Le Foulher F, Bajard M, Chevallier M, Dauvergne D, Freud N, Henriquet P, Karkar S, Létang J, Lestand L, Plescak R et al., Monte Carlo Simulations of Prompt-Gamma Emission During Carbon Ion Irradiation. *IEEE Trans Nucl Sci* (2010) **57**: pp. 2768 - 2772.
- [Geo93] Georgiev A, Gast W, Digital Pulse Processing in High Resolution, High Throughput, Gamma-ray Spectroscopy. *IEEE Trans Nucl Sci* (1993) **40**: pp. 770 - 779.
- [Gol11] Golnik C, Dersch U, Fiedler F, Kormoll T, Rohling H, Enghardt W, A Pair Production Upgrade for a Compton Imager for In-vivo Dosimetry at Therapeutic Proton and Ion Beams. *Nuclear Science Symposium and Medical Imaging Conference (NSS/MIC), 2011 IEEE*: pp. 3323 - 3326.
- [Gra09] van der Graaf E, Ostendorf R, van Goethem M, Kiewiet H, Hofstee M, Brandenburg S, AGORFIRM, the AGOR Facility for Irradiations of Materials. *2009 European Conference on Radiation and Its Effects on Components and Systems (RADECS)*: pp. 451 - 454.
- [Gu11] Gu Y, Matteson JL, Skelton RT, Deal AC, Stephan EA, Duttweiler F, Gasaway TM, Levin CS, Study of a High-Resolution, 3D Positioning Cadmium Zinc Telluride Detector for PET. *Phys Med Biol* (2011) **56**: pp. 1563 - 1584.
- [Haa08] de Haas J, Dorenbos P, Advances in Yield Calibration of Scintillators. *IEEE Trans Nucl Sci* (2008) **55**: pp. 1086 - 1092.
- [Hau04] Hauser R, The ATLAS Trigger System. *Eur Phys J C* (2004) **34**: p. s173 - s183.
- [Hay51] Haynes JR, Shockley W, The Mobility and Life of Injected Holes and Electrons in Germanium. *Phys Rev* (1951) **81**: pp. 835 - 843.
- [He01] He Z, Review of the Shockley–Ramo Theorem and its Application in Semiconductor Gamma-ray Detectors. *Nucl Instrum Methods Phys Res A* (2001) **463**: pp. 250 - 267.
- [He97] He Z, Knoll G, Wehe D, Miyamoto J, Position-sensitive Single Carrier CdZnTe Detectors. *Nucl Instrum Methods Phys Res A* (1997) **388**: pp. 180 - 185.
- [Hec32] Hecht K, Zum Mechanismus des lichtelektrischen Primärstromes in isolierenden Kristallen. *Z Phys* (1932) **77**: pp. 235 - 245.
- [Hel12] Helmbrecht S, Santiago A, Enghardt W, Kuess P, Fiedler F, On the Feasibility of Automatic Detection of Range Deviations from In-beam PET Data. *Phys Med Biol* (2012) **57**: pp. 1387 - 1397.
-

- [Jen41] Jen CK, On the Induced Current and Energy Balance in Electronics. *Proceedings of the IRE* (1941) **29**: pp. 345 - 349.
- [Kab09] Kabuki S, Ueno K, Kurosawa S, Iwaki S, Kubo H, Miuchi K, Fujii Y, Kim D, Kim J, Kohara R et al., Study on the Use of Electron-tracking Compton Gamma-ray Camera to Monitor the Therapeutic Proton Dose Distribution in Real Time. *Nuclear Science Symposium Conference Record (NSS/MIC), 2009 IEEE*: pp. 2437 - 2440.
- [Kab10] Kabuki S, Kimura H, Amano H, Nakamoto Y, Kubo H, Miuchi K, Kurosawa S, Takahashi M, Kawashima H, Ueda M et al., Electron-tracking Compton Gamma-ray Camera for Small Animal and Phantom Imaging. *Nucl Instrum Methods Phys Res A* (2010) **623**: pp. 606 - 607.
- [Kan04] Kanbach G, Andritschke R, Schopper F, Schönfelder V, Zoglauer A, Bloser P, Hunter S, Ryan J, McConnell M, Reglero V et al., The MEGA Project. *New Astron Rev* (2004) **48**: pp. 275 - 280.
- [Kan10] Kantemiris I, Angelopoulos A, Bassler N, Giokaris N, Holzscheiter MH, Karaiskos P, Kalogeropoulos TE, Collaboration A, Real-time Imaging for Dose Evaluation During Antiproton Irradiation. *Phys Med Biol* (2010) **55**: p. N123 - N131.
- [Kem80] Kemmer J, Fabrication of Low Noise Silicon Radiation Detectors by the Planar Process. *Nucl Instrum Methods* (1980) **169**: pp. 499 - 502.
- [Kle29] Klein O, Nishina T, Über die Streuung von Strahlung durch freie Elektronen nach der neuen relativistischen Quantendynamik von Dirac. *Z Phys* (1929) **52**: pp. 853 - 868.
- [Kno00] Knoll GF. Radiation Detection and Measurement. Wiley, 2000.
- [Kor09a] Kormoll T. In-vivo Dosimetrie für harte Photonenstrahlen auf der Basis der Paarbildung. *Diploma Thesis*, Technische Universität Dresden. 2009.
- [Kor11] Kormoll T, Fiedler F, Schöne S, Wüstemann J, Zuber K, Enghardt W, A Compton Imager for In-vivo Dosimetry of Proton Beams — A Design Study. *Nucl Instrum Methods Phys Res A* (2011) **626 - 627**: pp. 114 - 119.
- [Kor11a] Kormoll T, Fiedler F, Golnik C, Heidel K, Kempe M, Schöne S, Sobiella M, Zuber K, Enghardt W, A Prototype Compton Camera for In-vivo Dosimetry of Ion Beam Cancer Irradiation. *Nuclear Science Symposium and Medical Imaging Conference (NSS/MIC), 2011 IEEE*: pp. 3484 - 3487.
- [Kor12] Kormoll T, Fiedler F, Golnik C, Heidel K, Kempe M, Schoene S, Sobiella M, Zuber K, Enghardt W, Imaging of Point Sources with a Compton Camera for In-vivo Dose Monitoring of Ion Beam Irradiation. *Radiother Oncol* (2012) **102**, **Supplement 1**: p. S41 - S42.
- [Kur00] Kurfess JD, Johnson WN, Kroeger RA, Philips BF, Considerations for the Next Compton Telescope Mission. *AIP Conference Proceedings* (2000) **510**: pp. 789 - 793.

-
- [Lan91] Landau L, Lifschitz E. Lehrbuch der theoretischen Physik: Quantenelektrodynamik. Harri Deutsch GmbH, 1991.
- [Lav83] Laval M, Moszyński M, Allemant R, Cormoreche E, Guinet P, Odru R, Vacher J, Barium Fluoride — Inorganic Scintillator for Subnanosecond Timing. *Nucl Instrum Methods Phys Res* (1983) **206**: pp. 169 - 176.
- [Luk94] Luke PN, Single Polarity Charge Sensing in Ionization Detectors Using Coplanar Electrodes. *Appl Phys Lett* (1994) **65**: pp. 2884 - 2886.
- [Mil95] Miller DW, A Review of Proton Beam Radiation Therapy. *Med Phys* (1995) **22**: pp. 1943 - 1954.
- [Mol62] Mollenauer JF, Gamma-Ray Emission from Compound Nucleus Reactions of Helium and Carbon Ions. *Phys Rev* (1962) **127**: pp. 867 - 879.
- [Owe02] Owens A, Bavdaz M, Andersson H, Gagliardi T, Krumrey M, Nenonen S, Peacock A, Taylor I, Tröger L, The X-ray Response of CdZnTe. *Nucl Instrum Methods Phys Res A* (2002) **484**: pp. 242 - 250.
- [Par05] Parodi K, Crespo P, Eickhoff H, Haberer T, Pawelke J, Schardt D, Enghardt W, Random Coincidences During In-beam PET Measurements at Microbunched Therapeutic Ion Beams. *Nucl Instrum Methods Phys Res A* (2005) **545**: pp. 446 - 458.
- [Par07] Parodi K, Paganetti H, Shih HA, Michaud S, Loeffler JS, DeLaney TF, Liebsch NJ, Munzenrider JE, Fischman AJ, Knopf A et al., Patient Study of In Vivo Verification of Beam Delivery and Range, Using Positron Emission Tomography and Computed Tomography Imaging After Proton Therapy. *Int J Radiat Oncol Biol Phys* (2007) **68**: pp. 920 - 934.
- [Pat96] Patt B, Iwanczyk J, Vilkelis G, Wang Y, New Gamma-ray Detector Structures for Electron Only Charge Carrier Collection Utilizing High-Z Compound Semiconductors. *Nucl Instrum Methods Phys Res A* (1996) **380**: pp. 276 - 281.
- [Paw97] Pawelke J, Enghardt W, Haberer T, Hasch B, Hinz R, Krämer M, Lauckner K, Sobiella M, In-beam PET Imaging for the Control of Heavy-ion Tumour Therapy. *IEEE Trans Nucl Sci* (1997) **44**: pp. 1492 - 1498.
- [Pel11] Peloso R, Busca P, Fiorini C, Basilavecchia M, Frizzi T, Smeets J, Roellinghoff F, Prieels D, Stichelbaut F, Benilov A, Application of the HICAM Camera for Imaging of Prompt Gamma Rays in Measurements of Proton Beam Range. *Nuclear Science Symposium and Medical Imaging Conference (NSS/MIC), 2011 IEEE*: pp. 2285 - 2289.
- [Pet00] Peterson SW, Robertson D, Polf J, Optimizing a Three-stage Compton Camera for Measuring Prompt Gamma Rays Emitted During Proton Radiotherapy. *Phys Med Biol* (2010) **55**: pp. 6841 - 6856.
- [Pol09] Polf JC, Peterson S, Ciangaru G, Gillin M, Beddar S, Prompt Gamma-ray Emission from Biological Tissues During Proton Irradiation: A Preliminary Study. *Phys Med Biol* (2009) **54**: pp. 731 - 743.
-

BIBLIOGRAPHY

- [Ram39] Ramo S, Currents Induced by Electron Motion. *Proceedings of the IRE* (1939) 27: pp. 584 - 585.
- [Ree72] Reed WA, Eisenberger P, Gamma-Ray Compton Profiles of Diamond, Silicon, and Germanium. *Phys. Rev. B* (1972) 6: pp. 4596 - 4604.
- [Rib75] Ribberfors R, Relationship of the Relativistic Compton Cross Section to the Momentum Distribution of Bound Electron States. *Phys Rev B* (1975) 12: pp. 2067 - 2074.
- [Rib82] Ribberfors R, Berggren K, Incoherent-x-ray-scattering Functions and Cross Sections by Means of a Pocket Calculator. *Phys Rev A* (1982) 26: pp. 3325 - 3333.
- [Ric11] Richard M, Chevallier M, Dauvergne D, Freud N, Henriquet P, Le Foulher F, Létang J, Montarou G, Ray C, Roellinghoff F et al., Design Guidelines for a Double Scattering Compton Camera for Prompt-Gamma Imaging During Ion Beam Therapy: A Monte Carlo Simulation Study. *IEEE Trans Nucl Sci* (2011) 58: pp. 87 - 94.
- [Rob11] Robertson D, Polf JC, Peterson SW, Gillin MT, Beddar S, Material Efficiency Studies for a Compton Camera Designed to Measure Characteristic Prompt Gamma Rays Emitted During Proton Beam Radiotherapy. *Phys Med Biol* (2011) 56: pp. 3047 - 3059.
- [Roe11] Roellinghoff F, Richard M, Chevallier M, Constanzo J, Dauvergne D, Freud N, Henriquet P, Foulher FL, Létang J, Montarou G et al., Design of a Compton Camera for 3D Prompt-gamma Imaging During Ion Beam Therapy. *Nucl Instrum Methods Phys Res A* (2011) 648, **Supplement 1**: p. S20 - S23.
- [Sau31] Sauter F, Über den atomaren Photoeffekt in der K-Schale nach der relativistischen Wellenmechanik Diracs. *Ann Phys* (1931) 403: pp. 454 - 488.
- [Scho10] Schöne S, Shakirin G, Kormoll T, Herbach C, Pausch G, Enghardt W, A Common Approach to Image Reconstruction for Different Applications of Compton Cameras. *Nuclear Science Symposium Conference Record (NSS/MIC), 2010 IEEE*: pp. 2292 - 2293.
- [Scho73] Schönfelder V, Hirner A, Schneider K, A Telescope for Soft Gamma Ray Astronomy. *Nucl Instrum Methods* (1973) 107: pp. 385 - 394.
- [Scho84] Schönfelder V, Diehl R, Lichti GG, Steinle H, Swanenburg BN, Deerenberg AJM, Aarts H, Lockwood J, Webber W, Macri J et al., The Imaging Compton Telescope Comptel on the Gamma Ray Observatory. *IEEE Trans Nucl Sci* (1984) 31: pp. 766 - 770.
- [Schw11] Schwenke M, Zuber K, Janutta B, He Z, Zeng F, Anton G, Michel T, Durst J, Lück F, Gleixner T et al., Exploration of Pixelated Detectors for Double Beta Decay Searches within the COBRA Experiment. *Nucl Instrum Methods Phys Res A* (2011) 650: pp. 73 - 78.

-
- [Sha11] Shakirin G, Braess H, Fiedler F, Kunath D, Laube K, Parodi K, Priegnitz M, Enghardt W, Implementation and Workflow for PET Monitoring of Therapeutic Ion Irradiation: A Comparison of In-beam, In-room, and Off-line Techniques. *Phys Med Biol* (2011) **56**: pp. 1281 - 1298.
- [She82] Shepp LA, Vardi Y, Maximum Likelihood Reconstruction for Emission Tomography. *IEEE Trans Med Imaging* (1982) **1**: pp. 113 - 122.
- [Sho38] Shockley W, Currents to Conductors Induced by a Moving Point Charge. *J Appl Phys* (1938) **9**: pp. 635 - 636.
- [Sin85] Singh M, Doria D, Single Photon Imaging with Electronic Collimation. *IEEE Trans Nucl Sci* (1985) **32**: pp. 843 - 847.
- [Sze04] Szeles C, CdZnTe and CdTe Materials for X-ray and Gamma Ray Radiation Detector Applications. *Phys Status Solidi B* (2004) **241**: pp. 783 - 790.
- [Tes12] Testa E, Chevallier M, Dauvergne D, Dedes G, Rydt MD, Freud N, Henriquet P, Krimmer J, Létang J, Ray C et al., Real-time Monitoring of the Bragg Peak during Ion Therapy: A Feasibility Study of Interaction Vertex Imaging. *Radiother Oncol* (2012) **102**, **Supplement 1**: p. S123.
- [Tod74] Todd RW, Nightingale JM, Everett DB, A Proposed Gamma Camera. *Nature* (1974) **251**: pp. 132 - 134.
- [Vet07] Vetter K, Burks M, Cork C, Cunningham M, Chivers D, Hull E, Krings T, Manini H, Mihailescu L, Nelson K et al., High-sensitivity Compton Imaging with Position-sensitive Si and Ge Detectors. *Nucl Instrum Methods Phys Res A* (2007) **579**: pp. 363 - 366.
- [Wah10] Wahl C, He Z, Point-source Detection using 3D-position-sensitive Semiconductor Detectors with Estimated Background. *Nuclear Science Symposium Conference Record (NSS/MIC), 2010 IEEE*: pp. 1096 - 1100.
- [Wur07] Würschig T, Kluge T, Heidel K, Sobiella M, Enghardt W, An Experimental Positron Emission Tomograph for Education. *Z Med Phys* (2007) **17**: pp. 212 - 217.
- [XCOM] NIST XCOM: Photon Cross Sections Database.
<http://www.nist.gov/pml/data/xcom/index.cfm>, accessed June 2012.
- [Zha05] Zhang F, He Z, Knoll G, Wehe D, Berry J, 3-D Position Sensitive CdZnTe Spectrometer Performance using Third Generation VAS/TAT Readout Electronics. *IEEE Trans Nucl Sci* (2005) **52**: pp. 2009 - 2016.
- [Zha09] Zhang F, Kaye W, He Z, Performance of 3-D Position Sensitive CdZnTe Detectors for Gamma-ray Energies above 1 MeV. *Nuclear Science Symposium Conference Record (NSS/MIC), 2009 IEEE*: pp. 2012 - 2016.
- [Zog03] Zoglauer A, Kanbach G, Doppler Broadening as a Lower Limit to the Angular Resolution of Next-generation Compton Telescopes. *Society of Photo-Optical Instrumentation Engineers (SPIE) Conference Series (2003)*: pp. 1302 - 1309.
-

BIBLIOGRAPHY

- [Zog06] Zoglauer AC, First Light for the Next Generation of Compton and Pair Telescopes: Development of New Techniques for the Data Analysis of Combined Compton and Pair Telescopes and their Application to the MEGA Prototype. Max-Planck-Institut für extraterrestrische Physik (2006).

Danksagung

Diese Arbeit wäre nicht entstanden, ohne dass viele Personen mitgewirkt hätten. Ich danke Prof. Kai Zuber und Prof. Wolfgang Enhardt, dass sie diese Arbeit begleitet und unterstützt haben und auch dafür, dass ich die Möglichkeit bekommen habe, auf zahlreichen Vorträgen die Ergebnisse vorzustellen.

Bei Klaus Heidel bedanke ich mich für die Entwicklung der Elektronik. Ohne seinen Einsatz und seine Begeisterung wäre dieses Projekt nicht weit gekommen. Die Zusammenarbeit war mir eine große Freude und einer der Höhepunkte bei der Entwicklung dieser Kamera. Vielen Dank auch an Heiko Gude, der unzählige Stecker an insgesamt über 500 m Kabel gelötet hat. Für die mechanische Konstruktion in gewohnt hoher Qualität war Manfred Sobiella verantwortlich. Vielen Dank dafür! Ich bedanke mich auch bei Christian Golnik für seine Beiträge zum Computer-Code und seinen Beitrag zu den Messungen. Mit Sebastian Schöne zu arbeiten hat großen Spaß gemacht. Wir haben unsere „Schnittstelle“ definiert – nicht nur für Messdaten. Bei den Mitarbeitern am KVI in Groningen bedanke ich mich für die Unterstützung bei der Durchführung der Strahlexperimente, allen voran Peter Dendooven und Harry Kiewit.

Meiner Frau Kathrin Kormoll danke ich für die ausgezeichnete, alltägliche Teamarbeit. Ohne Dich wäre ich nicht fertig geworden!

Erklärung

Hiermit versichere ich, dass ich die vorliegende Arbeit ohne unzulässige Hilfe Dritter und ohne Benutzung anderer als der angegebenen Hilfsmittel angefertigt habe; die aus fremden Quellen direkt oder indirekt übernommenen Gedanken sind als solche kenntlich gemacht. Die Arbeit wurde bisher weder im Inland noch im Ausland in gleicher oder ähnlicher Form einer anderen Prüfungsbehörde vorgelegt.

Die Arbeit wurde unter der wissenschaftlichen Betreuung von Prof. Dr. Wolfgang Enghardt am National Center for Radiation Research in Oncology, OncoRay, Dresden, angefertigt.

Thomas Kormoll, Dresden, den 30. November 2012